UNIVERSIDAD DE CHILE
FACULTAD DE CIENCIAS FÍSICAS Y MATEMÁTICAS
DEPARTAMENTO DE FÍSICA

NON-IDEAL RHEOLOGY AND SPATIAL STRUCTURES OF BACTERIAL SUSPENSIONS IN THE SEMI-DILUTE REGIME

TESIS PARA OPTAR AL GRADO DE MAGÍSTER EN CIENCIAS, MENCIÓN FÍSICA

MARCELO ANDRÉS GUZMÁN JARA

PROFESOR GUÍA:
RODRIGO SOTO BERTRÁN

MIEMBROS DE LA COMISIÓN:
ERIC CLÉMENT
MARCEL CLERC GAVILÁN
JUAN KEYMER REYES

Este trabajo ha sido financiado por CONICYT

SANTIAGO DE CHILE
2018

RESUMEN DE LA TÉSIS PARA OPTAR
AL TÍTULO DE MAGÍSTER EN CIENCIAS, MENCIÓN FÍSICA
POR: MARCELO ANDRÉS GUZMÁN JARA
FECHA: 2018
PROF. GUÍA: SR. RODRIGO SOTO BERTRÁN

En esta tesis se presenta un estudio de la reología y de las estructuras espaciales que surgen en suspensiones de bacterias en el regimen semi-diluido.

Debido al tamaño microscópico de las bacterias, su densidad y velocidad de propulsión, estas viven en un ambiente caracterizado por un bajo número de Reynolds, por lo que la fuerza y torque total sobre ellas son nulos. Por lo tanto, a primer orden, las perturbaciones en el campo de velocidades producidas por estos nadadores corresponde a un dipolo de fuerzas. Además, el dipolo de fuerzas ejerce un cizalle en el fluido, el que puede traducirse en una viscosidad activa cuando se impone un flujo externo. Esta contribución puede llegar a ser tal que la viscosidad total es nula o incluso negativa, como se ha encontrado experimentalmente.

Los nadadores presentan interacciones de corto y largo alcance. En el regimen semi-diluido, las concentraciones siguen siendo bajas, pero suficientemente altas para que las interacciones de corto alcance sean relevantes sin que las de largo alcance jueguen un rol fundamental. Estas interacciones se traducen principalmente en un alineamiento entre bacterias cercanas debido a efectos estéricos e hidrodinámicos.

En esta tesis se extiende la teoría cinética de suspensiones bacterianas en el régimen diluido, considerando interacciones de corto alcance a través de una integral colisional. Se presentan dos tipos de interacciones: alineamiento polar y nemático. A partir de la ecuación cinética es posible obtener las ecuaciones hidrodinámicas de la densidad, la orientación promedio y el tensor nemático cuando existe un flujo impuesto. En particular, en esta tesis se estudia el caso de un flujo de corte uniforme.

Para sistemas homogéneos se encontró que por sobre cierta concentración crítica, existe una transición hacia una fase polar o nemática, según el tipo de interacción. Ambas fases dan origen a una viscosidad oscilante en el tiempo. A través de un análisis de separación de escalas, cercano a la concentración crítica, se obtienen expresiones analíticas para la orientación promedio y el cizalle producido por una suspensión. Resultados numéricos revelan, además, que para grandes tasas de corte la fase ordenada se pierde. En particular, para colisiones nemáticas, esta fase se pierde de manera subcrítica.

Finalmente se estudió la dependencia espacial de la suspensión bacteriana. A través de simulaciones tipo DSMC (Direct Simulation Monte Carlo) se resolvió la ecuación cinética condiciones de borde rígidas, encontrando estructuras espaciales en la suspensión bacteriana. El mismo fenómeno se encuentra al emplear condiciones de borde periódicas, por lo que se analizó la estabilidad lineal de la solución homogénea al ser perturbada con ondas planas. Los resultados indican que la inestabilidad ocurre para grandes longitudes de onda, por lo que es posible mediarla a través del tamaño del sistema. Además, al incluir interacciones de largo alcance al análisis de estabilidad, se obtienen que estas sólo modifican cuantitativamente los resultados. Finalmente, este fenómeno también se encontró en tres dimensiones.

SUMMARY

In this thesis we study the rheology and the spatial structures that emerge in bacterial suspensions in the semi-dilute regime.

Due to the microscopic size of the bacteria, their density, and their velocity, they live in a low Reynolds number environment, which is characterized by a null total force and torque acting on them. Therefore, to first order, the perturbations produced in the velocity field by the activity of the swimmers correspond to force dipoles. Moreover, these force dipoles exert a shear stress on the fluid, which can be translated into an active viscosity when there is an imposed flow. This contribution to the fluid viscosity can be large enough so the total viscosity is zero or even negative, as it has been found experimentally.

The swimmers interact through short- and long-range interactions. In the semi-dilute regime, the concentrations are still low but high enough for the short-range interactions to dominate over the long-range counterparts. These interactions translate mainly into an alignment among near bacteria, due to steric and hydrodynamics effects.

In this thesis we extend the kinetic theory of bacterial suspensions in the dilute regime, where the short-range interactions are included through a Boltzmann-like collision integral in the kinetic equation. We present two kinds of interactions: polar and nematic alignment. From the kinetic equation we can obtain the hydrodynamic equations for the density, the average orientation, and the nematic tensor, when there is an imposed flow. In particular, in this thesis we study the case of an imposed uniform shear flow.

For homogeneous systems we found that, above a critical concentration, there is a transition to a polar or nematic phase, depending on the nature of the interaction. Both phases lead to an oscillatory viscosity in time, around a value that is close to the viscosity obtained in the dilute regime. Through a multi-scale scheme near the critical concentration, we obtained analytical expressions for the average orientation and the shear stress produced by the activity of the swimmers. These results are confirmed by numerical solutions, finding as well that for large shear rates, the ordered phase disappears. In particular, for nematic collisions, the ordered phase is lost in a subcritical transition.

Finally, we studied the spatial dependence of a bacterial suspension. By testing different boundary conditions, we concluded that the only one capable of reproducing a homogeneous suspension, is the anti-specular collision with the wall. Through DSMC (direct simulation Monte Carlo) simulations, we solved the kinetic equation with spatial dependence and rigid boundary conditions, finding that spatial structures emerge in the bacterial suspension. The same phenomenon was found when employing period-like boundary conditions, which allowed us to analyze the linear stability of the homogeneous solution when it is perturbed by plane-waves. The results showed that there is a critical wave-length, above which the instability appears. Therefore, it is possible to mediate the instability through the system size. Moreover, the same analysis was performed including long-range hydrodynamic interactions, finding a small quantitative correction. Finally, the same phenomenon was found in three dimensions.

Acknowledgements

First of all, I would like to thank my supervisor, Rodrigo Soto, who has been an extraordinary guide in this whole process. Thanks for the patience to explain even the simplest concepts, the trust, the support, and the invitations to several conferences and schools worldwide. He is a true model for what a scientist should be.

I am also grateful for the CONICYT PFCHA Magister Nacional Scholarship 2016-22162176, for funding this work, and the ECOS-Sud project for letting me spend some time in France. In this regard, I completely appreciate the help from Eric Clément and his group, for the great welcome they gave me as well as all the constructive discussion we had.

I am truly indebted to my parents, my sister and my brother, for their unconditional support. Without their help this work would not have been finished. Special thanks to my friends that keep me in touch with the real world: the few that remain from high school, the ones that accompanied me during my undergraduate studies, and finally, my office colleagues. Your craziness made my days.

I am profoundly thankful to Maya, for showing me a whole new perspective of the world, for her support, and her sincere love.

Finally, I have to thank all the people that directly and indirectly helped to finish this work. To all the friends that I made during the conferences, the colleagues of the active matter group and from all the internships that I did, and the people that I met in Brazil and did all they could to help me finish my thesis. Thanks to you all.

Contents

List of Figures

Chapter 1

Introduction

1.1 Active Matter

Active matter refers to systems made of a plethora of units with the capacity to extract energy from the environment and turn it into motion [25]. The examples cover a wide variety of time and length-scales, both in living and artificial systems: flocks of birds, schools of fishes [28], bacterial suspensions [10], crowds of microrobots [32], suspensions of active colloids [29], cellular cultures [18], microtubules in suspensions [40], etc. The first two examples correspond to active matter acting in the macro-scale, whereas the rest acts in the micro-scale. Moreover, there is a further classification into wet and dry systems, where in the former the activity mediated by the surrounding fluid is important so the dynamics of the fluid must be considered, as in bacterial suspensions, whereas in the latter, the fluid can be treated as an inert medium providing only friction, like in animal herds on land [28] [41] and vibrated granular particles [20].

The understanding of active matter at the micro and nano-scale have attracted an important interest in the last years in multiples areas of science in technology: it can lead to the development of novel micro-motors based on bacteria activity [46] [36], the development of micro-cargos for pharmaceutical use [9], the understanding of cell dynamics and morphologies in cell colonies [11], and ultimately shed some light on fundamental questions such as the origin of life or its development at early stages.

1.2 Individual Swimmers

As a first approximation, a microswimmer can be modelled by its centre of mass position $\boldsymbol{r}$ and its director vector $\boldsymbol{p}$, so the swimming velocity is given by $\boldsymbol{v} = V_0\boldsymbol{p}$. In the absence of external flows, both $\boldsymbol{r}$ and $\boldsymbol{p}$ vary due to thermal fluctuations that are taken into account by considering spatial (D) and rotational (D_r) diffusion. Nonetheless, the self-propulsion and the rotational diffusion give rise to an effective diffusivity, the Berg diffusivity $D_\mathrm{Berg} \sim V_0^2/D_\mathrm{r}$,

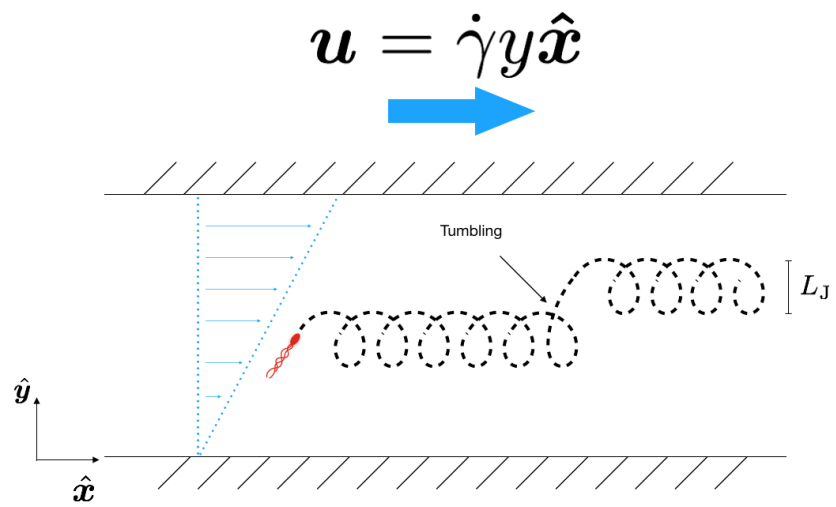

Figure 1.1: Jeffery's orbit representation in a simple shear flow, where a tumbling event makes the swimmer migrate to a different orbit.

which is typically much larger than the Brownian (spatial) diffusion [5].

Flagellated bacteria such as *E. Coli* present a particular mechanism of reorientation called *rund and tumble* [21]. When a bacterium *runs* all its flagella form a bundle that rotate counterclockwise, propelling the swimmer. During the *tumble* phase, one or more flagellum rotate clockwise, undoing the bundle and reorienting the swimmer.

If an external flow $\boldsymbol{u}$ is present, then the swimmer is advected:

$$\boldsymbol{v} = V_0 \boldsymbol{p} + \boldsymbol{u}. \tag{1.1}$$

Moreover, the director vector evolves according to Jeffery's equation [15] [8] which is valid for ellipsoids

$$\dot{\boldsymbol{p}} = (\mathbb{I} - \boldsymbol{pp}) \cdot (\beta \mathbb{E} + \mathbb{W}) \cdot \boldsymbol{p}, \tag{1.2}$$

where $\mathbb{E} = 1/2(\nabla \boldsymbol{u} + \nabla \boldsymbol{u}^{\mathrm{T}})$ is the strain rate tensor, $\mathbb{W} = 1/2(\nabla \boldsymbol{u} - \nabla \boldsymbol{u}^{\mathrm{T}})$ is the vorticity tensor, and β is the Bretherton coefficient, which depends on the swimmer's shape. For rods, discs and spheres, $\beta \approx 1$, -1, and 0, respectively. For *E. Coli* $\beta \approx 0.7$ [16]. In a uniform shear flow, the evolution of the orientation and the position in eqs. (1.2) and (1.1), for non-tumbling bacteria, describes Jeffery's orbits as shown in fig. 1.1. These are cycloid-like orbits with a characteristic length $L_J \sim V_0/\dot{\gamma}$ and period $T_J \sim 1/\dot{\gamma}$, where $\dot{\gamma}$ is the shear rate, that in a simple shear flow relates to the fluid velocity by $\boldsymbol{u} = \dot{\gamma} y \hat{\boldsymbol{x}}$. The effect of the diffusion (spatial and rotational) and the tumbling is to migrate between Jeffery's orbits.

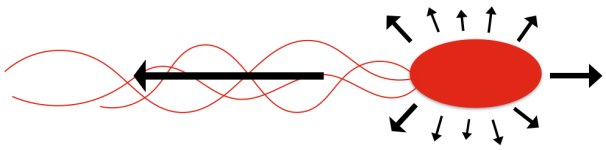

Figure 1.2: Representation of the force density over the surface of a swimmer.

1.3 Swimming at Low Reynolds Number

E. Coli is one of the best-known bacteria. We know its genome, metabolism and propulsion mechanisms [21] [5]. Their typical volume, speed, and mass density are, respectively, Vol = $1\,\mu\text{m}^3$, $V_0 = 10\,\mu\text{m/s}$, and $\rho_{\text{mass}} = 1\,\text{g/cm}^3$. Considering that these bacteria are immersed in water (which has a viscosity $\eta \approx 10^{-3}\,\text{Ns/m}^2$ at room temperature), they are characterized by a low Reynold's number: $Re \sim 10^{-5}$. Therefore the evolution of the fluid is described by the incompressible Stokes equation:

$$-\eta\nabla^2\boldsymbol{u} + \nabla p = \boldsymbol{F}, \tag{1.3}$$

$$\nabla \cdot \boldsymbol{u} = 0, \tag{1.4}$$

where η is the viscosity of the fluid, p is the pressure, and $\boldsymbol{F}$ accounts for the external forces. In this regime, inertia is completely neglected, therefore the objects (in this case swimmers) experience null total force and null total torque.

The propulsion of a swimmer involves forces exerted to the fluid. If $\boldsymbol{f}$ is the force density acting on the fluid on the surface of the swimmer (see fig. 1.2 for a reference), then we must have

$$\int_S \boldsymbol{f}\mathrm{d}^2S = 0. \tag{1.5}$$

Moreover, the velocity field generated by a force density can be obtained by solving eq. 1.3 using the Green method

$$\boldsymbol{u}(\boldsymbol{r}) = \int_S \mathbb{A}(\boldsymbol{r} - \boldsymbol{R}_{\text{cm}} - \boldsymbol{\rho}) \cdot \boldsymbol{f}(\boldsymbol{\rho})\mathrm{d}^2S, \tag{1.6}$$

where $\boldsymbol{R}_{\text{cm}}$ is the center of mass position of the bacteria, $\boldsymbol{\rho}$ is the relative position from the center of mass reference, and $\mathbb{A}$ is the Green function of the Stokes equation, which in 3D takes the form $\mathbb{A}(\boldsymbol{r}) = \frac{1}{8\pi\eta r}(\mathbb{I} + \boldsymbol{r}\boldsymbol{r}/r^2)$, called the Oseen tensor [19]. For the far field ($\rho \ll |\boldsymbol{r} - \boldsymbol{R}_{\text{cm}}|$), the velocity field can be expanded in multipoles of the force density

$$\boldsymbol{u}(\boldsymbol{r}) \approx \mathbb{A}(\boldsymbol{r} - \boldsymbol{R}_{\text{cm}}) \cdot \int_S \boldsymbol{f}(\boldsymbol{\rho})\mathrm{d}^2S - \frac{\partial \mathbb{A}}{\partial r_k} \cdot \int_S \rho_k \boldsymbol{f}(\boldsymbol{\rho})\mathrm{d}^2S. \tag{1.7}$$

The first term is zero, thus the lowest non-zero contribution is the dipolar one

$$\mathbb{D} = \int_S \boldsymbol{\rho}\boldsymbol{f}(\boldsymbol{\rho})\mathrm{d}^2S, \tag{1.8}$$

which is a symmetric tensor due to the vectorial nature of the force density and the fact that the total torque, which relates to the anti-symmetric part, is zero. This tensor can be

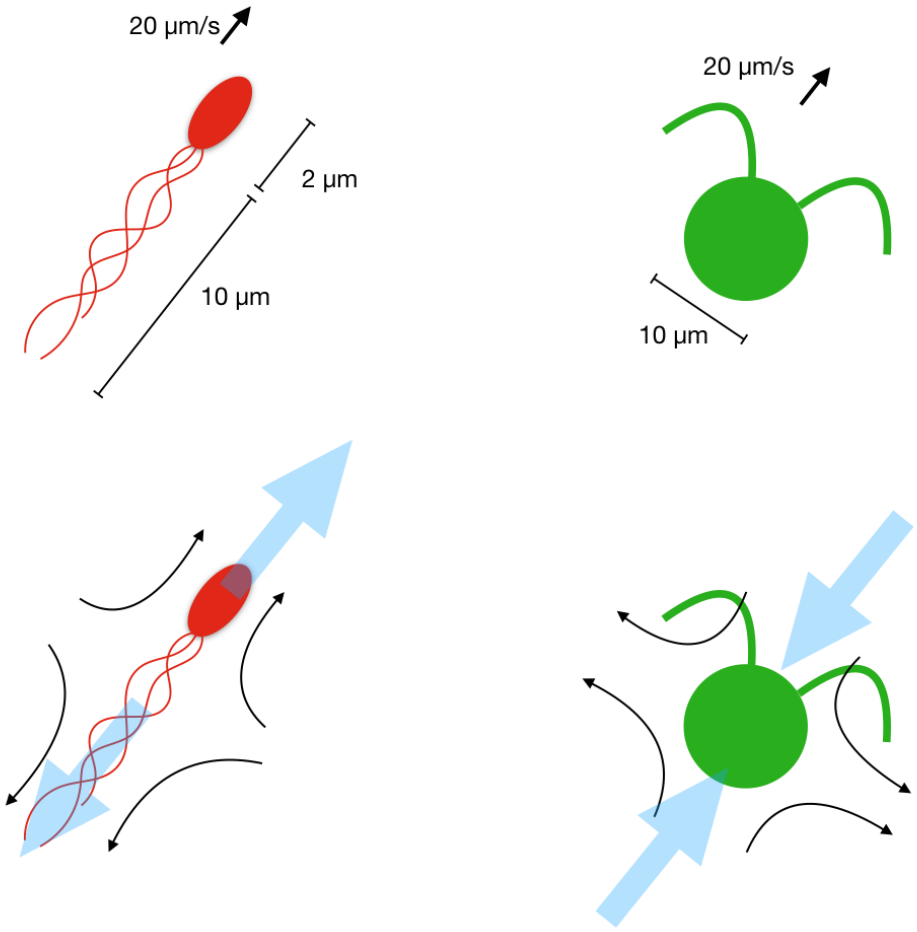

Figure 1.3: Dimensions (top) and flows (bottom) generated by the bacterium *E. Coli* (left) and the algae *Chlamydomonas Reinhardtii* (right). The dark arrows in the bottom image represent the velocity of the fluid near the swimmer. The pale blue arrows represent the dipole approximation for a pusher (left) and puller (right).

diagonalized in its principal axes, from which one coincides with the orientation $\boldsymbol{p}$ of the swimmer if it is axisymmetric. In 3D, this reduces to [34]

$$\mathbb{D} = \chi_0 \mathbb{I} - \sigma_0 \left(\boldsymbol{pp} - \frac{1}{3}\mathbb{I} \right). \tag{1.9}$$

The first contribution is isotropic and adds to the pressure. The second contribution is anisotropic and defines two categories of swimmers. If $\sigma_0 < 0$ the swimmer is classified as a *pusher* and if $\sigma_0 > 0$, as a *puller*. The difference relies on the directions in which the swimmer pushes and pulls the fluids as shown in fig. 1.3. *E. Coli* corresponds to the first case, with $|\sigma_0| \approx 2.3\,\mathrm{pN\,\mu m}$ [13] whereas algae such as *Chlamydomonas Reinhardtii* are classified as pullers.

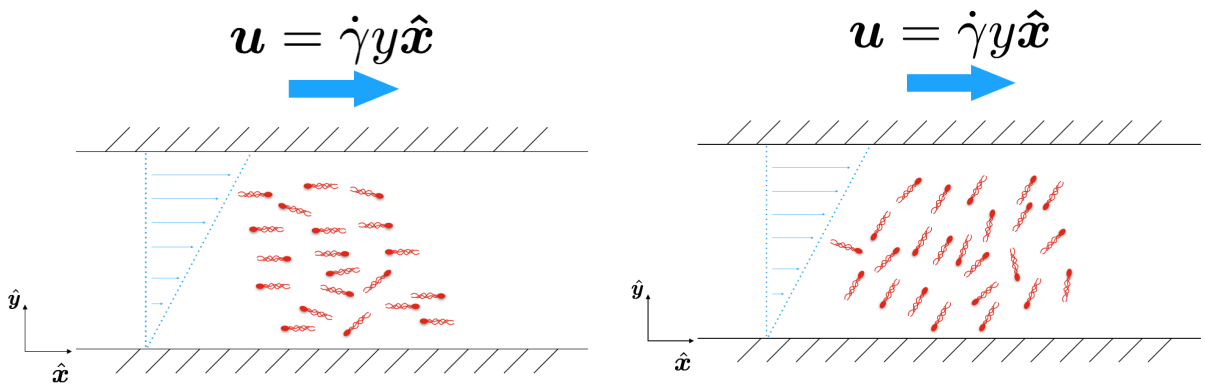

Figure 1.4: Representation of a bacterial suspension in a simple shear flow at a given time. Left (right) plot corresponds to the case without (with) rotational diffusion. When considering the rotational diffusion, the majority of the bacteria are nearly aligned with the velocity profile, inducing a non-zero active shear stress.

1.4 Bacterial Suspensions and Rheology

A bacterial suspension of number density ρ generates an active stress contribution corresponding to the configuration average over all orientations of the force dipole of each swimmer, $\mathbb{\Sigma}^{\mathrm{s}} = \rho \langle \mathbb{D} \rangle$, where $\langle \cdot \rangle$ denotes ensemble average. It can be seen as well as the nematic order parameter weighted by the local concentration [35]. In the absence of external flow, the bacteria orient isotropically, leading to an additional term that can be absorbed into the pressure (see eq. (1.9)). Nevertheless, if there is an imposed flow, there is going to be a preferred direction leading to a non-zero active shear stress. This is a result of the interplay between the Jeffery's orbit and the rotational diffusion. Indeed, if we ignore the rotational diffusion and consider a simple shear flow $\boldsymbol{u} = \dot{\gamma} y \hat{\boldsymbol{x}}$, the evolution of the orientation of each swimmer is completely given by eq. (1.2), which in two dimensions is $\dot{\theta} = \frac{\dot{\gamma}}{2}[\beta \cos(2\theta) - 1]$, where the angle θ is defined from the $\hat{\boldsymbol{x}}$ axis counterclockwise. Therefore, due to the symmetry under reflection of the Jeffery's equation in the y-axis, on average we would find the same amount of bacteria aligned in θ and in $\pi - \theta$, so the force dipoles cancel. We note, however, that the distribution in this case is not isotropic since there are two orientations in which the swimmer spend more time (*i.e.* in which the angular speed is minimum), namely $\theta = 0$ and $\theta = \pi$ (see fig. 1.4 (left)).

When considering the rotational diffusion, the symmetry is shifted towards the velocity profile. This can be seen from the xy component of the nematic tensor, which is proportional to the active stress and was obtained analytically in the dilute regime: $\langle \cos\theta \sin\theta \rangle \propto \frac{4\dot{\gamma}/D_{\mathrm{r}}}{16+(\dot{\gamma}/D_{\mathrm{r}})^2}$ [33], where $\langle \cdot \rangle$ denotes ensemble average. In this case, the majority of the bacteria are aligned with the velocity profile as depicted in fig. 1.4 (right). We note that in the limit $D_{\mathrm{r}} \to 0$, $\langle \cos\theta \sin\theta \rangle$ goes to zero as expected.

This preferred direction leads to a non-zero active stress, that can decrease or augment the passive stress [14] [37] [30]. We can define the active viscosity as the ratio between the

active shear stress and the shear rate,

$$\eta^{\mathrm{act}} = \frac{\Sigma^{\mathrm{s}}_{xz}}{\dot{\gamma}}. \tag{1.10}$$

This contribution to the fluid viscosity can be negative enough (for pushers) so that the total viscosity becomes zero or even negative [24], i.e. the bacterial suspension does work on the rheometer.

The interactions between bacteria can be classified as short and long-range. For the first case, we have binary collisions that align them (as seen in experiments [38] and in simulations [23]) in a polar or nematic way (as shown in figs. 2.2 and 2.3, respectively), due to steric and hydrodynamic interactions. For the second case, the interaction is mediated by the fluid: due to the propulsion of the swimmer, it produces a perturbation in the flow that decays as $1/r^2$ in three dimensions. This perturbation can be sensed by other bacteria, advecting and rotating them. Moreover, this long-range interaction must be accounted for each swimmer so it is convenient to use a mean field approximation, in which each bacterium swims in the flow perturbed by the active stress defined before. The active contribution acts as a source in the Stokes equation, modifying the velocity of the fluid and therefore the dynamics of the swimmers (see eqs. (1.1) and (1.2)).

When increasing the density, the mean free path of the bacteria decreases, thus the short-range interactions dominate over the long-range hydrodynamic interactions. As a result, flocks may emerge [44], as well as active turbulence [48]. In contrast, long-range interactions can lead to instabilities in a suspension of pushers [35].

1.5 Kinetic Theories

One way to study the rheology and, in general, the phenomenology of bacterial suspensions is through kinetic theories. This statistical approach is valid since, for example, the number of bacteria present in a mililiter at a very dilute concentration (volume fraction of 0.01) is $\sim 10^{10}$. The main object under study is the distribution function of bacteria $\Psi(t, \boldsymbol{r}, \boldsymbol{p})$ such that $\Psi \mathrm{d}\boldsymbol{r}\mathrm{d}\boldsymbol{p}$ gives the number of bacteria in a given position and orientation. The orientational moments of the distribution function lead to the number density, the average orientation, and the nematic tensor, which are the macroscopic variables that are usually measured experimentally. Besides, kinetic theories have successfully described the spatial localization of microtubules with polar interaction [2] [3] and the rheology of bacterial suspensions in the dilute regime [33], the two basic ingredients from which we are going to build the kinetic theory in the semidilute regime.

1.6 Methodology, Objectives, Thesis Organization.

This thesis employs both theory and simulations. From the theoretical point of view, it uses kinetic theory tools, linear stability analysis and asymptotic techniques. Regarding the

simulations, it uses particle-based methods with a statistical sampling of the collisions.

The organization of this thesis is as follow: in chapter 2 we present the kinetic equation for bacterial suspensions in two and three dimensions, extending the dilute regime to the semi-dilute case, in which binary collision between bacteria take place, accounting for steric and hydrodynamic effects, and the long-range hydrodynamic are ignored. In chapter 3 we describe the polar and nematic transition in two-dimensional homogeneous suspensions and how these phases modify the active shear stress. We employ a multi-scale scheme to analyze the evolution of the polar and nematic parameters close to the phase transition, finding an asymptotic characterization of the active shear stress. Analogously, chapter 4 describes the different phases for magnetotactic bacterial suspensions exposed to a constant magnetic field and how it modifies the rheology of the system. In chapter 5 we study inhomogeneous suspensions in two and three dimensions by exploring different boundary conditions, employing simulations and performing a linear stability analysis of the homogeneous solutions. Finally, in chapter 6 we present the conclusions and discuss two different paths for future work: the study of the response of the fluid under the shear rate obtained in a dilute suspension and the study of the phenomenology of dense magnetotactic bacterial suspensions confined in droplets.

Chapter 2

Semidilute Regime of Two- and Three-Dimensional Suspensions

Summary

In this chapter we derive the kinetic equation for the distribution function of positions and orientations of the swimmers. We extend the previous kinetic equation known for dilute suspensions [33], which does not take into account any interaction between swimmers. We describe two types of short-range interaction through the addition of a Boltzmann-like term: polar and nematic aligning collisions. In addition, we present in detail the equations related to a two-dimensional bacterial suspension in a uniform shear flow, by expanding the distribution function in angular Fourier series.

2.1 Kinetic Equation

The evolution of the distribution function $\Psi(t, \boldsymbol{r}, \boldsymbol{p})$ involves several factors as discussed in the Introduction. First, we have a streaming term originated by the evolution of the independent variables $\boldsymbol{r}$ and $\boldsymbol{p}$, given by eqs. (1.1) and (1.2), respectively. Ignoring all the other effects, we have $\Psi(\boldsymbol{r}, \boldsymbol{p}, t + \Delta t) = \Psi(\boldsymbol{r} - \dot{\boldsymbol{r}}\Delta t, \boldsymbol{p} - \dot{\boldsymbol{p}}\Delta t, t)$, and by Taylor expanding we get the following kinetic equation

$$\frac{\partial \Psi}{\partial t} + \frac{\partial}{\partial \boldsymbol{r}} \cdot (\dot{\boldsymbol{r}}\Psi) + \nabla_{\boldsymbol{p}} \cdot (\dot{\boldsymbol{p}}\Psi) = 0, \tag{2.1}$$

where $\nabla_{\boldsymbol{p}} = (\mathbb{I} - \boldsymbol{pp}) \cdot \frac{\partial}{\partial \boldsymbol{p}}$ is the gradient projected onto the unit sphere. This condition comes as a direct consequence of the fact that $\boldsymbol{p}$ is a unit vector, and therefore has just two degrees of freedom, which are the polar and azimuthal angle in spherical coordinates.

Next, we have diffusion in the two independent variables: a spatial (Brownian) diffusion and a rotational diffusion. The former can act differently in each direction, so in general, there is an anisotropic diffusivity tensor $D_{\mathrm{i}j}$ which for axisymmetric bodies can be encoded in just two variables: the diffusivity in the axial direction $D_{||}$ and perpendicular to it $D_{\perp}$, so the diffusivity tensor can be written as $D_{\mathrm{i}j} = D_{||} p_{\mathrm{i}} p_j + D_{\perp}(\delta_{\mathrm{i},j} - p_{\mathrm{i}} p_j)$ with $\delta_{\mathrm{i},j}$ being

the Kronecker delta. The rotational diffusion can be encoded in just one variable D_r for axisymmetric swimmers. Adding the diffusion to the eq. (2.1) gives

$$\frac{\partial \Psi}{\partial t} + \frac{\partial}{\partial \boldsymbol{r}} \cdot (\dot{\boldsymbol{r}}\Psi) + \nabla_{\boldsymbol{p}} \cdot (\dot{\boldsymbol{p}}\Psi) = \partial_\mathrm{i} D_{\mathrm{i}j} \partial_j \Psi + D_r \nabla^2_{\boldsymbol{p}} \Psi. \tag{2.2}$$

Finally, we have scattering and collision terms that change the distribution function. These terms are added to the right-hand side (RHS) of eq. (2.2). The tumble phenomenon presented in the introduction can be modelled as an isotropic Poissonian process with a characteristic correlation time τ:

$$T[\Psi] = \frac{1}{\tau}\left(\frac{\rho}{4\pi} - \Psi\right), \tag{2.3}$$

where the first term in the RHS accounts for the gain term in which bacteria are distributed isotropically, and the second term represents the loss term, which gives the number of swimmers that were swimming with an orientation $\boldsymbol{p}$ and performed a tumble. The tumbling can be further generalized by adding a kernel $W(\boldsymbol{p}, \boldsymbol{p}')$ depending on the initial orientation $\boldsymbol{p}'$.

The collision processes between bacteria are included via a Boltzmann-like term $J[\Psi, \Psi]$ that depends quadratically on the distribution function since we just consider binary collisions. In sections 2.2 and 2.3 we discuss the polar and nematic collisions respectively.

The kinetic equation, describing the evolution of the distribution function $\Psi(t, \boldsymbol{r}, \boldsymbol{p})$ considering all the ingredients already discussed, is

$$\frac{\partial \Psi}{\partial t} + \frac{\partial}{\partial \boldsymbol{r}} \cdot (\boldsymbol{v}\Psi) + \nabla_{\boldsymbol{p}} \cdot (\dot{\boldsymbol{p}}\Psi) = \partial_\mathrm{i} D_{\mathrm{i}j} \partial_j \Psi + D_r \nabla^2_{\boldsymbol{p}} \Psi + T[\Psi] + J[\Psi, \Psi], \tag{2.4}$$

with

$$\boldsymbol{v} = V_0 \boldsymbol{p} + \boldsymbol{u}, \tag{2.5}$$

$$\dot{\boldsymbol{p}} = (\mathbb{I} - \boldsymbol{pp}) \cdot (\beta \mathbb{E} + \mathbb{W}) \cdot \boldsymbol{p}. \tag{2.6}$$

In two dimensions, β equals to 0 for discs and ± 1 for rods, being positive for rods moving in their axial direction, and negative for those that move perpendicularly to their axial direction. The fluid velocity is given by the incompressible Stokes equation

$$-\eta \nabla^2 \boldsymbol{u} + \nabla p = \nabla \cdot \mathbb{\Sigma}^{\mathrm{tot}} + \boldsymbol{F}_{\mathrm{ext}}, \tag{2.7}$$

$$\nabla \cdot \boldsymbol{u} = 0, \tag{2.8}$$

$$\mathbb{\Sigma}^{\mathrm{tot}} = \underbrace{\sigma_0 \left\langle \boldsymbol{pp} - \frac{1}{\mathrm{d}}\mathbb{I} \right\rangle}_{\mathbb{\Sigma}^{\mathrm{s}}} + \underbrace{\frac{\xi_\mathrm{r}}{2} \left\langle \boldsymbol{pppp} - \frac{1}{\mathrm{d}}\mathbb{I}\boldsymbol{pp} \right\rangle : \mathbb{E}}_{\mathbb{\Sigma}^{\mathrm{drag}}}, \tag{2.9}$$

$$+ \text{Boundary Conditions (BC)}. \tag{2.10}$$

where ξ_r is the rotational friction coefficient, which can be computed from slender body theory as $\xi_\mathrm{r} = \pi\eta L/(3\ln(2L/a))$, with η being the viscosity of the fluid, L the total length of the swimmer, and a the equatorial diameter. $\boldsymbol{F}_{\mathrm{ext}}$ represents any external force and d is the dimension of the system. The first term in the RHS of (2.9) represents the active contribution to the stress which is originated from the self-propulsion of bacteria. The second

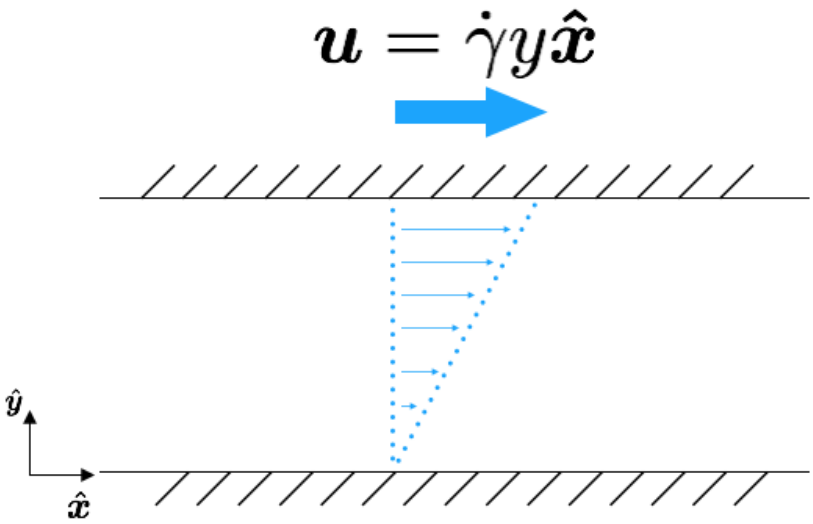

Figure 2.1: Uniform shear flow in $\hat{\boldsymbol{x}}$ and its gradient in $\hat{\boldsymbol{y}}$. The shear rate is $\dot{\gamma}$.

term is a passive contribution that accounts for the drag on the surface of the swimmers due to the resistance to be stretched or compressed by the local fluid flow. In general, the active contribution is much greater than the passive one since the latter depends on higher order orientational moments.

Since the Brownian diffusivity is much smaller than the Berg diffusivity [5], an outcome of the random reorientation of the bacteria, the translational diffusion is negligible. In addition, the tumbling term T, at long times, acts as a rotational diffusion [33] so it can be absorbed into the rotational diffusion coefficient D_{r}. Besides, in the semidilute regime we neglect the long-range hydrodynamic interactions and just consider the short-range aligning collisions [48] [12], so $\boldsymbol{u}$ corresponds to the imposed flow.

In 2D, eq. (2.4) reduces to

$$\frac{\partial \Psi}{\partial t} + \frac{\partial (\dot{x}\Psi)}{\partial x} + \frac{\partial (\dot{y}\Psi)}{\partial y} + \frac{\partial (\dot{\theta}\Psi)}{\partial \theta} = D_r \frac{\partial^2 \Psi}{\partial \theta^2} + J[\Psi, \Psi], \tag{2.11}$$

where $\boldsymbol{p} = (\cos\theta, \sin\theta)$.

We will focus our attention on a uniform shear flow, which can be obtained in a Couette configuration and locally represents any smooth flow. The fluid velocity is given by $\boldsymbol{u} = u(y)\hat{\boldsymbol{x}} = \dot{\gamma} y \hat{\boldsymbol{x}}$, where $\dot{\gamma}$ is the shear rate (see fig. 2.1). In this case, the velocity of a swimmer is given by $\boldsymbol{v} = (V_0 \cos\theta + \dot{\gamma} y)\hat{\boldsymbol{x}} + V_0 \sin\theta \hat{\boldsymbol{y}}$, and the Jeffery's equation (1.2) reads

$$\dot{\theta} = \frac{\dot{\gamma}}{2}[\beta \cos(2\theta) - 1]. \tag{2.12}$$

For circular swimmers $\beta = 0$, eq. (2.12) reduces to $\dot{\theta} =$ constant, so they rotate at a constant angular speed. However, for non-circular swimmers, the rotation is slower when they are nearly aligned with the flow, and faster when they are aligned perpendicularly to it.

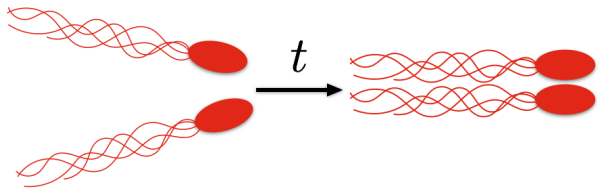

Figure 2.2: Completely inelastic polar alignment: when two bacteria collide, they end up with the same orientation equal to the average of the pre-collisional orientations.

Regarding the short-range interactions, it has been observed that bacteria align with each other due to hydrodynamic and steric effects. As a consequence, they tend to align in a polar and/or nematic way, so the collision integral, in the most general case, can be expressed as $J = g_1 J_{\text{polar}} + g_2 J_{\text{nematic}}$, where g_1 and g_2 are proportional to the collision rates accounting for polar and nematic alignment, respectively. Furthermore, both kinds of interactions depend on the incidental orientations, aligning bacteria only if the relative angle between them is less than a certain threshold angle. Finally, in reality this alignment process is not perfect, in the sense that an angle difference after the interaction may remain. In what follows, we analyze both kinds of interactions independently, *i.e.* $g_1 = 0$ or $g_2 = 0$ in order to facilitate the calculations.

2.2 Polar Alignment

For simplicity we consider the completely polar aligning case: when two bacteria meet they end up with the same orientation, equal to the average of the pre-collisional orientations shown in fig. 2.2. Moreover, we consider that two bacteria interact regardless of their initial orientation. In this case, the collisions are accounted by a Boltzmann-like term under the Maxwell approximation, *i.e.* the cross-section does not depend on the incidental angles [2] [3]:

$$J[\Psi,\Psi] = g \int \mathrm{d}^{\mathrm{d}-1}p_1 \mathrm{d}^{\mathrm{d}-1}p_2 \Psi(\boldsymbol{p}_1)\Psi(\boldsymbol{p}_2) \left[\delta\left(\boldsymbol{p} - \frac{\boldsymbol{p}_1 + \boldsymbol{p}_2}{|\boldsymbol{p}_1 + \boldsymbol{p}_2|} \right) - \delta(\boldsymbol{p} - \boldsymbol{p}_2) \right]. \tag{2.13}$$

Here g is parameter proportional to the collision rate, which is estimated as $g = V_0\sigma$, where σ is the effective cross-section, and δ is the Dirac delta function. The first term in the RHS of eq. (2.13) represents the gain term, that is, all the bacteria that after a collision process end up with an orientation $\boldsymbol{p}$. Analogously, the second term represents the loss term, *i.e.* all the bacteria that lost their pre-collisional orientation $\boldsymbol{p}$.

In 2D, for *E. Coli*, $V_0 \approx 20\,\mu\text{m/s}$ and $\sigma_{2D} \approx 2\,\mu\text{m}$, so $g \approx 40\,\mu\text{m}^2/\text{s}$, and the collision integral can be expressed as

$$J_{2D}[\Psi,\Psi] = g \int_{-\pi}^{\pi} \mathrm{d}w \left[\Psi(\theta + w/2)\Psi(\theta - w/2) - \Psi(\theta)\Psi(\theta - w) \right], \tag{2.14}$$

where the Dirac deltas have been explicitly integrated.

This model was used to describe the polar transition of non-propelling microtubules without imposed flow as well as the spatial structures such as vortices and asters [2] [3]. Likewise, this model was used to describe the transient spatiotemporal patterns in thin film concentrated bacterial suspensions [1].

To solve eq. (2.11) considering (2.14), we decompose the distribution function in angular Fourier series

$$\Psi(t,x,y,\theta)=\sum_n a_n(t,x,y)\mathrm{e}^{\mathrm{i}n\theta}, \tag{2.15}$$

so the kinetic equation reads

$$\begin{aligned}\frac{\partial a_n}{\partial t}=&-a_n\left(D_{\mathrm{r}}n^2-\frac{\mathrm{i}n\dot{\gamma}}{2}+g\rho\right)+\frac{V_0}{2}\left[\left(\frac{\partial a_{n+1}}{\partial x}+\frac{\partial a_{n-1}}{\partial x}\right)+\mathrm{i}\left(\frac{\partial a_{n+1}}{\partial y}-\frac{\partial a_{n-1}}{\partial y}\right)\right]\\&+\dot{\gamma}y\frac{\partial a_n}{\partial x}-\frac{\mathrm{i}\dot{\gamma}\beta n}{4}\left(a_{n-2}+a_{n+2}\right)+2\pi g\sum_l a_l a_{n-l}\mathrm{sinc}\left(n\pi/2-l\pi\right),\end{aligned} \tag{2.16}$$

where $\mathrm{sinc}(x)=\sin(x)/x$ and $a_0=\rho/(2\pi)$ due to the normalization condition $\int\Psi\mathrm{d}\theta=\rho$, with ρ being the bacteria number density.

2.3 Nematic Alignment

For elongated bacteria such as Bacilus Subtilis, there have been different observations indicating that they interact nematically [25], *i.e.* swimmers with opposite orientations tend to align so they are anti-parallel, whereas if they are swimming in a similar direction they align polarly.

As before, to facilitate the calculations we consider the completely aligning case and that two bacteria interact regardless of their initial orientation. In this situation, however, the alignment is polar if the pre-collisional angle is smaller than $\pi/2$ and apolar if it is greater than that (see fig. 2.3). The collision operator in 2D reads

$$\begin{aligned}J[\Psi,\Psi]=&g\Bigg[\int_{-\pi/2}^{\pi/2}\mathrm{d}w\Psi(\theta+w/2)\Psi(\theta-w/2)+\int\limits_{[-\pi,-\frac{\pi}{2}]\cup[\frac{\pi}{2},\pi]}\Psi(\theta+w/2+\pi/2)\Psi(\theta-w/2+\pi/2)\\&-\int_{-\pi}^{\pi}\Psi(\theta)\Psi(\theta-w)\Bigg],\end{aligned} \tag{2.17}$$

and the equation for each of the Fourier amplitudes is given by

$$\begin{aligned}\frac{\partial a_n}{\partial t}=&-a_n\left(D_{\mathrm{r}}n^2-\frac{\mathrm{i}n\dot{\gamma}}{2}+g\rho\right)+\frac{V_0}{2}\left[\left(\frac{\partial a_{n+1}}{\partial x}+\frac{\partial a_{n-1}}{\partial x}\right)+\mathrm{i}\left(\frac{\partial a_{n+1}}{\partial y}-\frac{\partial a_{n-1}}{\partial y}\right)\right]+\dot{\gamma}y\frac{\partial a_n}{\partial x}\\&-\frac{\mathrm{i}\dot{\gamma}\beta n}{4}\left(a_{n-2}+a_{n+2}\right)+2\pi g\sum_l a_l a_{n-l}\left[\mathrm{i}^n\mathrm{sinc}\left((n/2-l)\pi\right)+\frac{\cos\left((l-n/2-1)\frac{\pi}{2}\right)}{(l-n/2)\pi}(1-\mathrm{i}^n)\right].\end{aligned} \tag{2.18}$$

Figure 2.3: Completely inelastic nematic alignment: when two bacteria collide, they end up with the same orientation equal to the average of the pre-collisional orientations if the angle between them is smaller than $\pi/2$, otherwise they end up with anti-parallel orientations.

Chapter 3

Rheology of Two-Dimensional Homogeneous Suspensions

Summary

In this chapter we study the kinetic equation in two dimensions for a homogeneous suspension under a uniform shear flow, considering polar and nematic interactions. We find that there are polar and nematic phase transitions, respectively. In particular, we study two scenarios: circular swimmers, for which we can find a direct connection with a suspension in a quiescent fluid, and rod-shaped swimmers. Near the transition point, for rod-shaped swimmers, it is possible to truncate the series expansions up to the second Fourier mode. It is possible as well to obtain analytical solutions based on a multi-scale scheme, in which we adopt a particular ansatz based on scalings behaviors found in suspensions without imposed flows [2] [3]. The results show that the polar and nematic phases rotate in time due to the imposed vorticity, which leads to a time-oscillatory behavior of the active shear stress, with an average close to the non-interacting case. This behavior is also shown by numerical solutions considering more terms in the angular Fourier expansion. Finally, the polar and nematic phases disappear for high shear rates $\dot{\gamma}$, and in particular, for the nematic case, it disappears in a subcritical transition.

3.1 Polar Alignment

We first consider the case with polar alignment. For a homogeneous suspension, eq. (2.16) simplifies to

$$\frac{\partial \Psi}{\partial t} + \frac{\partial(\dot{\theta}\Psi)}{\partial \theta} = D_r \frac{\partial^2 \Psi}{\partial \theta^2} + J[\Psi, \Psi]. \tag{3.1}$$

It is worth pointing out that eq. (3.1) presents no activity: a suspension of passive rods would behave in the same way. Then, what does activity mean? There are two sources of

activity in the most general case. First, we have the self-propulsion, which is manifest in the streaming motion of the kinetic equation and does not appear in the homogeneous case, and second, there is the force dipole, which is a product of the self-propulsion, and generates an active stress on the fluid. This imprint of activity is still present in a homogenous system and is what makes the difference between an active and a passive suspension.

Assuming no dependence in space, the kinetic equation expanded in angular Fourier modes (2.16) reduces to

$$\dot{a}_n = -a_n\left(n^2 - \frac{\mathrm{i}n\dot{\gamma}}{2} + \rho\right) - \frac{\mathrm{i}\dot{\gamma}\beta n}{4}\left(a_{n-2} + a_{n+2}\right) + 2\pi\sum_l a_l a_{n-l}\mathrm{sinc}\left(n\pi/2 - l\pi\right), \tag{3.2}$$

where we used the following rescaled variables

$$t \to D_\mathrm{r} t, \tag{3.3}$$

$$\dot{\gamma} \to \dot{\gamma}/D_\mathrm{r}, \tag{3.4}$$

$$a_n \to a_n g/D_\mathrm{r}. \tag{3.5}$$

Note that $\dot{a}_0 = 0$ reflecting that the density is conserved in a homogenous system.

In terms of the Fourier coefficients, the swimming contribution to the shear stress is

$$\Sigma^\mathrm{s}_{xy} = -\sigma_0\pi\mathrm{Im}(a_2). \tag{3.6}$$

Likewise, the drag contribution is given by

$$\Sigma^\mathrm{drag}_{xy} = \dot{\gamma}\frac{\xi_\mathrm{r} D_\mathrm{r}\pi}{8}\left(\frac{\rho}{2\pi} - \mathrm{Re}(a_4)\right). \tag{3.7}$$

Finally, another quantity of interest is the average of the orientation vector

$$\langle \boldsymbol{p}\rangle = \frac{2\pi}{\rho}\begin{pmatrix}\mathrm{Re}(a_1)\\ -\mathrm{Im}(a_1)\end{pmatrix}. \tag{3.8}$$

The rotational diffusion gives rise to a fast decay of the high n modes. Then, it is possible to truncate eq. (3.2) with few modes, as the rest will take small values. Considering that the swimming contribution to the stress tensor depends on a_2 and that the polar order that results from the short-range interactions are characterized by a_1, we first truncate the series to $n = 2$. Furthermore, the drag contribution to the stress tensor is roughly a constant (see eq. (3.7)) since it depends on the number density, which is conserved and therefore a constant in the homogeneous case, and on the fourth mode, which is much smaller than the second mode. We define the bifurcation parameter [2]

$$\varepsilon = \rho(4/\pi - 1) - 1 = \frac{\rho - \rho_\mathrm{c}}{\rho_\mathrm{c}}, \tag{3.9}$$

such that the critical density for the isotropic to polar transition corresponds to $\varepsilon = 0$, that is for $\rho_\mathrm{c} g/D_\mathrm{r} = 3.66$. For *E. Coli*, $\rho_\mathrm{c} \approx 6\times10^{-4}\,\mu\mathrm{m}^{-3}$, which translate to a volume fraction of approximately 0.06%. The equations for a_1 and a_2 are

$$\dot{a}_1 = a_1\left(\frac{\mathrm{i}\dot{\gamma}}{2} + \varepsilon\right) - \frac{\mathrm{i}\beta\dot{\gamma}}{4}a_{-1} - \frac{8}{3}a_{-1}a_2, \tag{3.10}$$

$$\dot{a}_2 = -\frac{\mathrm{i}\beta\dot{\gamma}\rho_\mathrm{c}}{4\pi}\left(\varepsilon + 1\right) - \left[4 - \mathrm{i}\dot{\gamma} + \rho_\mathrm{c}(\varepsilon+1)\right]a_2 + 2\pi a_1^2. \tag{3.11}$$

3.1.1 Circular Swimmers: $\beta = 0$

For circular swimmers ($\beta = 0$) the equations for a_1 and a_2 read

$$\dot{a}_1 = a_1 \left(\frac{\mathrm{i}\dot{\gamma}}{2} + \varepsilon \right) - \frac{8}{3} a_{-1} a_2, \tag{3.12}$$

$$\dot{a}_2 = -\left[4 - \mathrm{i}\dot{\gamma} + \rho_{\mathrm{c}}(\varepsilon + 1) \right] a_2 + 2\pi a_1^2. \tag{3.13}$$

Changing variables $a_n = c_n \mathrm{e}^{\mathrm{i}\frac{\dot{\gamma}}{2} nt}$ we recover the equations for inelastic interactions of polar rods in absence of flow, but this time for c_n

$$\dot{c}_1 = c_1 \varepsilon - \frac{8}{3} c_{-1} c_2, \tag{3.14}$$

$$\dot{c}_2 = -[4 + \rho_{\mathrm{c}}(\varepsilon + 1)] c_2 + 2\pi c_1^2. \tag{3.15}$$

Therefore, there is a polar phase transition that leads to a spontaneous symmetry breaking as in the polar rods system. Indeed, near the transition $\varepsilon = 0$, the growth rate of c_1 is much smaller than the decaying rate of c_2, so we can approximate $\dot{c}_2 \approx 0$, obtaining $c_2 = 2\pi(4 + \rho)^{-1} c_1^2$ which leads to a supercritical equation for c_1

$$\dot{c}_1 = \varepsilon c_1 - A_0 |c_1|^2 c_1, \tag{3.16}$$

with

$$A_0 = \frac{16\pi}{3(4 + \rho)} \approx \frac{16\pi}{3(4 + \rho_c)} + O(\rho - \rho_c). \tag{3.17}$$

Thus, for $\rho > \rho_c$ or equivalently $\varepsilon > 0$, there is an orientation transition, going from $|c_1| = 0$ to a finite value $|c_1| = \sqrt{\varepsilon / A_0}$ with a random phase ϕ selected in the symmetry breaking process, so $c_1 = \sqrt{\varepsilon / A_0} \mathrm{e}^{\mathrm{i}\phi}$. The same transition is found for a_1 when $\dot{\gamma} = 0$, recovering the equations for the inelastic interaction of polar rods presented by Aranson and Tsimring [2] [3]. This analysis leads to $a_1 \propto \sqrt{\varepsilon}$ and $a_2 \propto \varepsilon$.

Once in the polar phase, we note that due to the change of variables, a_n has a constant module with a rotating phase. In particular, $a_2 = c_2 \mathrm{e}^{\mathrm{i}\dot{\gamma} t}$ therefore, the active shear stress becomes

$$\Sigma_{xy}^{\mathrm{act}} = -\sigma_0 \pi \mathrm{Im}(a_2) = -\sigma_0 \pi \sqrt{\varepsilon / A_0} \cos\left(\phi + \dot{\gamma} t \right), \tag{3.18}$$

that is, it oscillates around zero, which is a direct consequence of setting $\beta = 0$ as we show in the next section. The reason behind it is the symmetry of the swimmer: since there is no preferred axis, the swimmer rotates at a constant rate under the uniform flow as can be seen in eq. (2.12) with $\beta = 0$.

3.1.2 Non-Circular Swimmers: $\beta \neq 0$.

Equations (3.10) and (3.11) are highly non-linear, but a detailed analysis can be performed close to the polar transition. How is the imposed flow going to modify the results obtained

from (3.14) and (3.15)? Once in the polar phase, the simple shear flow will induce a macroscopic rotation of $\langle \boldsymbol{p} \rangle$. Thus, a_1 and a_2 will not be stationary, but instead oscillations will appear. For $|\varepsilon| \ll 1$ a multiple time scale approach is possible, where we define the fast and slow time scales $s_0 = t$, $s_1 = \varepsilon t$, and $s_2 = \varepsilon^2 t$. Based on the couplings in eqs. (3.10) and (3.11), we propose the following ansatz

$$a_1(s_0, s_1, s_2) = A\mathrm{e}^{\mathrm{i}\omega_0 s_0 + \mathrm{i}\omega_1 s_1} + B\mathrm{e}^{-\mathrm{i}\omega_0 s_0 - \mathrm{i}\omega_1 s_1} \tag{3.19}$$

$$a_2(s_0, s_1, s_2) = F\mathrm{e}^{2\mathrm{i}\omega_0 s_0 + 2\mathrm{i}\omega_1 s_1} + G\mathrm{e}^{-2\mathrm{i}\omega_0 s_0 - 2\mathrm{i}\omega_1 s_1} + H, \tag{3.20}$$

where A, B, F, G, and H depend solely on s_1 and s_2. Here we implicitly assume that $\dot{\gamma}$ is at least one order higher than ε so it makes sense to have several time scales: one for the oscillations and the other for the evolution of the amplitudes.

Inserting the ansatz in eqs. (3.10) and (3.11) and using that $A, B \propto \sqrt{\varepsilon}$, $F, G \propto \varepsilon$, and $H = H_0 + \varepsilon H_1$, with $H_0, H_1 \propto 1$, the equations are solved order by order. At order ε^0

$$H_0 = \frac{-\mathrm{i}\beta\dot{\gamma}\rho_\mathrm{c}}{4\pi} \frac{1}{\rho_\mathrm{c} + 4 - \mathrm{i}\dot{\gamma}}. \tag{3.21}$$

Then, at order $\varepsilon^{1/2}$

$$\begin{pmatrix} -6\mathrm{i}(\dot{\gamma} - 2\omega_0) & 32H_0 + 3\mathrm{i}\beta\dot{\gamma} \\ 32H_0^* - 3\mathrm{i}\beta\dot{\gamma} & 6\mathrm{i}(\dot{\gamma} + 2\omega_0) \end{pmatrix} \begin{pmatrix} A \\ B^* \end{pmatrix} = 0. \tag{3.22}$$

Imposing a null determinant, we get $\omega = \pm\omega(\dot{\gamma}, \beta) \approx \pm\dot{\gamma}/2 + O(\beta)$. For $\beta = 0.7$, $\omega \approx 0.468\dot{\gamma}$. At order ε^2, expressions for H_1, F and G are obtained, which are plotted in fig. 3.1.

$$H_1 = \underbrace{\frac{-\mathrm{i}\beta\dot{\gamma}\rho_\mathrm{c}/(4\pi) - \rho_\mathrm{c}H_0}{\rho_\mathrm{c} + 4 - \mathrm{i}\dot{\gamma}}}_{\equiv \bar{H}} + \underbrace{\frac{4\pi}{\rho_\mathrm{c} + 4 - \mathrm{i}\dot{\gamma}}}_{\equiv \bar{\bar{H}}} \frac{AB}{\varepsilon} \tag{3.23}$$

$$F = \underbrace{\frac{2\pi}{\rho_\mathrm{c} + 4 - \mathrm{i}(\dot{\gamma} - 2\omega_0)}}_{\equiv g_1} A^2 \tag{3.24}$$

$$G = \underbrace{\frac{2\pi}{\rho_\mathrm{c} + 4 - \mathrm{i}(\dot{\gamma} + 2\omega_0)}}_{\equiv g_2} B^2 \tag{3.25}$$

Finally, substituting all these results into the order $\varepsilon^{3/2}$ equation gives

$$\frac{\mathrm{d}A}{\mathrm{d}s_1} = A\left[\varepsilon(1 - \mathrm{i}\omega_1) - \frac{8}{3}\left(g_1|A|^2 + \bar{\bar{H}}|B|^2\right)\right] - \frac{8}{3}\varepsilon\bar{H}B^*, \tag{3.26}$$

$$\frac{\mathrm{d}B}{\mathrm{d}s_1} = B\left[\varepsilon(1 + \mathrm{i}\omega_1) - \frac{8}{3}\left(g_2|B|^2 + \bar{\bar{H}}|A|^2\right)\right] - \frac{8}{3}\varepsilon\bar{H}A^*. \tag{3.27}$$

The crossed term $\varepsilon\bar{H}$ is small compared to the other terms and, therefore, can be neglected (see fig. 3.2). In the steady state of the s_1 time-scale we have that whether A or B has to be zero, otherwise we would obtain an inconsistency such as $|A|^2$ being a complex number. Numerical results show that the system selects $B = 0$. If this is the case, then $A = 0$ or

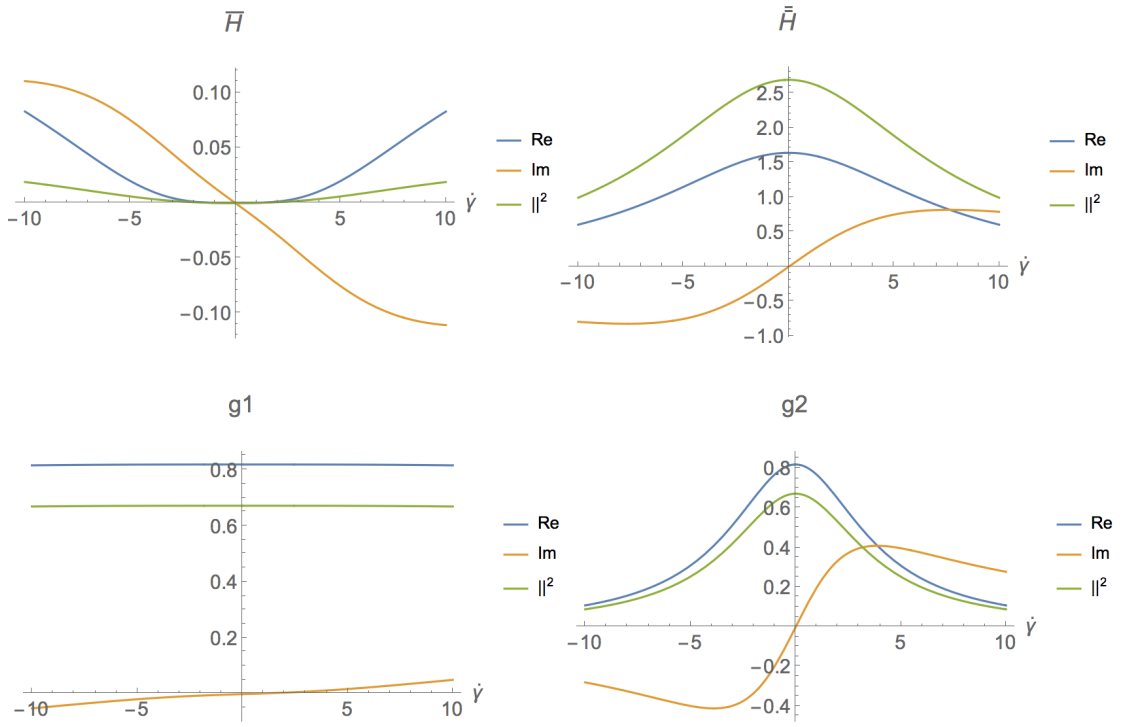

Figure 3.1: Real part, imaginary part, and modulus squared of the different coefficients of eqs. (3.26) and (3.27), as a function of the shear rate $\dot{\gamma}$ for $\beta = 0.7$.

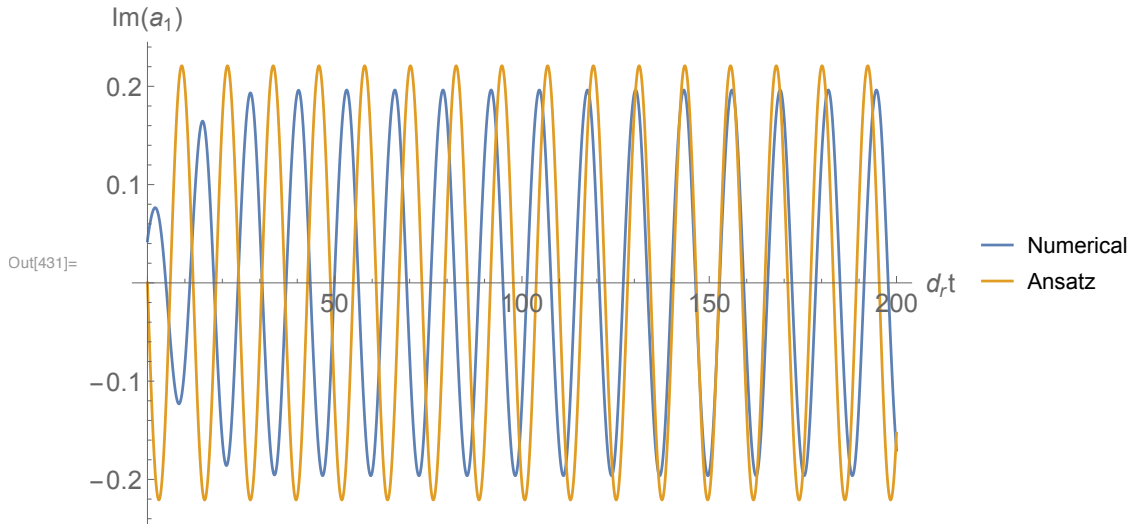

Figure 3.2: Comparison between solution of eqs. (3.26) and (3.27) (up to $n = 2$), and ansatz based on $\omega = \omega_0 + \varepsilon\omega_1$. $\varepsilon = 0.1$, $\dot{\gamma} = 1$, and $\beta = 0.7$.

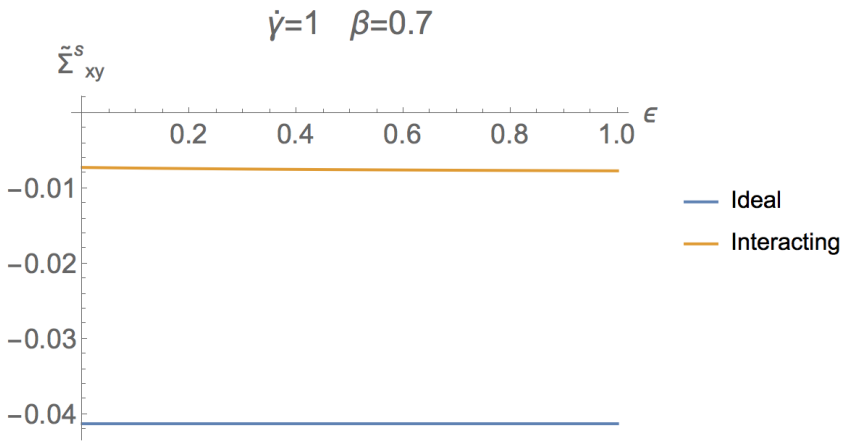

Figure 3.3: Comparison between the shear stress obtained in the interacting and ideal case, as a function of ε, for a suspension of pushers ($\sigma_0 < 0$).

$|A|^2 = \frac{3\varepsilon}{8}\frac{1-i\omega_1}{g_1}$. The latter solution is only valid if it is a real positive number. This condition gives us the value $\omega_1 = \mathrm{Im}(g_2)/\mathrm{Re}(g_2)$, and therefore $|A|^2 = \frac{3\varepsilon}{8\mathrm{Re}(g_1)}$. This analysis agrees with the numerical solutions of eqs. (3.10) and (3.11) truncating to $n = 2$ as shown in fig. 3.2, where there is a just a difference in phase.

One important result is that the oscillatory behavior of a_2 leads to an oscillatory active shear stress, with period $T \sim 1/\dot{\gamma}$, according to (3.6). In fact, using the ansatz, the active shear stress ((3.6)) reads

$$\begin{aligned}
\Sigma^{\mathrm{s}}_{xy} \approx & -\sigma_0\pi\mathrm{Im}\left(F\mathrm{e}^{2\mathrm{i}(\omega_0+\varepsilon\omega_1)s_0} + G\mathrm{e}^{-2\mathrm{i}(\omega_0+\varepsilon\omega_1)s_0} + H\right) \\
\approx & -\sigma_0\pi\mathrm{Im}\left[\frac{3\varepsilon}{8}\mathrm{e}^{2\mathrm{i}(\omega_0+\varepsilon\omega_1)s_0+\mathrm{i}\phi} - \frac{\mathrm{i}\beta\dot{\gamma}\rho_c}{4\pi(\rho_c+4-\mathrm{i}\dot{\gamma})}\left(1+\varepsilon+\frac{\varepsilon}{\rho_c+4-\mathrm{i}\dot{\gamma}})\right)\right] \\
= & -\sigma_0\pi\left\{\frac{3\varepsilon}{8}\sin\left(2(\omega_0+\varepsilon\omega_1)s_0+\phi\right)\right. \\
& \left. -\frac{\beta\dot{\gamma}\rho_c\left[4(16+\dot{\gamma}^2)(1+\varepsilon)+(48+32\varepsilon+\dot{\gamma}^2(1+2\varepsilon))\rho_c+4(3+\varepsilon)\rho_c^2+\rho_c^3\right]}{4\pi(16+\dot{\gamma}^2+8\rho_c+\rho_c^2)^2}\right\},
\end{aligned} \tag{3.28}$$

where ϕ is a free phase. In the first line we used the ansatz and in the second line we use the approximation $B \approx 0$ and $\omega_0 \approx \dot{\gamma}/2$. Taking the time average of the former expression over a period $2\pi/(\omega_0+\varepsilon\omega_1)$ we have

$$\left\langle\Sigma^{\mathrm{s}}_{xy}\right\rangle_t \approx \sigma_0\pi\frac{\beta\dot{\gamma}\rho_c\left[4(16+\dot{\gamma}^2)(1+\varepsilon)+(48+32\varepsilon+\dot{\gamma}^2(1+2\varepsilon))\rho_c+4(3+\varepsilon)\rho_c^2+\rho_c^3\right]}{4\pi(16+\dot{\gamma}^2+8\rho_c+\rho_c^2)^2}, \tag{3.29}$$

which is greater than the value obtained in the ideal gas approximation $\Sigma^{\mathrm{s}}_{xy_{\mathrm{Ideal}}} \approx \frac{\sigma_0\beta\dot{\gamma}\rho_c(\varepsilon+1)}{(16+\dot{\gamma}^2)}$ obtained by Saintillan [33] and, in our case, by setting $g = 0$, as shown in fig. 3.3 (where we show a dimensionless version of the shear stress $\tilde{\Sigma}^{\mathrm{s}} = \Sigma^{\mathrm{s}}/(\rho|\sigma_0|)$). Unlike the circular swimmers case, this time we have a non-zero time average for the active shear stress, which is proportional to β as can be seen from $H = H_0 + \varepsilon H_1$ in eqs. (3.21) and (3.23).

The amplitude of the shear stress oscillations can be obtained analytically under the

approximation $A \approx 0$, obtaining $|\sigma_0|\pi 3\varepsilon/4$. Likewise, the root mean square is given by.

$$\sqrt{\left\langle (\Sigma^{\mathrm{s}}_{xy})^2 \right\rangle_t} \approx \sigma_0 \pi \sqrt{\frac{9\varepsilon^2}{128} + \left(\frac{\beta\dot{\gamma}\rho_c \left[4(16+\dot{\gamma}^2)(1+\varepsilon) + (48+32\varepsilon+\dot{\gamma}^2(1+2\varepsilon))\rho_c + 4(3+\varepsilon)\rho_c^2 + \rho_c^3 \right]}{4\pi(16+\dot{\gamma}^2+8\rho_c+\rho_c^2)^2} \right)^2}, \tag{3.30}$$

The standard deviation can be also obtained from eq. (3.28), giving

$$\sqrt{\left\langle (\Sigma^{\mathrm{s}}_{xy})^2 \right\rangle_t - \left\langle \Sigma^{\mathrm{s}}_{xy} \right\rangle_t^2} \approx 3\sigma_0 \pi \varepsilon \sqrt{2}/16. \tag{3.31}$$

An important consequence of the oscillatory active shear stress is that for certain configurations, it takes positive and negative values. Hence, a suspension of pushers would not only see a reduction of the viscosity but also an increase, when being in a peak and a valley, respectively. On average there is indeed a reduction in the viscosity that is smaller than in the ideal gas case.

It is worth pointing out that the oscillatory ansatz works up to order $a_{\pm 2}$. In fact, if we truncate up to $a_{\pm 3}$, then the evolution of each mode is given by

$$\dot{a}_1 = a_1 \left(\frac{\mathrm{i}\dot{\gamma}}{2} + \varepsilon \right) - \frac{\mathrm{i}\beta\dot{\gamma}}{4} a_{-1} - \frac{\mathrm{i}\beta\dot{\gamma}}{4} a_3 - \frac{8}{3} a_{-1} a_2 + \frac{8}{5} a_{-2} a_3, \tag{3.32}$$

$$\dot{a}_2 = -\frac{\mathrm{i}\beta\dot{\gamma}\rho_{\mathrm{c}}}{4\pi} (\varepsilon + 1) - \left[4 - \mathrm{i}\dot{\gamma} + \rho_{\mathrm{c}}(\varepsilon+1) \right] a_2 + 2\pi a_1^2, \tag{3.33}$$

$$\dot{a}_3 = -a_3 \left[9 - \frac{3\mathrm{i}}{2}\dot{\gamma} + \rho_c(\varepsilon+1)(1+\frac{4}{3\pi}) \right] - \frac{3\mathrm{i}\beta\dot{\gamma}}{4} a_1 + 8 a_1 a_2, \tag{3.34}$$

and the natural extension for the ansatz would be

$$a_1(s_0, s_1, s_2) = A\mathrm{e}^{\mathrm{i}\omega_0 s_0 + \mathrm{i}\omega_1 s_1} + B\mathrm{e}^{-\mathrm{i}\omega s_0 - \mathrm{i}\omega_1 s_1}, \tag{3.35}$$

$$a_2(s_0, s_1, s_2) = F\mathrm{e}^{2\mathrm{i}\omega s_0 + 2\mathrm{i}\omega_1 s_1} + G\mathrm{e}^{-2\mathrm{i}\omega s_0 - 2\mathrm{i}\omega_1 s_1} + H \tag{3.36}$$

$$a_3(s_0, s_1, s_2) = J\mathrm{e}^{\mathrm{i}\omega s_0 + \mathrm{i}\omega_1 s_1} + K\mathrm{e}^{-\mathrm{i}\omega s_0 - \mathrm{i}\omega_1 s_1} + P\mathrm{e}^{3\mathrm{i}\omega s_0 + 3\mathrm{i}\omega_1 s_1} + Q\mathrm{e}^{-3\mathrm{i}\omega s_0 - 3\mathrm{i}\omega_1 s_1}, \tag{3.37}$$

with the following scaling obtained from the case without flow: J, $K \propto \sqrt{\varepsilon}$, P, $Q \propto \varepsilon^{3/2}$ and the rest remains the same. Inserting the ansatz in eqs. (3.32), (3.33), and (3.34) we can solve to each order in ε. To order ε^0 we obtain the relation (3.21), which defines H_0. To order $\varepsilon^{1/2}$ we have

$$\begin{pmatrix} 30\mathrm{i}(\dot{\gamma} - 2\omega_0) & \alpha_1 & \alpha_2^* & 0 \\ \alpha_1^* & -30\mathrm{i}(\dot{\gamma} + 2\omega_0) & 0 & \alpha_2 \\ \alpha_3 & 0 & 18\mathrm{i}\pi\dot{\gamma} - 12\mathrm{i}\pi\omega_0 + \alpha_4 & 0 \\ 0 & \alpha_3^* & 0 & -18\mathrm{i}\pi\dot{\gamma} - 12\mathrm{i}\pi\omega_0 + \alpha_4 \end{pmatrix} \begin{pmatrix} A \\ B^* \\ J \\ K^* \end{pmatrix} = 0, \tag{3.38}$$

where $\alpha_1 = -160H_0 - 15\mathrm{i}\beta\dot{\gamma}$, $\alpha_2 = 96H_0 + 15\mathrm{i}\beta\dot{\gamma}$, $\alpha_3 = 96\pi H_0 - 9I\pi\beta\dot{\gamma}$, and $\alpha_4 = -\rho_c(12\pi + 16) - 108\pi$. We can obtain the frequency ω_0 by imposing null determinant. However, the frequencies obtained from this matrix have real and imaginary parts, meaning that the modes increase indefinitely or go to zero in the fast time scale s_0. This fact contradicts both the intuition and the numerical results shown next.

Numerical Results

We solve eq. (3.2) truncating to $n = 5$, for $\beta = 0.7$. In fig. 3.4 we show the active shear stress and the average of the orientation vector as a function of time. They reveal a polar phase transition for ε close to zero and the oscillatory behavior of the active shear stress, as predicted by the multi-scale analysis. We notice that the amplitude of the oscillations increases with ε and it is greater for small values of $\dot{\gamma}$.

However, by plotting the shear stress as a function of $\dot{\gamma}$ and ε, we notice that high shear rates impede the formation of the polar phase, as shown in fig. 3.6 and 3.8. This feature is solely due to higher order terms ($n > 2$), otherwise the transition remains even for large values of $\dot{\gamma}$. A complete picture of the transition can be found in the phase space shown in fig. 3.10, where we considered the following criterium to determine if a configuration belonged to a polar phase or not: if the difference between the maximum and minimum value of the dimensionless shear stress is smaller than 0.0001, then it belongs to the disordered phase, otherwise it is polarly ordered.

3.2 Nematic Alignment

In the homogeneous case, eq. (2.16) reduces to

$$\begin{aligned}\dot{a}_n =& -a_n\left(n^2 - \mathrm{i}n\dot{\gamma}/2 + \rho\right) - \mathrm{i}\dot{\gamma}\beta n/4\left(a_{n-2} + a_{n+2}\right)\\ &+ 2\pi\sum_l a_l a_{n-l}\Bigg[\mathrm{i}^n \mathrm{sinc}\left(n\pi/2 - l\pi\right)\\ &+ \frac{\cos\left((l - n/2 - 1)\pi/2\right)}{(l - n/2)\pi}(1 - \mathrm{i}^n)\Bigg],\end{aligned} \tag{3.39}$$

where we have used the same rescaling (3.3), (3.4), and (3.5). It is worth pointing out that the evolution of the even modes is decoupled from the odd ones, which is a direct consequence of the nematic symmetry present in the collision rule and the swimmer shape. On the contrary, the evolution of the odd modes does depend on the even modes.

As in the polar case, it is possible to truncate eq. (3.39) with few modes, as the rest will take small values due to the rotational diffusion. Nonetheless, this time we truncate the set of equations up to $a_{\pm 4}$ since the nematic interactions involve just even modes and in order to see a phase transition we need a non-linear coupling of a_2 and a_4. This reasoning is confirmed by the numerical results, which reveal that there is a nematic phase transition involving a_4. We define the bifurcation parameter

$$\nu = \rho(4/\pi - 1) - 4 = \varepsilon - 3 = \frac{\rho - 4\rho_\mathrm{c}}{\rho_\mathrm{c}}, \tag{3.40}$$

such that the critical density for the isotropic to nematic transition corresponds to $\nu = 0$. This time the critical density is four times bigger than in the polar case $\rho_c^{\mathrm{Nematic}} = 4\rho_c$. The

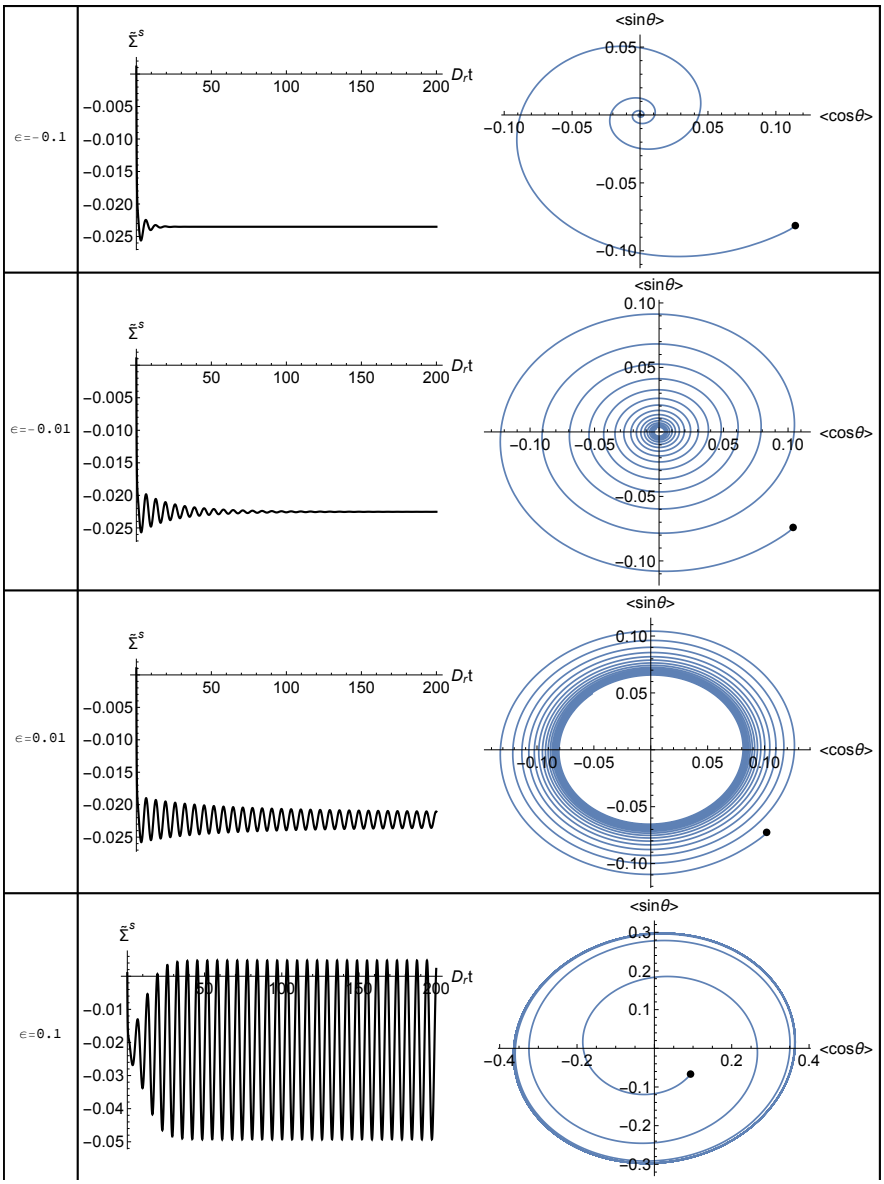

Figure 3.4: Dimensionless active shear stress $\tilde{\Sigma}^{\mathrm{s}}_{xy}$ as a function of time $D_{\mathrm{r}}t$ (left) and time evolution of the average orientation (right) for pushers with $\beta = 0.7$ and $\dot{\gamma} = 1$. The black dot in the right plots corresponds to the initial orientation.

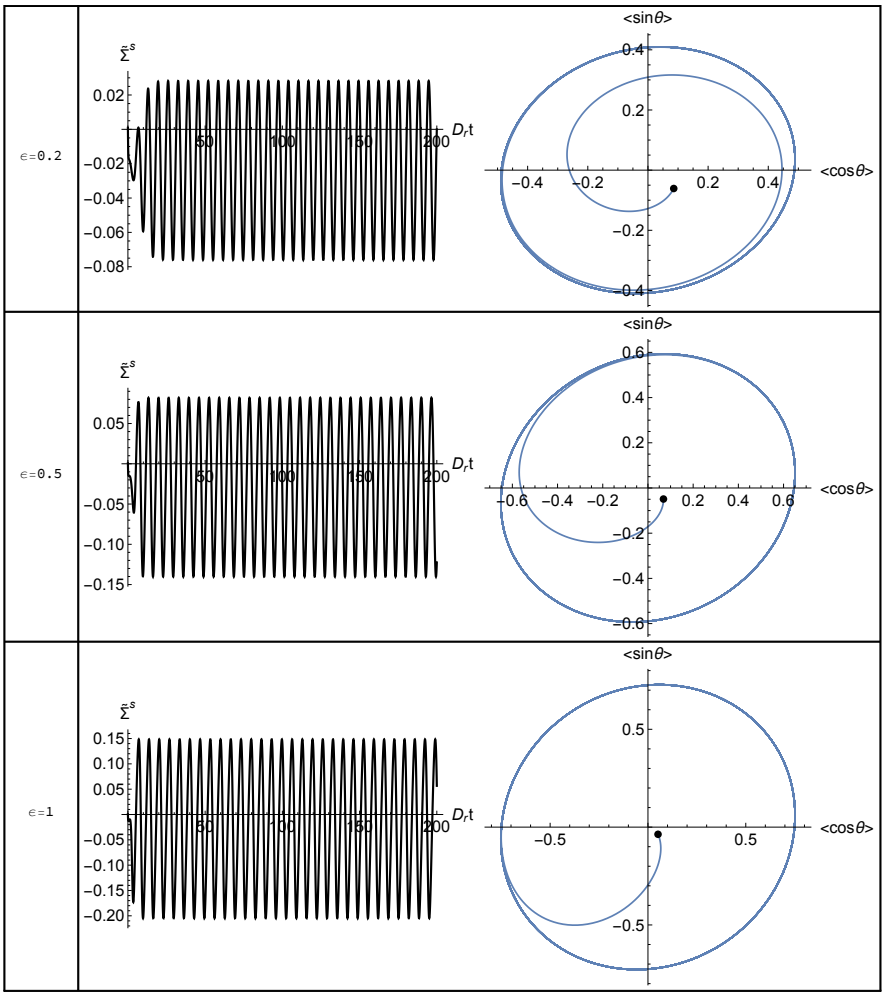

Figure 3.5: Continuation of fig. 3.4.

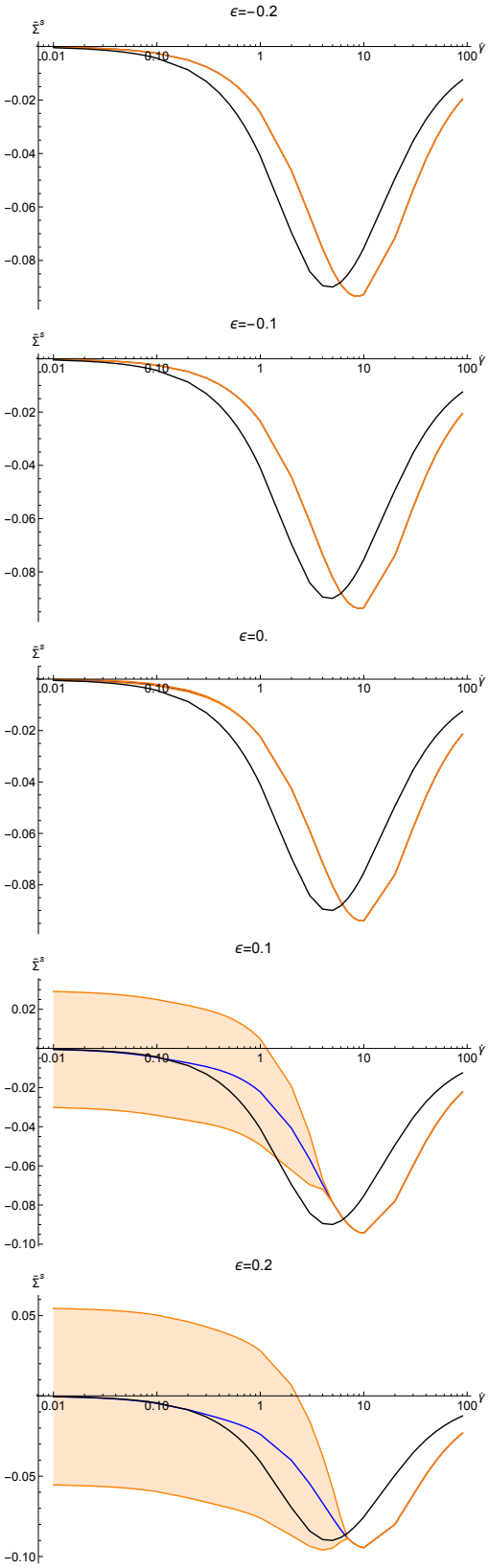

Figure 3.6: Dimensionless active shear stress $\tilde{\Sigma}^{\mathrm{s}}_{xy}$ as a function of $\dot{\gamma}$ for different concentrations (pushers with $\beta = 0.7$). The orange lines represent the maximum and minimum value for $\tilde{\Sigma}^{\mathrm{s}}_{xy}$, the blue line is the average between these two values, and the black line represents the ideal case.

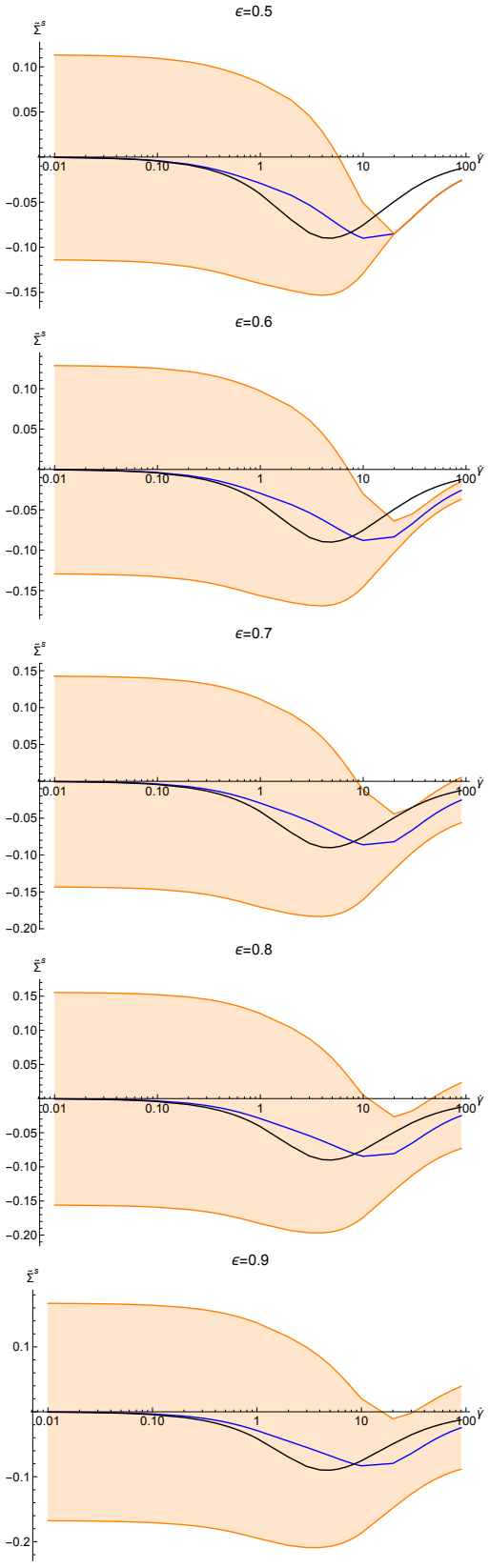

Figure 3.7: Continuation of fig. 3.6.

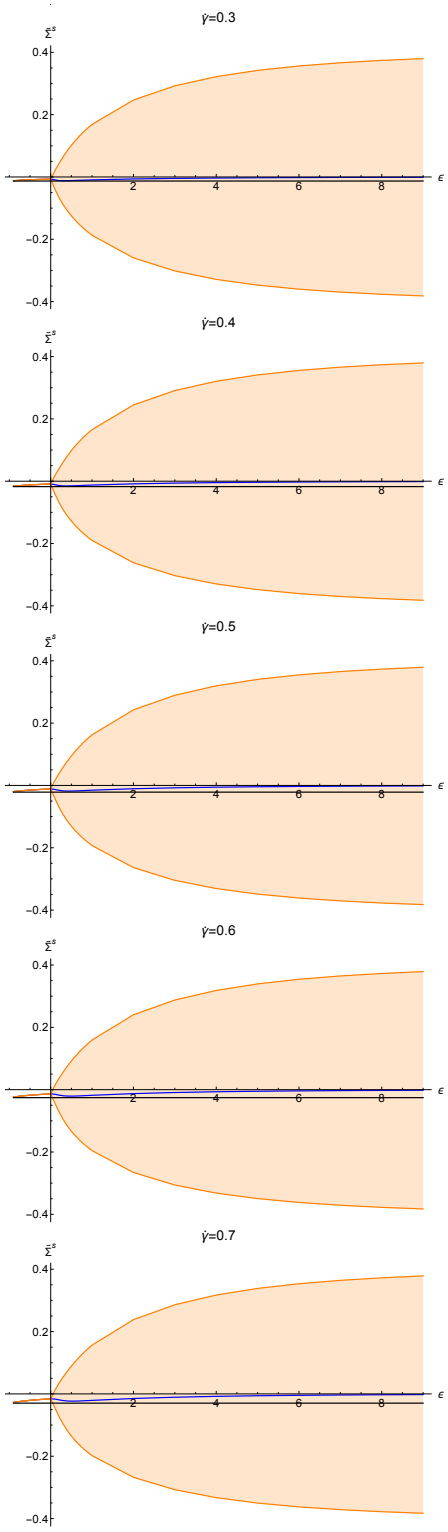

Figure 3.8: Dimensionless active shear stress $\tilde{\Sigma}^{\mathrm{s}}_{xy}$ as a function of ε for different shear rates (pushers with $\beta = 0.7$). The orange lines represent the maximum and minimum value for $\tilde{\Sigma}$, the blue line is the average between these two values, and the black line represents the ideal case.

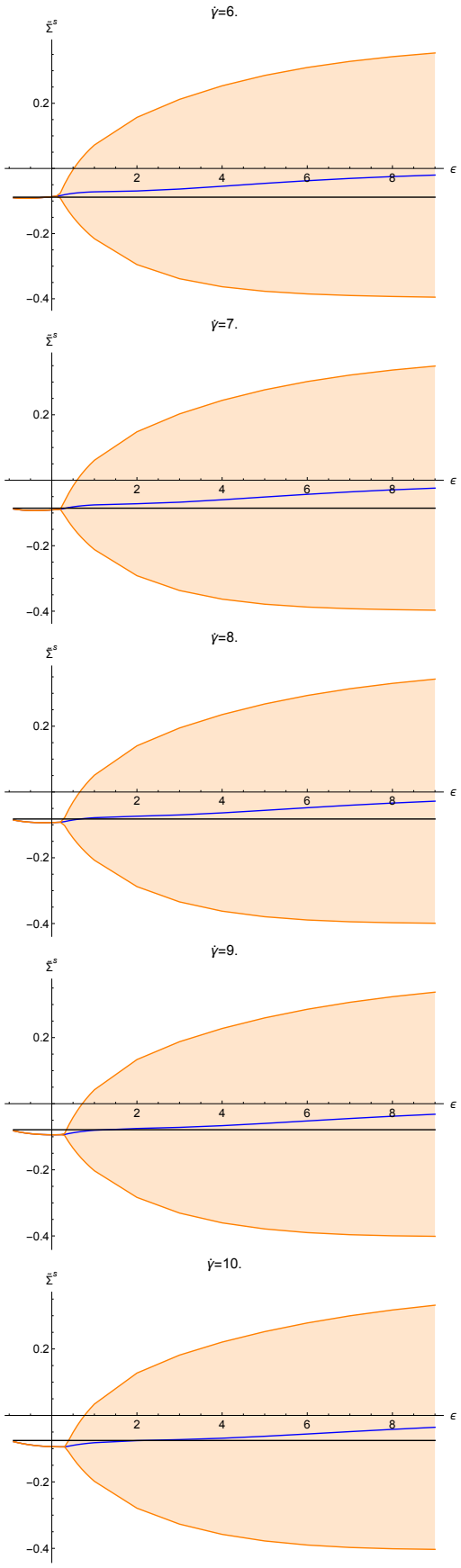

Figure 3.9: Continuation of fig. 3.8.

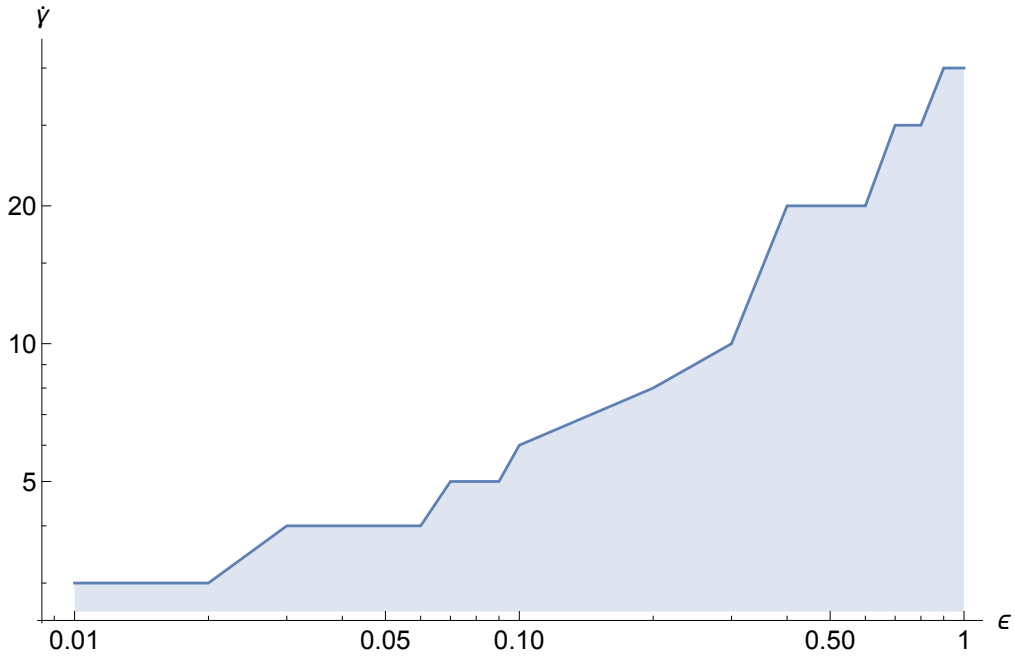

Figure 3.10: Transition diagram in the phase space formed by ε and $\dot{\gamma}$. The colored region indicates the polar phase.

equations for a_1, a_2, a_3 and a_4 are

$$\dot{a}_1 = -\left(1 - \mathrm{i}\frac{\dot{\gamma}}{2} + \rho_c(\nu+4)\left[1 - \frac{2}{\pi}\left(2\mathrm{i} + (1-\mathrm{i})\sqrt{2}\right)\right]\right)a_1 - \frac{\mathrm{i}\beta\dot{\gamma}}{4}a_{-1} - \frac{\mathrm{i}\beta\dot{\gamma}}{4}a_3 + \frac{4}{3}\left(-2\mathrm{i} + (1-\mathrm{i})\sqrt{2}\right)a_2a_{-1}$$
$$+ \frac{4}{5}\left(2\mathrm{i} - (1-\mathrm{i})\sqrt{2}\right)a_3a_{-2} + \frac{4}{7}\left(-2\mathrm{i} - (1-\mathrm{i})\sqrt{2}\right)a_4a_{-3}, \tag{3.41}$$

$$\dot{a}_3 = -\left(9 - \frac{3\mathrm{i}\dot{\gamma}}{2} + \rho_c(\nu+4)\left[1 - \frac{2}{3\pi}\left(2\mathrm{i} + (1+\mathrm{i})\sqrt{2}\right)\right]\right)a_3 - \frac{3\mathrm{i}\beta\dot{\gamma}}{4}a_1 + 4\left(-2\mathrm{i} + (1+\mathrm{i})\sqrt{2}\right)a_1a_2$$
$$+ \frac{4}{5}\left(-2\mathrm{i} - (1+\mathrm{i})\sqrt{2}\right)a_4a_1, \tag{3.42}$$

$$\dot{a}_2 = -\frac{\mathrm{i}\beta\dot{\gamma}\rho_c}{4\pi}(\nu+4) + a_2(\mathrm{i}\dot{\gamma} + \nu) - \frac{\mathrm{i}\beta\dot{\gamma}}{2}a_4 - \frac{8}{3}a_4a_{-2}, \tag{3.43}$$

$$\dot{a}_4 = -\left[16 - 2\mathrm{i}\dot{\gamma} + \rho_c(\nu+4)\right]a_4 + 2\pi a_2^2 - \mathrm{i}\beta\dot{\gamma}a_2. \tag{3.44}$$

If $\dot{\gamma} = 0$ we recover the same equations for the polar order transition found in interacting polar microtubules in absence of flow [2] [3], this time for the a_4 coefficient enslaved to a_2, and for the bifurcation parameter ν instead of ε. In addition, the numerical results reveal that all the odd coefficients rapidly decay to zero, even the first ones. This result is a consequence of the rotational diffusion (for high modes) and the nematic interaction for all the modes. Finally, the evolution of the distribution function is mainly governed by the even modes.

3.2.1 Circular Swimmers: $\beta = 0$

If $\beta = 0$, eqs. (3.43) and (3.44) read

$$\dot{a}_2 = a_2(\mathrm{i}\dot{\gamma} + \nu) - \frac{8}{3}a_{-2}a_4, \tag{3.45}$$

$$\dot{a}_4 = -(16 - 2\mathrm{i}\dot{\gamma} + \rho_\mathrm{c}(\nu + 4))a_4 + 2\pi a_2^2. \tag{3.46}$$

Using the same change of variables as in the polar case $a_n = c_n \mathrm{e}^{\mathrm{i}\frac{\dot{\gamma}}{2}nt}$ we recover the same phenomena found in [2] [3], this time for the variables c_2 and c_4

$$\dot{c}_2 = c_2\nu - \frac{8}{3}c_{-2}c_4, \tag{3.47}$$

$$\dot{c}_2 = -(16 + \rho_\mathrm{c}(\nu + 4))c_4 + 2\pi c_2^2. \tag{3.48}$$

As before, we can perform a detailed analysis close to the nematic transition $\nu = 0$, where the growth rate of c_2 is much smaller than the decaying rate of c_4, so the latter variable is enslaved by the former one: $c_4 = 2\pi(16+\rho)^{-1}c_2^2$. Inserting this expression in eq. (3.47) leads to a supercritical equation for c_2

$$\dot{c}_2 = \nu c_2 - B_0|c_2|^2 c_2, \tag{3.49}$$

with

$$B_0 = \frac{16\pi}{3(16+\rho)} \approx \frac{16\pi}{3(16+4\rho_\mathrm{c})} + O(\rho - 4\rho_\mathrm{c}). \tag{3.50}$$

A nematic transition occurs for $\nu > 0$, where the equilibrium stationary solution is $c_2 = \sqrt{\nu/B_0}\mathrm{e}^{\mathrm{i}\phi}$, with ϕ being a random phase. Although the mechanism and the transition are different from the polar case, the phenomena is the same: an oscillatory active shear stress with zero mean

$$\Sigma_{xy}^s = -\sigma_0\pi\mathrm{Im}(a_2) = -\sigma_0\pi\sqrt{\nu/B_0}\cos(\phi + \dot{\gamma}t). \tag{3.51}$$

3.2.2 Non-Circular Swimmers: $\beta \neq 0$

Solving numerically the eq. (3.39) up to $n = 5$, we obtain the same qualitative behavior as in the polar case, that is time oscillations in the active shear stress (see fig. 3.11). However, there is not a polar phase, and in fact the oscillation is caused by a nematic phase transition.

As before, we plot the shear stress as a function of $\dot{\gamma}$ and ε, noting that high shear rates impede the formation of the nematic phase, as shown in figs. 3.13, 3.14, 3.15, and 3.16. It is worth pointing out that the nematic phase disappears in a subcritical transition unlike the polar phase in section 3.1 (see fig. 3.17).

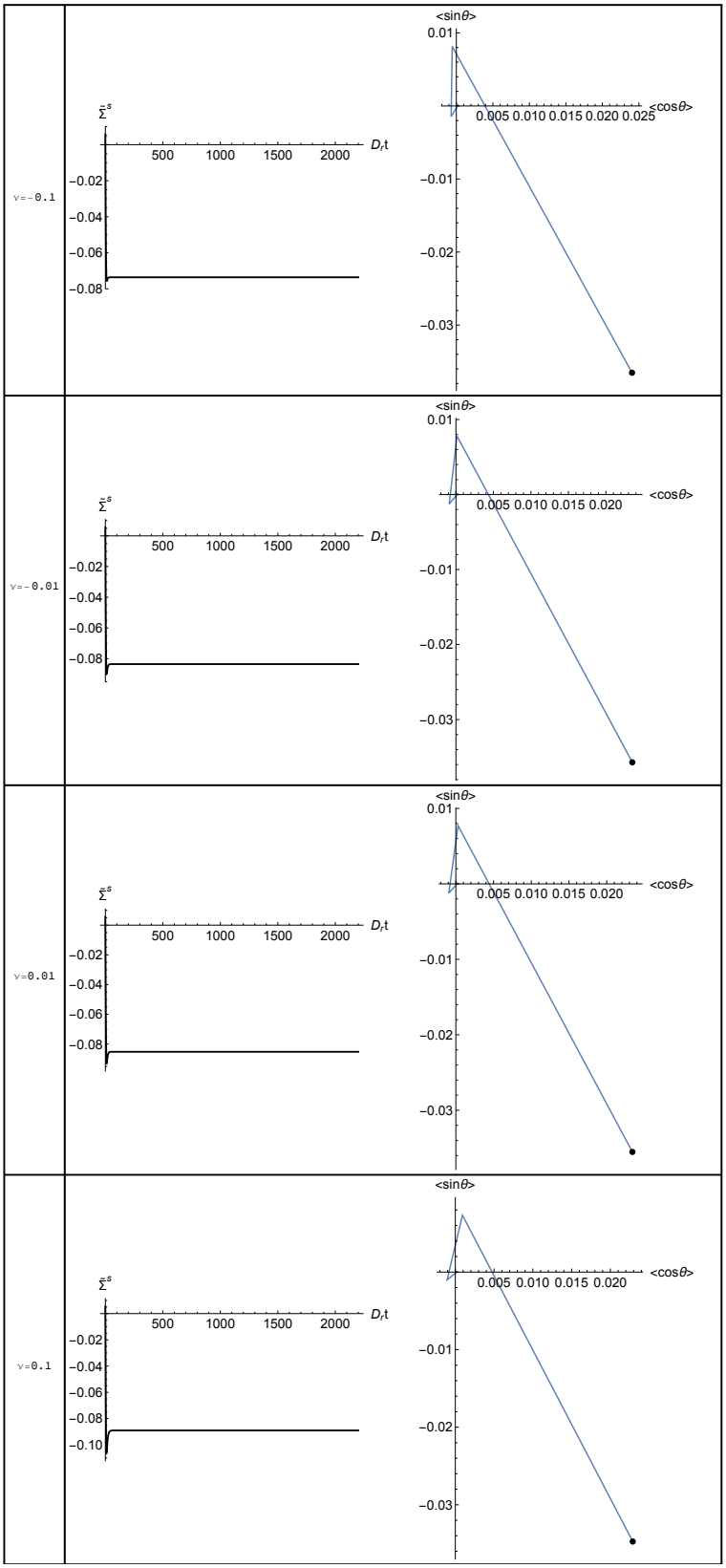

Figure 3.11: Dimensionless active shear stress $\tilde{\Sigma}^{\mathrm{s}}_{xy}$ as a function of time $D_{\mathrm{r}}t$ (left) and time evolution of the average orientation (right) for pushers with nematic alignment. $\beta = 0.7$, $\dot{\gamma} = 0.1$. The black dot in the left plots corresponds to the initial configuration.

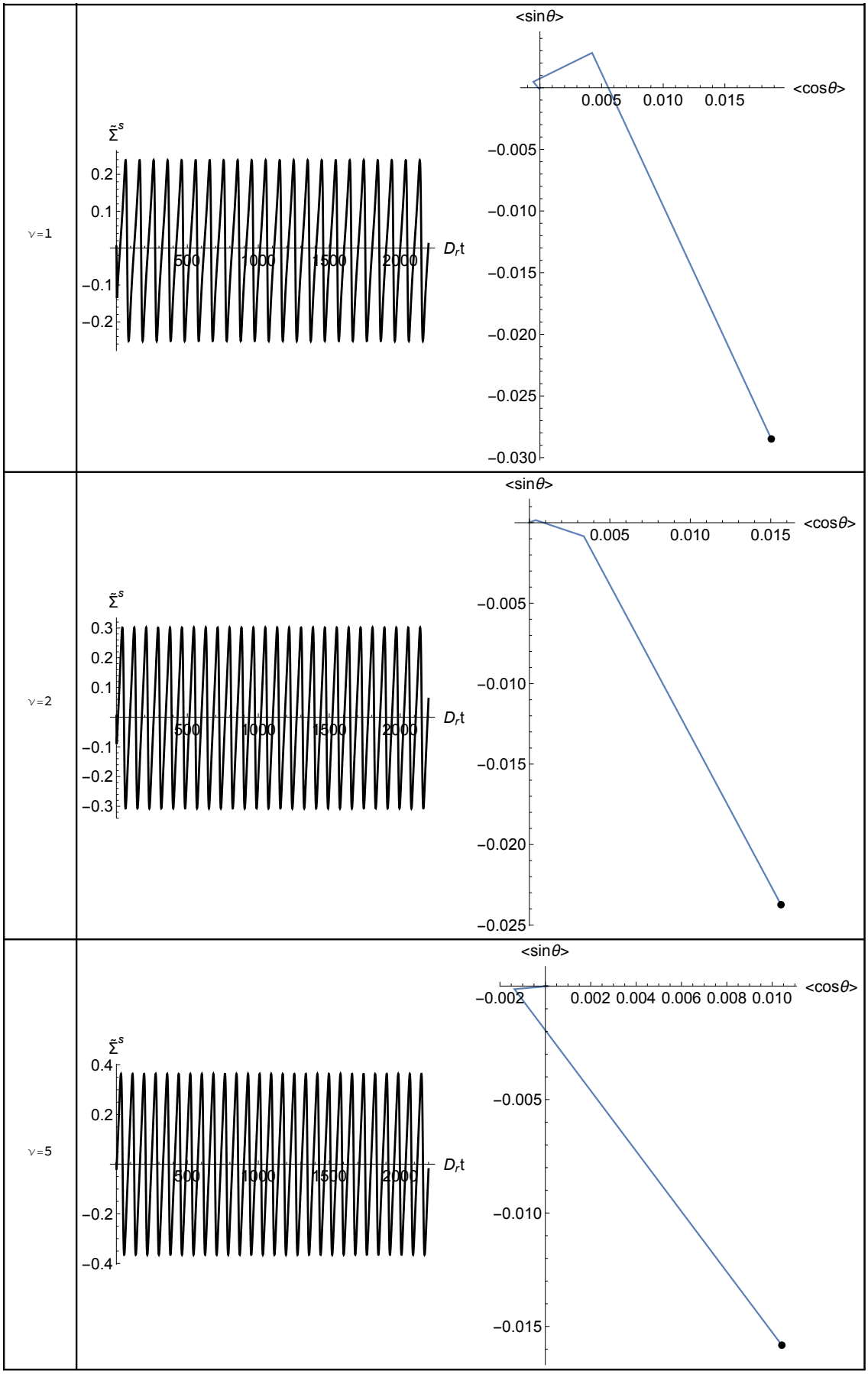

Figure 3.12: Continuation of fig 3.11.

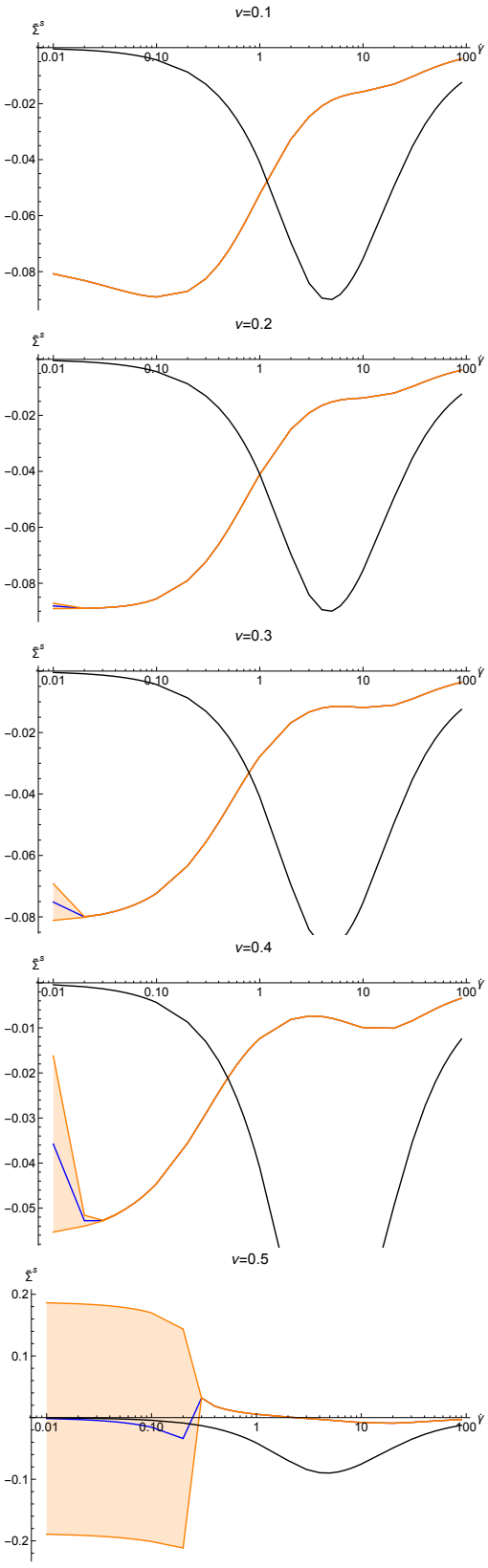

Figure 3.13: Dimensionless active shear stress $\tilde{\Sigma}^{\mathrm{s}}_{xy}$ as a function of $\dot{\gamma}$ for different concentration (pushers with $\beta = 0.7$). The orange lines represent the maximum and minimum value for $\tilde{\Sigma}$, the blue line is the average between these two values, and the black line represents the ideal case.

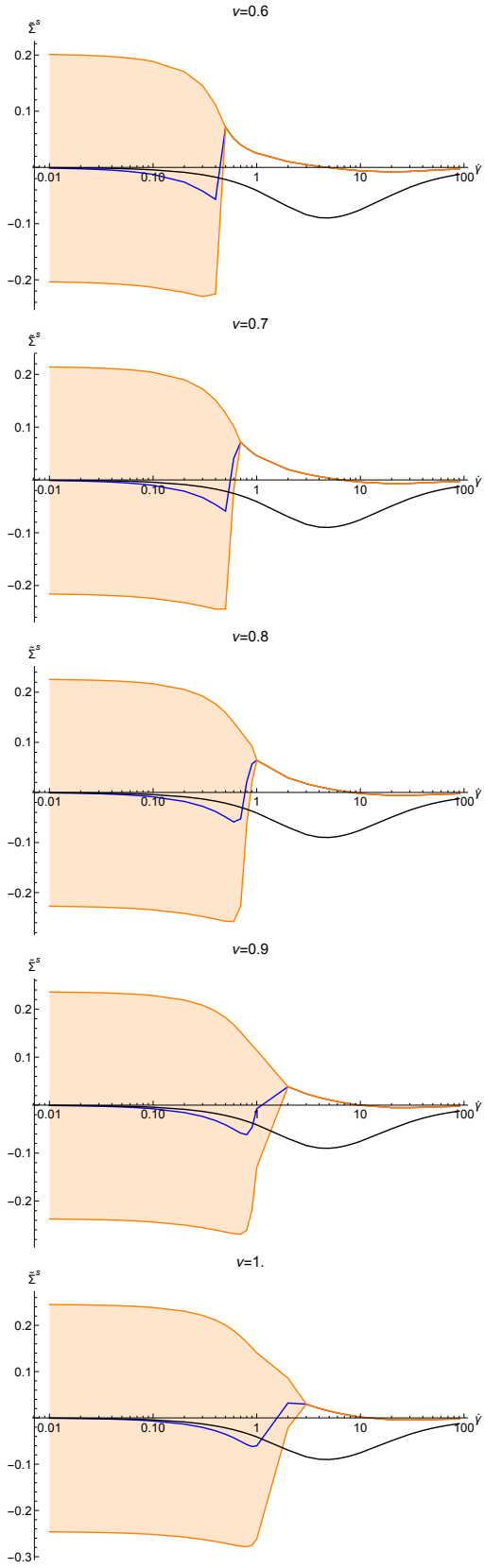

Figure 3.14: Continuation of fig. 3.13.

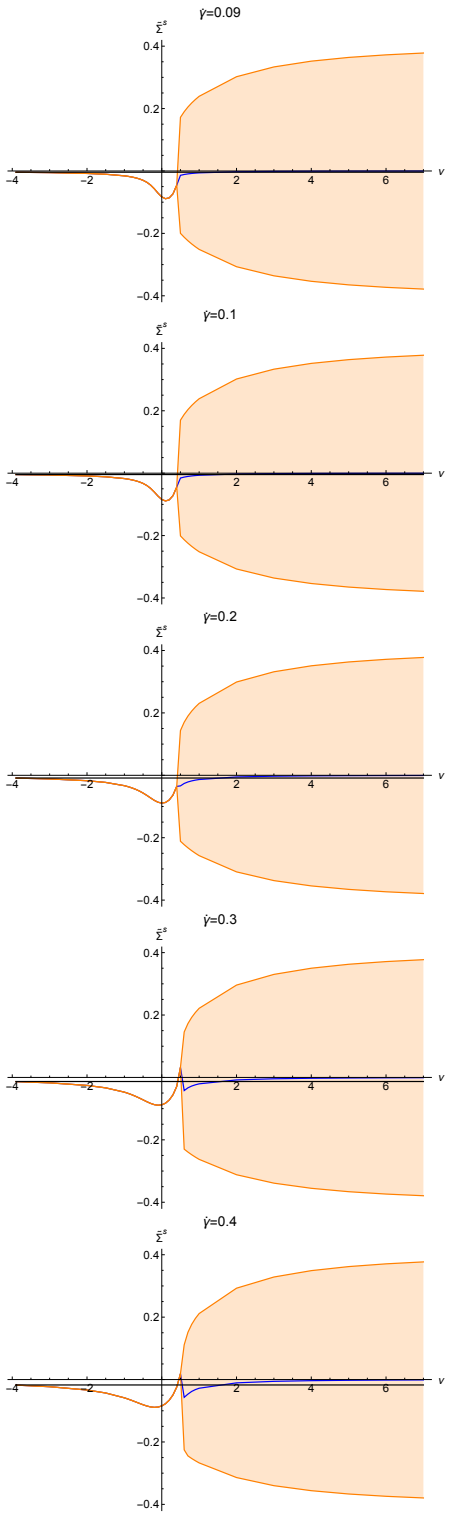

Figure 3.15: Dimensionless active shear stress $\tilde{\Sigma}^{\mathrm{s}}_{xy}$ as a function of ν for different shear rates (pushers with $\beta = 0.7$). The orange lines represent the maximum and minimum value for $\tilde{\Sigma}$, the blue line is the average between these two values, and the black line represents the ideal case.

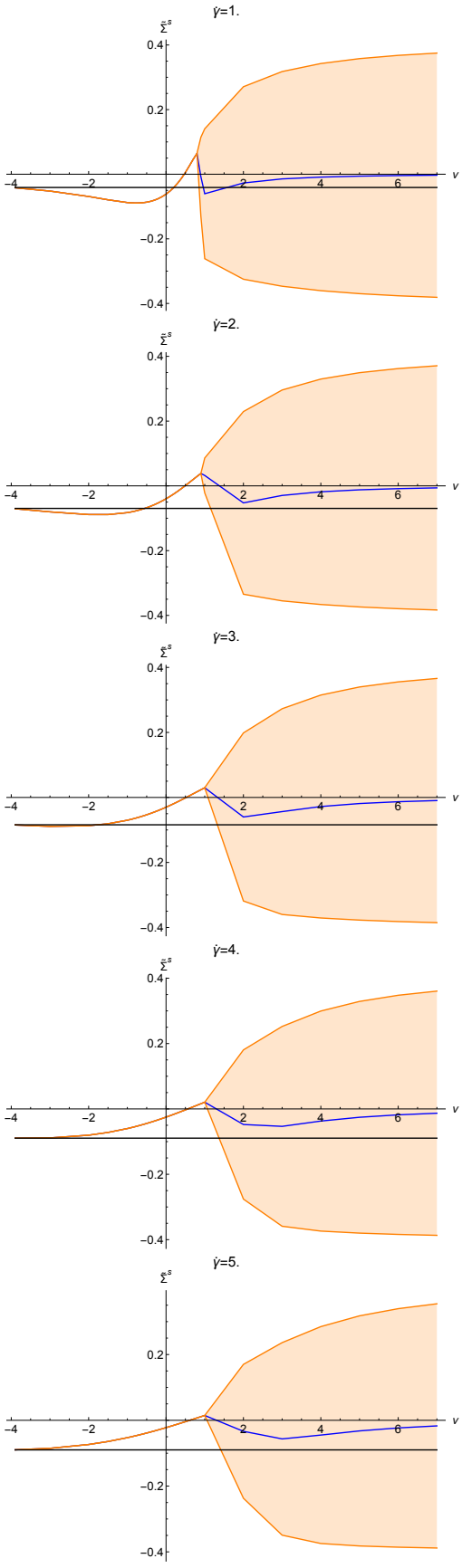

Figure 3.16: Continuation of fig. 3.15.

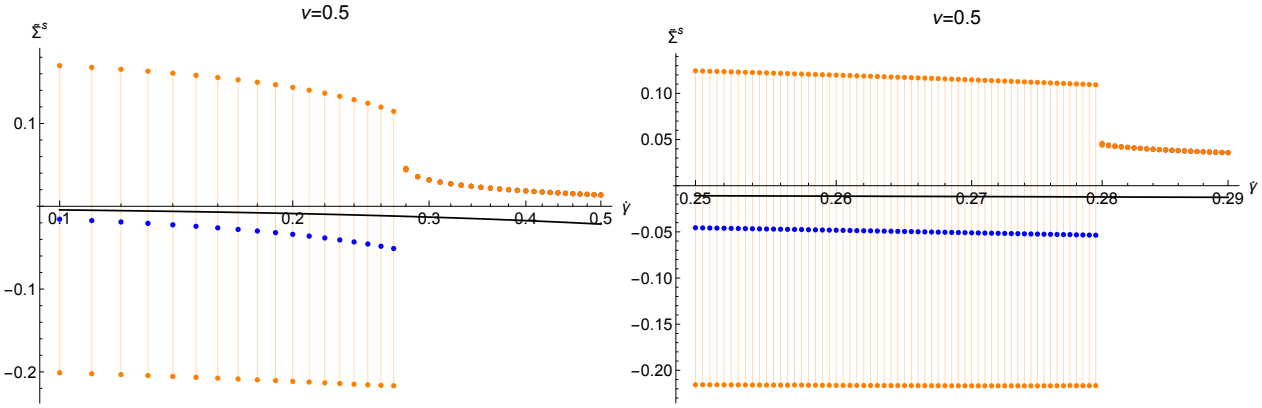

Figure 3.17: Dimensionless shear stress as a function of $\dot{\gamma}$ for $\nu = 0.5$. Pushers. $\beta = 0.7$. The orange dots represent the maximum and minimum values for $\tilde{\Sigma}$ and the blue dots are the average between these two values. The right plot is a zoom from the left one, which it is at the same time a zoom from the last plot of fig. 3.13.

Chapter 4

Rheology of Two-Dimensional Homogeneous Magnetotactic Suspensions

Summary

In this chapter we consider magnetotactic bacteria: bacteria that tend to align with external magnetic fields. We study the kinetic equation in two dimensions for a homogeneous suspension under a uniform shear flow, considering polar interactions for magnetic swimmers. In addition to the evolution of the orientation vector due to the local vorticity, the presence of an external magnetic field generates a torque which reorients the swimmer in the direction of the field or antiparallel to it. Numerical results show that the presence of a magnetic field shifts the transition points found in the non-magnetic case in chapter 3, depending on the relative orientation of the field with respect to the flow direction.

4.1 Introduction

Among all the different type of bacteria, a special group called magnetotactic has attracted important attention. They have the ability to synthesize an intern magnetic moment aligned with their principal axis $\boldsymbol{m} = \pm m\boldsymbol{p}$, strong enough to reorient them under an imposed magnetic field of the order of mili Teslas [7]. If the magnetic moment points in the swimming direction $\boldsymbol{p}$ then the bacterium is called *North Seeker* (NS), and *South Seeker* (SS) if it points in the opposite direction. Such magnetotactic bacteria are able to move preferentially to one of the magnetic poles [43] by following the magnetic field lines. In the north hemisphere, magnetotactic bacteria tend to move towards the north, following the positive sense of magnetic field lines (NS), whereas in the south hemisphere, they tend to follow the inverse sense, going to the south pole (SS). In both cases, they are led to deep waters, where the concentration of oxygen is low, representing the ideal environment for them to develop.

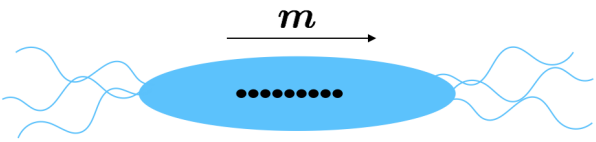

Figure 4.1: *Magnetospirilum gryphwaldense*. Simplified representation.

Magnetotactic bacteria exposed to a shear flow and a magnetic field exhibit unique patterns of collective motion such as band formation and pearling instabilities [47]. One example of magnetotactic bacteria is the *Magnetospirilum gryphwaldense* (NS), characterized by a spiral shape, flagella at both ends, and magnetic moment of $m \approx 10^{-16}\,\mathrm{Am}^2$ [31] [26] as shown in fig. 4.1.

If there is a magnetic field $\boldsymbol{B} = B\boldsymbol{b}$, the evolution of the orientation is going to be affected by the magnetic torque $\boldsymbol{m} \times \boldsymbol{B}$ [45]. Due to the small Reynolds' number, the condition of null total torque translates to an instantaneous rotation when applying a torque (in this case magnetic), and therefore we have an angular velocity proportional to this torque, $\boldsymbol{\Omega}_\mathrm{m} = \boldsymbol{m} \times \boldsymbol{B}/\xi_\mathrm{r}$, with ξ_r being the rotational friction coefficient, which modifies the Jeffery's equation (1.2)

$$\dot{\boldsymbol{p}} = (\mathbb{I} - \boldsymbol{pp}) \cdot (\beta\mathbb{E} + \mathbb{W}) \cdot \boldsymbol{p} + \boldsymbol{\Omega}_\mathrm{m} \times \boldsymbol{p}. \tag{4.1}$$

In what follows, we will focus on NS bacteria with the magnetic field in the plane oriented at an angle α from the flow direction $\hat{\boldsymbol{x}}$ (see fig. 4.2); the analysis for SS bacteria is completely analogous. For simplicity, we neglect the magnetic interaction among bacteria, since its effect is weak when dealing with dilute and semi-dilute suspensions. Indeed, the magnetic field produced by a magnetic dipole is $\boldsymbol{B}_\mathrm{dip} = \frac{\mu_0}{4\pi}\left(\frac{3\boldsymbol{r}(\boldsymbol{m}\cdot\boldsymbol{r})}{r^5} - \frac{\boldsymbol{m}}{3}\right)$, where $\mu_0 \approx 1.2 \times 10^{-6}\,\mathrm{Tm/A}$ and $\boldsymbol{r}$ is the distance from the dipole. We can roughly estimate the strength of this magnetic field: using the magnetic moment of *Magnetospirilum gryphwaldense* and a typical distance between bacteria of $r \approx \rho_c^{-1/3} \approx 12\,\mu\mathrm{m}$, we obtain $B_\mathrm{dip} \sim 10^{-34}\,\mathrm{T}$, whereas common experiments in the lab deal with $B \sim 10^{-3}\,\mathrm{T}$.

4.2 Polar Alignment

Performing the same Fourier decomposition in the kinetic equation (2.11) considering the collision factor given by (2.14), we have

$$\begin{aligned}\dot{a}_n = &- a_n\left(n^2 - \mathrm{i}n\dot{\gamma}/2 + \rho\right) - \mathrm{i}\dot{\gamma}\beta n/4\left(a_{n-2} + a_{n+2}\right) + \frac{\omega_\mathrm{m} n}{2}\left(\mathrm{e}^{-\mathrm{i}\alpha}a_{n-1} - a^{\mathrm{i}\alpha}a_{n+1}\right)\\ &+ 2\pi\sum_l a_l a_{n-l}\mathrm{sinc}\left(n\pi/2 - l\pi\right),\end{aligned} \tag{4.2}$$

where we used the rescaled variables given by (3.3), (3.4), and (3.5). $\omega_\mathrm{m}^{-1} = \xi_r/(mB)$ is the characteristic time for the magnetic moment $\boldsymbol{m}$ to relax towards the direction of the magnetic field $\boldsymbol{B}$.

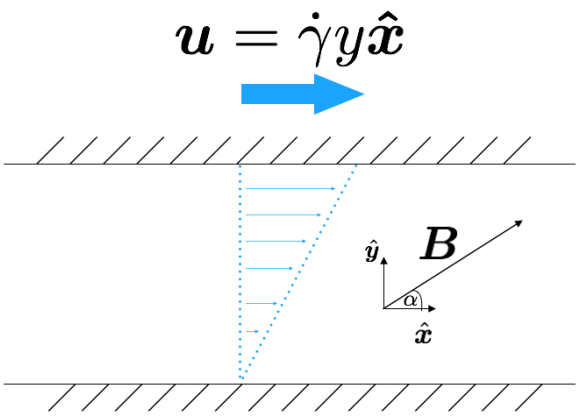

Figure 4.2: Uniform shear flow pointing in $\hat{\boldsymbol{x}}$ with gradient in $\hat{\boldsymbol{y}}$ and shear rate $\dot{\gamma}$. The magnetic field $\boldsymbol{B}$ is in the same plane x-y forming an angle α with $\hat{\boldsymbol{x}}$.

4.2.1 Numerical Results

By truncating eq. (4.2) up to $a_{\pm 5}$, we can obtain numerical results. In particular, we find that there is a competition between the alignment in the direction of the flow and the direction of the magnetic field, as shown in fig. 4.3. In this scenario there is a polar phase, however, the mean orientation tend to spend more time in the direction of the imposed magnetic field, which means that the mean orientation evolves having, on average, a non-zero magnitude, unlike the non-magnetic case. Moreover the external magnetic field shifts the critical concentration in a non-trivial way, and in fact, the order parameter is a function of the shear rate $\dot{\gamma}$, the concentration ρ, and the magnetic Peclet number ω_{m}.

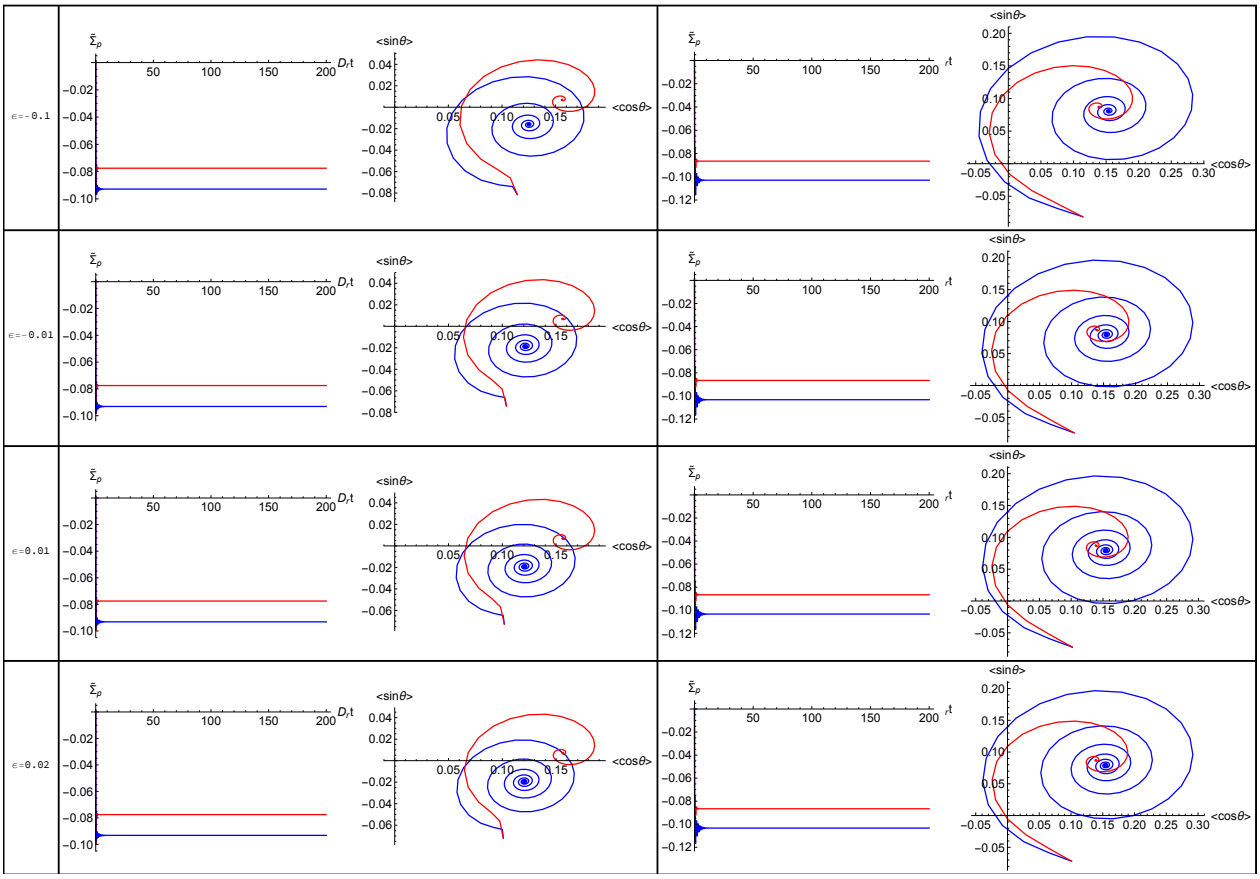

Figure 4.3: Dimensionless active shear stress $\tilde{\Sigma}^{\mathrm{s}}_{xy}$ as a function of time $D_{\mathrm{r}}t$ (left) and time evolution of the average orientation (right). The first column corresponds to $\omega_{\mathrm{m}} = 1$ and $\alpha = 45°$, and the second to $\omega_{\mathrm{m}} = 1$ and $\alpha = 135°$. Rows correspond to different densities. Red (blue) curves correspond to the ideal (interacting) case for pushers.

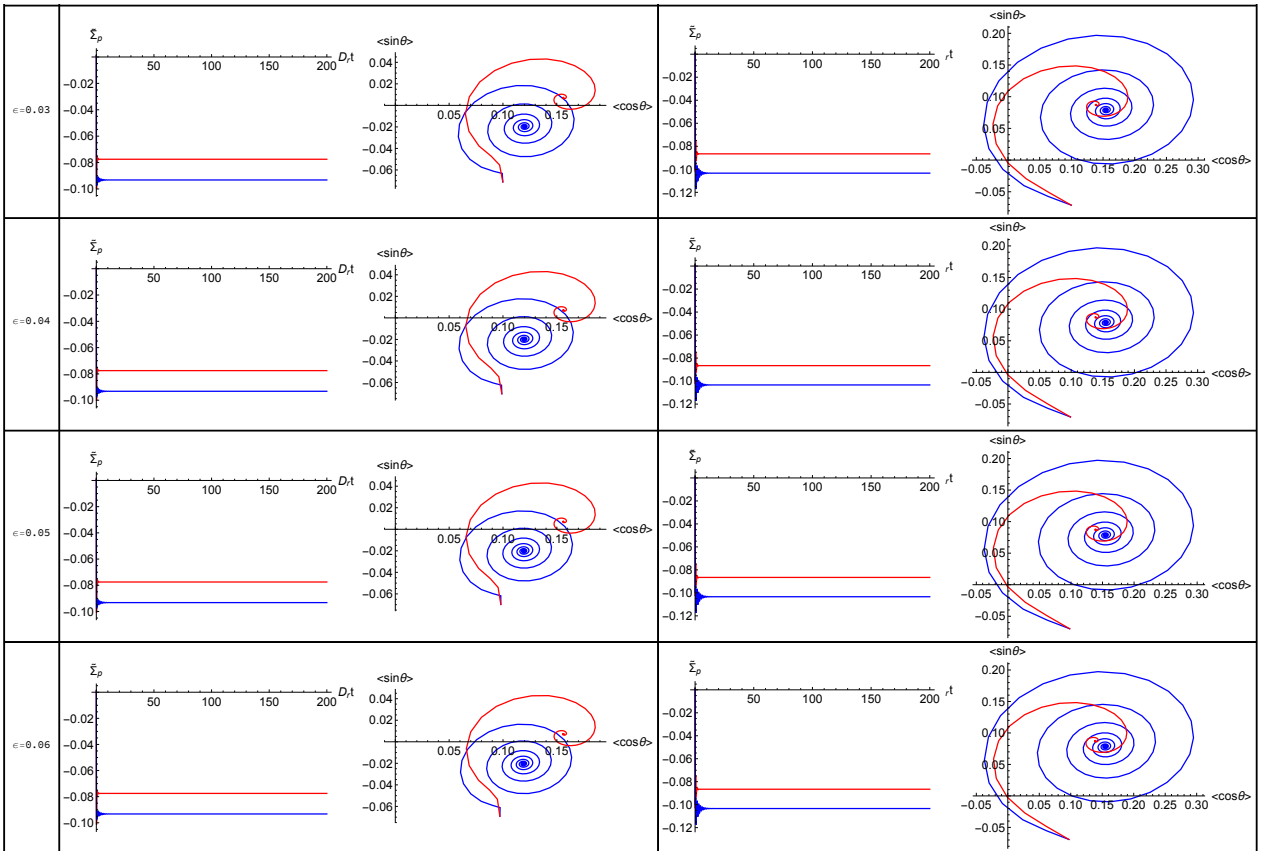

Figure 4.4: Continuation of fig. 4.3.

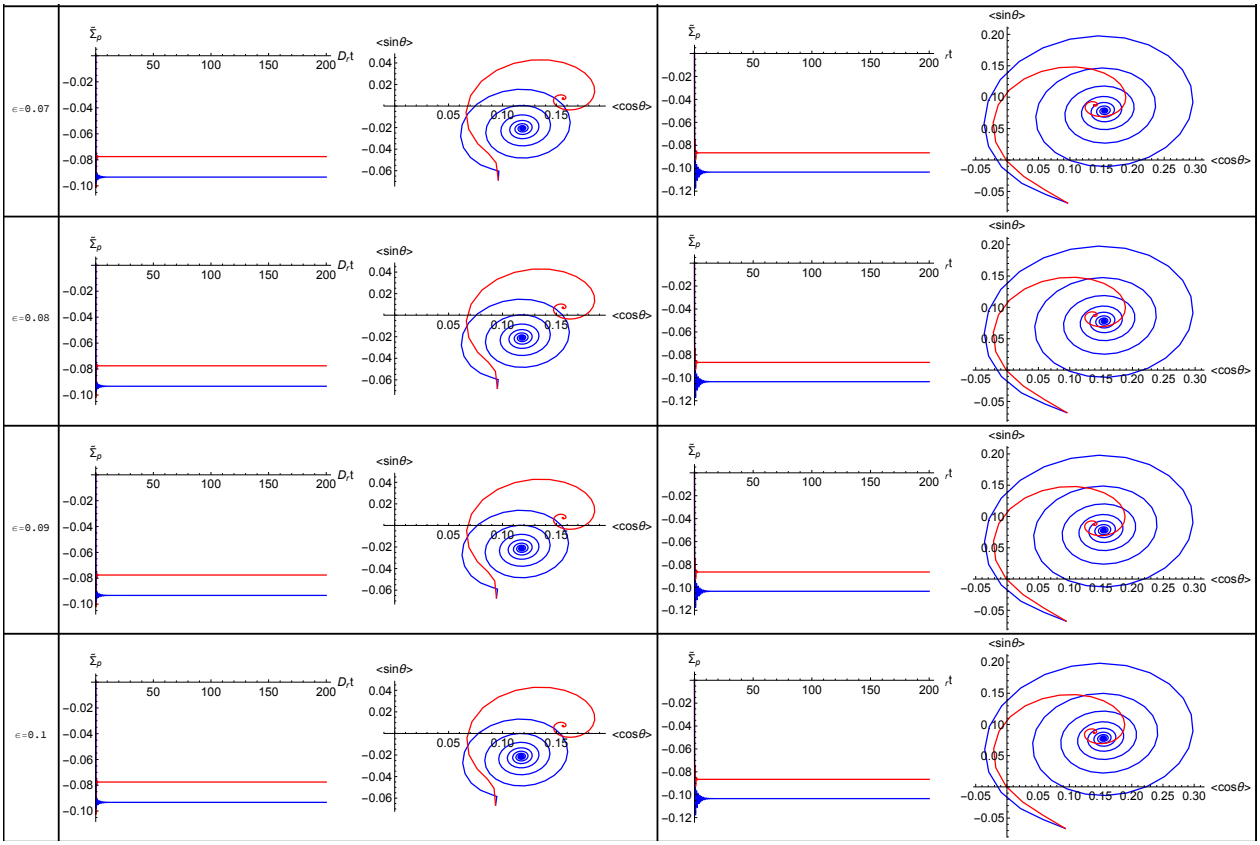

Figure 4.5: Continuation of fig. 4.3.

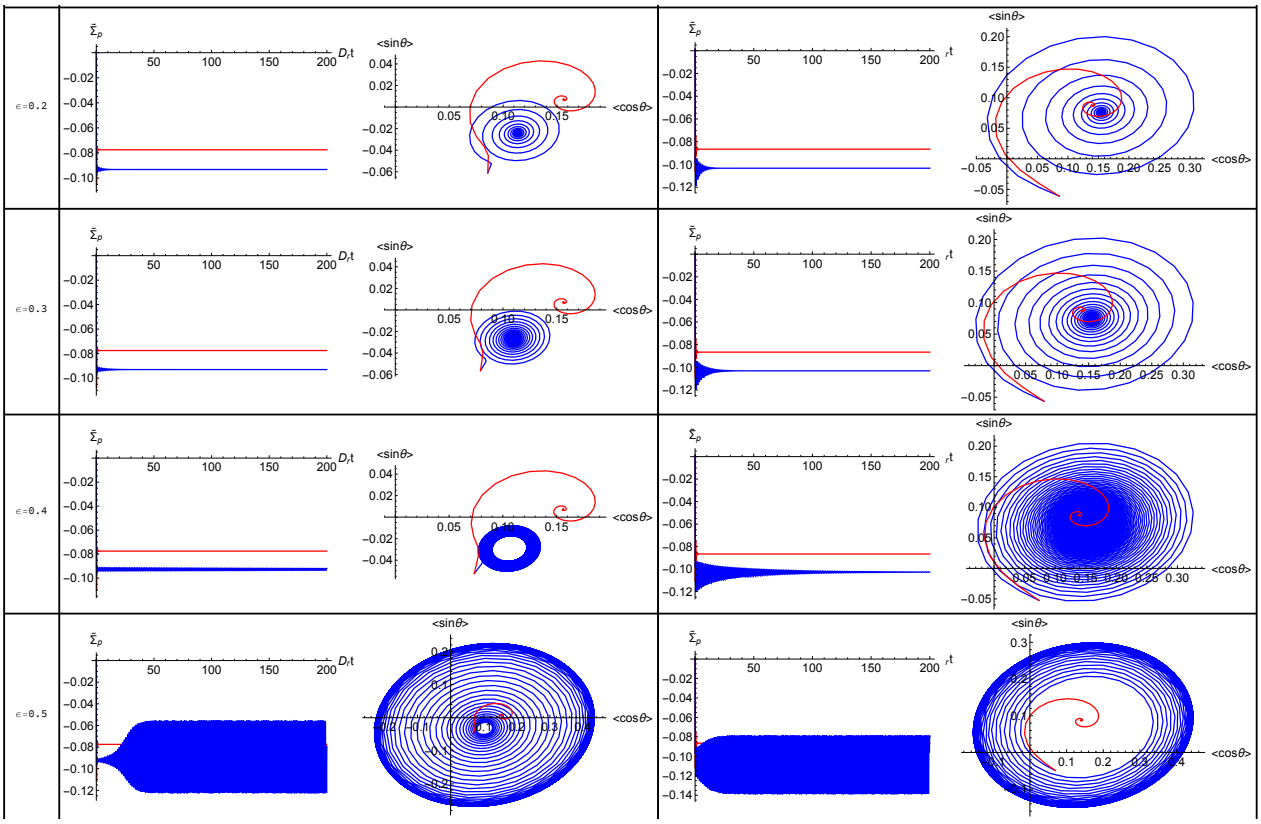

Figure 4.6: Continuation of fig. 4.3.

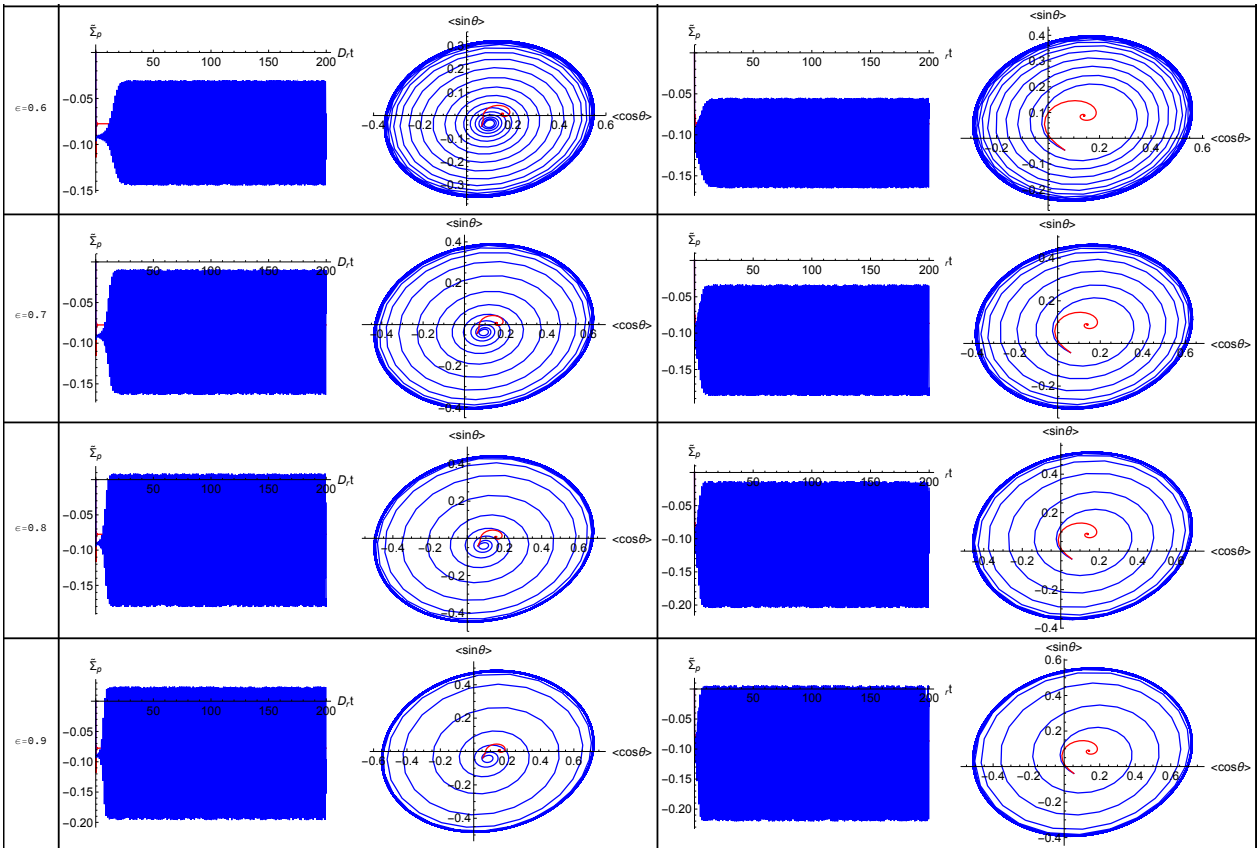

Figure 4.7: Continuation of fig. 4.3.

Chapter 5

Spatial Structures in Two- and Three-Dimensional Suspensions

Summary

In this chapter we study the kinetic equation in two and three dimensions for inhomogeneous suspensions under a shear flow, considering polar and nematic interactions. Different boundary conditions are explored, concluding that the only one capable of reproducing the homogeneous results are anti-specular BC with the walls. In particular, for the simulations we use wall-aligning collisions once the bacteria hit the wall. This adhoc condition reveals two phenomena observed experimentally: upstream swimming and high concentrations near the wall. Adding this boundary condition to two-dimensional systems, we found that an instability appears in the gradient direction for certain system sizes of pusher suspensions. Applying periodic-like BC leads to the same phenomenon, which allows us to use linear stability analysis, revealing that this instability is triggered by small wave-numbers, or equivalently, long-wavelengths. Therefore, if the system is small enough (smaller than the critical wave-length), then no instability appears. This peculiarity is also confirmed by the simulations. We also explore the three-dimensional case, in which a similar instability appears.

5.1 Introduction

In this section, we will include spatial dependence in the kinetic equation, which is the one presented in eq. (2.11)

$$\frac{\partial \Psi}{\partial t} + \frac{\partial (\dot{x}\Psi)}{\partial x} + \frac{\partial (\dot{y}\Psi)}{\partial y} + \frac{\partial (\dot{\theta}\Psi)}{\partial \theta} = D_r \frac{\partial^2 \Psi}{\partial \theta^2} + J[\Psi, \Psi]. \tag{5.1}$$

We will show that the validity of the homogeneous solutions is restricted to semi-dilute suspensions or very small systems, of the size of few mean free paths. Higher concentration

or bigger systems may give rise to spatial structures or instabilities.

First, we will analyze different bacteria-wall interacting mechanism in the dilute and semi-dilute regime. Then, we will introduce a particle-based method to study the kinetic equation. Finally, we will study the patterns that emerge from the unstable nature of the homogeneous solution.

5.2 Wall-Interactions

In this section we show how different bacteria-wall interacting mechanisms modify the distribution of swimmers. In particular, we study two mechanisms, that despite its simplicity, can shed some light on different phenomena. In order to facilitate the calculations and do not rely on numerical solutions from partial differential equations, we tackle the stationary dilute regime so the problem can be turned into determining eigenvalues and eigenvectors as shown below.

In the dilute regime, the stationary kinetic equation (2.11) reads

$$V_0 \sin\theta \frac{\partial \Psi}{\partial y} + \frac{\partial(\dot{\theta}\Psi)}{\partial \theta} = D_r \frac{\partial^2 \Psi}{\partial \theta^2}, \tag{5.2}$$

where we have neglected the spatial dependence in the flow direction on symmetry grounds, so $\Psi = \Psi(y, \theta)$. Using angular Fourier series, the equation for each amplitude a_n is

$$0 = -a_n \left(n^2 - \frac{\mathrm{i}n\dot{\gamma}}{2} \right) + \frac{\mathrm{i}}{2} \left(\frac{\mathrm{d}a_{n+1}}{\mathrm{d}y} - \frac{\mathrm{d}a_{n-1}}{\mathrm{d}y} \right) - \frac{\mathrm{i}\dot{\gamma}\beta n}{4} \left(a_{n-2} + a_{n+2} \right), \tag{5.3}$$

where we have used the rescaled variables given by (3.3), (3.4), and (3.5) plus $y \to y D_\mathrm{r}/V_0$. Equation (5.3) can be written in matrix form

$$\underbrace{\begin{pmatrix} \ddots & \ddots & \ddots & & & & \\ & -1 & 0 & 1 & & & \\ & & -1 & 0 & 1 & & \\ & & & -1 & 0 & 1 & \\ & & & & \ddots & \ddots & \ddots \end{pmatrix}}_{\mathbb{P}} \underbrace{\frac{\mathrm{d}}{\mathrm{d}y} \begin{pmatrix} \vdots \\ a_{-2} \\ a_{-1} \\ a_0 \\ a_1 \\ a_2 \\ \vdots \end{pmatrix}}_{\frac{\mathrm{d}\boldsymbol{a}}{\mathrm{d}y}} = \underbrace{\begin{pmatrix} \ddots & \ddots & \ddots & \ddots & & & \\ z_{-1} & 0 & w_{-1} & 0 & z_{-1} & & \\ & z_0 & 0 & w_0 & 0 & z_0 & \\ & & z_1 & 0 & w_1 & 0 & z_1 \\ & & & \ddots & \ddots & \ddots & \ddots \end{pmatrix}}_{\mathbb{M}} \underbrace{\begin{pmatrix} \vdots \\ a_{-2} \\ a_{-1} \\ a_0 \\ a_1 \\ a_2 \\ \vdots \end{pmatrix}}_{\boldsymbol{a}}, \tag{5.4}$$

with $w_n = -2\mathrm{i}n^2 - n\dot{\gamma}$ and $z_n = \dot{\gamma}\beta n/2$. This equation reduces to a generalized eigenvalue problem when introducing the ansatz $\boldsymbol{a} = \mathrm{e}^{\lambda y}\boldsymbol{A}$. Thus the solution can be expressed as

$$\boldsymbol{a} = \sum_j C_j \mathrm{e}^{\lambda_j y} \boldsymbol{A}, \tag{5.5}$$

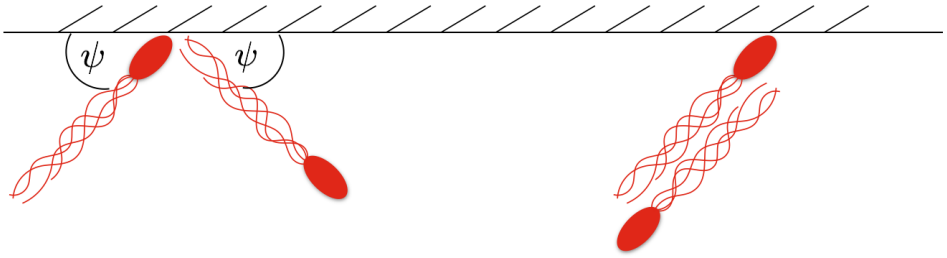

Figure 5.1: Specular (left) and anti-specular (right) boundary conditions depicted.

where C_j are constant coefficients given by the boundary conditions. In order to solve the eigenvalue problem (5.4) we must truncate the system up to an order $a_{\pm n}$ and then apply the standard tools, that is solving $\mathrm{Det}(\mathbb{P}\lambda - \mathbb{M}) = 0$ to determine the eigenvalues, and then determining the basis of the null space for each eigenvalue.

In what follows, we study two BC: specular and anti-specular collisions with the wall (see fig. 5.1).

5.2.1 Specular Collisions

In the upper wall, the specular collision translates to the following condition for the distribution function

$$\Psi(\theta) = \Psi(2\pi - \theta)_{0<\theta<\pi}. \tag{5.6}$$

The lower wall condition is completely analogous. In addition, we have the normalization condition

$$\int a_0 \mathrm{d}y = \frac{\rho}{2\pi}. \tag{5.7}$$

Expanding the condition (5.6) in Fourier series, we arrive, after some manipulation, at

$$(a_m - a_{-m})|_{\text{wall}} = 0 \qquad \forall m, \tag{5.8}$$

which is valid for the upper and lower wall.

Truncating the system (5.4) up to order $a_{\pm 4}$ and employing the specular boundary conditions, we obtain that the system indeed develops inhomogeneities near the walls, as shown in fig. 5.2. This result comes from the incompatibility of the BC with the Jeffery's equation (1.2), since the swimmer experiences an abrupt change in its angular speed when colliding with the wall.

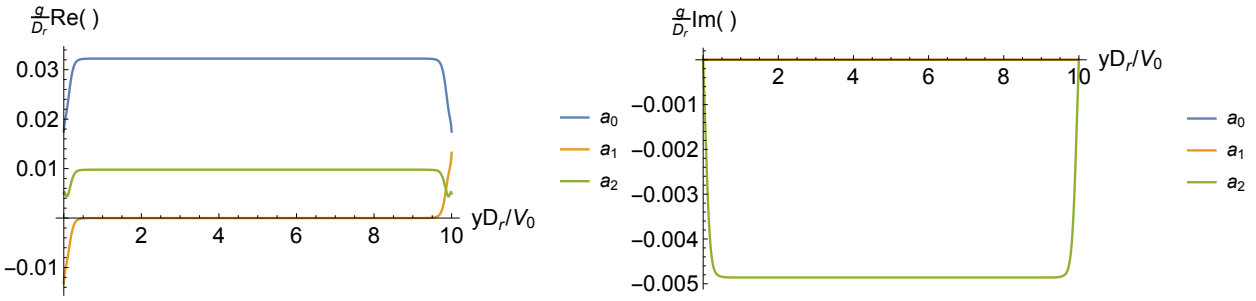

Figure 5.2: Real (left) and imaginary (right) part of a_0, a_1, and a_2 as a function of y, for $\dot{\gamma} = 10$, $\beta = 0.7$, $L_y = 10$, and $\rho = 2$, with specular BC. Numerical solution obtained by truncating eq. (5.4) up to order $a_{\pm 4}$.

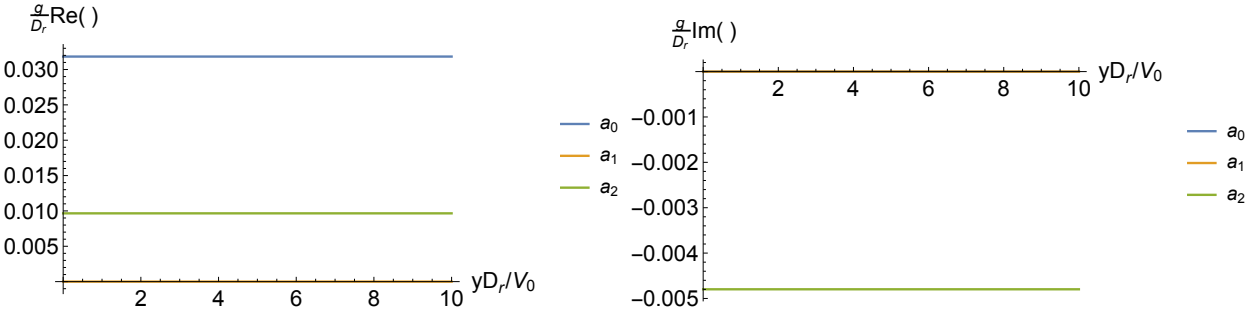

Figure 5.3: Real (left) and imaginary (right) part of a_0, a_1, and a_2 as a function of y, for $\dot{\gamma} = 10$, $\beta = 0.7$, $L_y = 10$, and $\rho = 2$ with anti-specular BC. Numerical solution obtained by truncating eq. (5.4) up to order $a_{\pm 4}$.

5.2.2 Anti-specular Collisions

For the anti-specular collisions in the upper wall, the constraint reads

$$\Psi(\theta) = \Psi(\pi - \theta)_{0<\theta<\pi}, \tag{5.9}$$

which translates to $a_m(y_{\text{wall}}) = 0$ for m odd when integrating from 0 to π. The same result applies to the lower wall. As before, we also have the normalization condition from eq. (5.7).

Truncating the system (5.4) up to order $a_{\pm 4}$ and employing the anti-specular boundary conditions, we obtain that the system reaches a homogeneous distribution as in the case of periodic boundary conditions (see fig. 5.3). Unlike the specular collisions, an anti-specular collision does not change the angular speed of the swimmer when colliding with the wall due to its ellipsoidal shape. This feature can be seen directly from the Jeffery's equation 2.12, which presents a symmetry in the even modes due to the presence of 2θ. However, this boundary condition in unreal and does not even approximate the interactions observed experimentally.

5.2.3 Wall-Aligning Collisions

It has been widely reported that bacteria are attracted to walls [6] yet the origin of this attraction is still discussed [21]. In this regard, two important macroscopic effects have

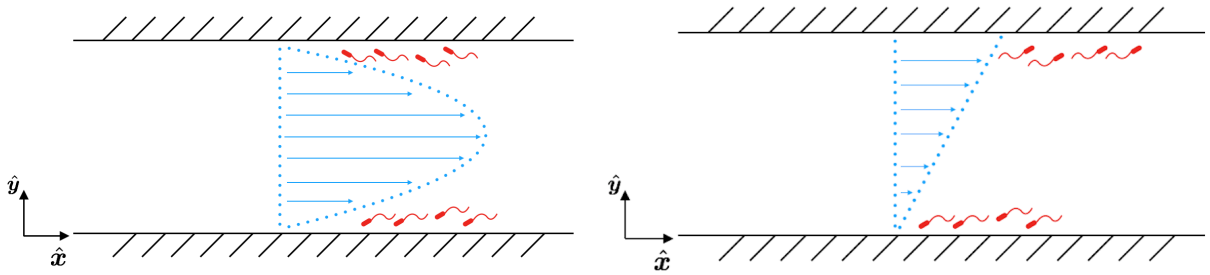

Figure 5.4: Representation of upstream swimming in a Poiseuille (left) and Couette (right) configuration.

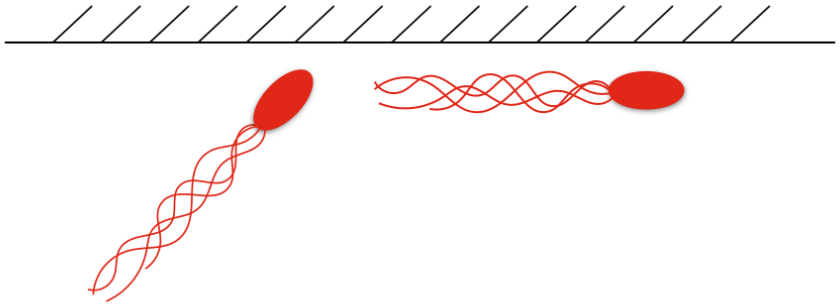

Figure 5.5: Alignment with wall boundary condition representation.

been observed experimentally: an augmentation in the concentration near the walls [6] and upstream swimming [17] [42], in which bacteria swim against the flow if $\boldsymbol{n} \cdot \nabla u > 0$, where $\boldsymbol{n}$ is the normal to the wall, and $\boldsymbol{u} = u(y)\hat{\boldsymbol{x}}$ (see fig. 5.4).

With this in mind, we employ an adhoc interaction: let $\boldsymbol{n}$ be the unit normal vector of a given surface. If $\boldsymbol{p}$ is the orientation of the swimmer when arriving to the surface, then it ends up with a new orientation $\boldsymbol{p}' = [\boldsymbol{p} - (\boldsymbol{p} \cdot \boldsymbol{n})\boldsymbol{n}]/[1 - (\boldsymbol{p} \cdot \boldsymbol{n})^2]$, which is a unit vector parallel to the surface (see fig. 5.5). Furthermore, in the simulations we add some noise to this reorientation process to render it more realistic, so at the end the swimmer is not completely aligned with the wall but has a small deviation from it.

The simulations reveal that this interaction leads to an augmentation of the bacteria concentration near the walls, as it would be expected since we are removing any velocity in the normal direction. Moreover, upstream swimming is obtained in 3 dimensions but not in 2 dimensions. The reason behind it is that in 3D bacteria have an extra degree of freedom that allow them to rotate around the gradient axis, whereas in 2D they are restricted to move in the plane and therefore cannot change their orientation smoothly.

5.3 Particle-based Methods

Particle-based methods are suitable tools to study kinetic equation. They are based on the fact that the distribution functions are statistical objects and therefore, they give averages of the real number of particles over small boxes in phase space and time (coarse-graining) [39].

We can simulate a large number of swimmers $\tilde{N}$ (which differs from the real number of swimmers N) with dynamics that reproduce the evolution of the distribution function and not necessarily the motion of real swimmers. Then, all the averages can be computed directly from the sampling swimmers. Each sampling swimmer represents $\Lambda = N/\tilde{N} = \rho L^3/\tilde{N}$ real swimmers. In what follows we will describe the evolution of each sampling swimmer.

Each simulation cycle consists of two steps: the displacement and the interactions. The displacement accounts for the streaming and the diffusion, whereas the interactions account for the binary collisions between bacteria.

5.3.1 Streaming Motion

Streaming motion is straightforward since we already have the expressions for $\dot{\boldsymbol{r}}$ and $\dot{\boldsymbol{p}}$, so we just have to solve the equations of motion for each sampling swimmer. If $\Gamma = \{\boldsymbol{r}, \boldsymbol{p}\}$ represents the degrees of freedom of the system, then the general equation of motion can be written as $\dot{\Gamma} = \phi(\Gamma)$. This equation can be easily integrated via Euler-like methods.

5.3.2 Diffusion

Diffusive behavior is obtained by adding a noise $\xi(t)$ to the previous equation of motion. This noise must have a Gaussian distribution with vanishing average, and must be uncorrelated, i.e.

$$\langle \xi(t)\xi(t') \rangle = \delta(t - t'), \tag{5.10}$$

so the equation of motion corresponds to a Langevin equation: $\dot{\Gamma} = \phi(\Gamma) + \sqrt{Dt}\xi(t)$.

Then, the evolution in a time step Δt becomes

$$\Gamma(t + \Delta t) = \Gamma(t) + \phi\left(\Gamma\right)\Delta t + \sqrt{2D\Delta t}\eta, \tag{5.11}$$

where η is a normal random number with a Gaussian distribution of unit variance and vanishing average.

In particular, for the case of rotational diffusion, we can adopt an alternative approach: let $\boldsymbol{\eta} = (\eta_x, \eta_y, \eta_z)$ be a noise-vector with each of its components having the properties mentioned before. Then the diffusive behavior can be accounted by including a multiplicative noise to the equation of motion

$$\boldsymbol{p}(t + \Delta t) = \boldsymbol{p}(t) + \phi(\boldsymbol{r}, \boldsymbol{p})\Delta t + \sqrt{2D_r\Delta t}\boldsymbol{p} \times \boldsymbol{\eta}. \tag{5.12}$$

In order to assure that $\boldsymbol{p}$ is a unit vector, it is mandatory to normalize $\boldsymbol{p}$ after each time step.

5.3.3 Collisions

Here is where we depart from Molecular Dynamics (MD). Although we could simulate each real collision, implementing them would be very costly. The general technique to deal with two-particle collision is the direct simulation Monte Carlo (DSMC), which samples the collisions statistically.

DSMC requires a grid with each cell size Δ being large enough to avoid MD, and small enough to avoid the loss of any relevant information (see fig. 5.6). In this regard, we have to consider two length scales: the mean free path $l_{\mathrm{mfp}} \sim 1/(\rho\sigma)$ and the Jeffery's orbit length $L_{\mathrm{J}} \sim V_0/\dot{\gamma}$ (applicable for uniform shear flows with shear rate $\dot{\gamma}$). We must have $\Delta < L_J$ so we do not lose information about the spatial organization. Finally, Δ must not be greater than a few mean free paths l_{mfp} so we can choose the pair of swimmers randomly in the box assuming a nearly homogeneous system. Then the hierarchy should be $\Delta \sim l_{\mathrm{mfp}} < L_J$.

The local distribution $\Psi(\boldsymbol{r}, \boldsymbol{p})$ is sampled by the number of local (sampling) swimmers, which we call $\tilde{N}_{\mathrm{i},j,k}$ with i, j, k indicating the box. The total number of collisions that should take place for the sampling particles, in a time step Δt is $N^{\mathrm{coll}}_{\mathrm{i},j,k} = \tilde{N}_{\mathrm{i},j,k}\nu_{\mathrm{i},j,k}\Delta t/2$, where $\nu_{\mathrm{i},j,k}$ is the collision frequency at the given box, and the factor $1/2$ avoids double counting. The collision frequency, in the Maxwell approximation, is given by

$$\nu(\boldsymbol{r}) = \frac{g}{\rho(\boldsymbol{r})}\int \Psi(\boldsymbol{p}_1)\Psi(\boldsymbol{p}_2)\mathrm{d}\boldsymbol{p}_1\mathrm{d}\boldsymbol{p}_2 = g\rho(\boldsymbol{r}), \tag{5.13}$$

so the number of collisions in a box is

$$N^{\mathrm{coll}}_{\mathrm{i},j,k} = \frac{\tilde{N}^2_{\mathrm{i},j,k}\Lambda(D_r\Delta t)}{2}\frac{g}{D_r\Delta^3}, \tag{5.14}$$

To perform the collisions, in each box we choose $N^{\mathrm{coll}}_{\mathrm{i},j,k}$ pairs of random sampling swimmers and we update their orientations according to the completely inelastic polar or nematic collision rules. This simple approach is valid due to the Maxwell approximation. If we were to consider the cross-section depending on the incidental angles of the swimmers, then the collision process is slightly more sophisticated [39].

One important remark is that $N^{\mathrm{coll}}_{\mathrm{i},j,k}$ is not necessarily an integer number. By truncating it we would be considering fewer collisions than expected, affecting the transport properties of the system. In order to avoid such undesired side-effects, it is a common practice to truncate $N^{\mathrm{coll}}_{\mathrm{i},j,k}$ to an integer number and to add the fractional part to the next time step collision process, so the right number of collisions is generated on average.

5.4 Two-Dimensional Simulations

We perform different simulations by varying the number density, the shear rate, and the dimensions of the system. We first consider the wall-aligning BC since it is more realistic.

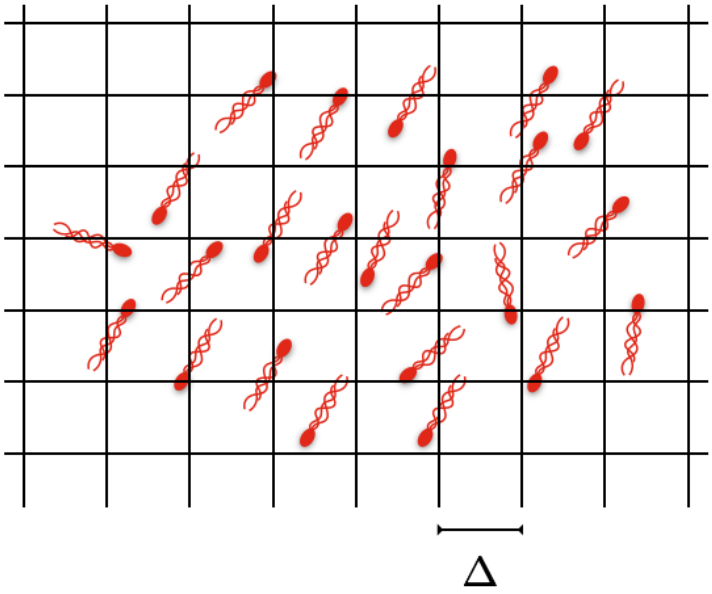

Figure 5.6: Grid DSMC in two dimensions. The length cell Δ is depicted.

We found that for large systems, or equivalently small shear rates, spatial structures emerge in the $\hat{\boldsymbol{y}}$ direction but not in the direction of the flow. Additionally, simulations suggest that they are not formed by nucleation processes [4]. In figs. 5.7, 5.8, and 5.9 we show the number density integrated in $\hat{\boldsymbol{x}}$ direction, $\rho_x(y)$, and the average orientation weighted by the density $\langle \boldsymbol{p} \rangle_x \rho_x$ (averaged in the $\hat{\boldsymbol{x}}$ direction) as a function of y and time, in a spatiotemporal diagram. We observe that, due to the instability of the homogeneous suspensions in the gradient direction, spatial structures emerge. On the contrary, as illustrated in figs. 5.10, 5.11, and 5.12, where we show the number density integrated in the $\hat{\boldsymbol{y}}$ direction, $\rho_y(x)$ and the average orientation weighted by the density $\langle \boldsymbol{p} \rangle_y \rho_y$ (this time averaged in the $\hat{\boldsymbol{y}}$ direction) as a function of x and time, in a spatiotemporal diagram, we observe that this direction does not present any instability.

The BC lead to inhomogeneities (sec. 5.2) in the $\hat{\boldsymbol{y}}$ direction, so in order to determine if the spatial structures are dependent on the wall interactions, we employ periodic-like boundary conditions. Although the uniform shear flow is only periodic in the direction of the flow, we can use periodic-like boundary condition in all directions by applying the Lees-Edwards method [22]. This method is widely used to compute transport properties, such as the viscosity of liquids and granular flows, with high accuracy [22]. In our case, this method simply consists in shifting the position of the swimmer by $\pm\dot{\gamma} L_y \Delta T$ every time it crosses the non-periodic boundary (see fig. 5.13), where L_y is the height of the system and ΔT the time elapsed from the beginning of the simulation. Notice that if the system is homogeneous in the x direction, then this BC is irrelevant.

By using the Lees-Edwards BC together with the same system parameters, we found the same spatial structures (see figs. 5.14 5.15 5.16 5.17 5.18 5.19), concluding that they are not caused by the walls.

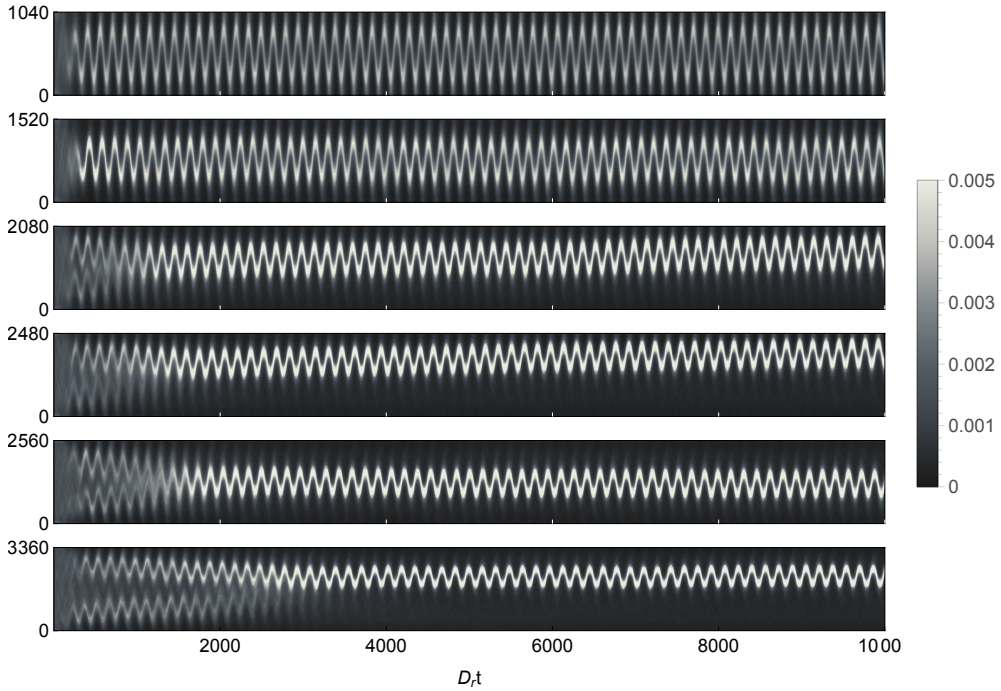

Figure 5.7: $\rho_x(y)$ (gray scale) in time (horizontal axis) space (vertical axis, in µm) representation obtained from DSMC simulations, for different L_y and fixed $L_x = 160\,\mu\text{m}$. $\rho = 10$, $\dot{\gamma} = 10$, and $\beta = 0.7$. Wall-aligning boundary condition were applied.

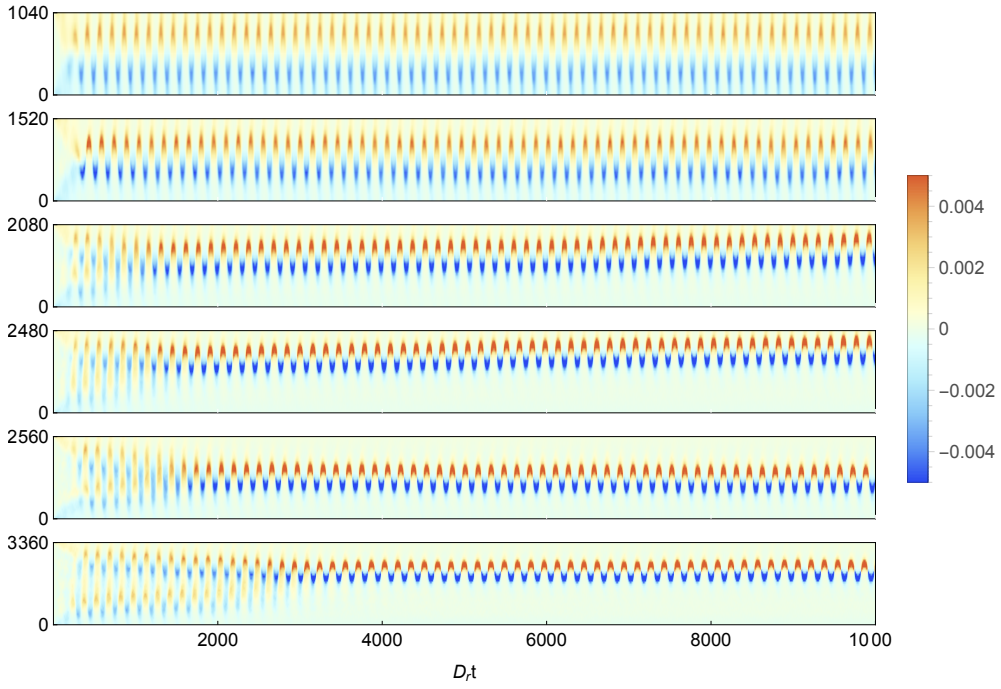

Figure 5.8: $\langle p_x \rangle_x \rho_x(y)$ (color bar) in time (horizontal axis) space (vertical axis, in µm) representation obtained from DSMC simulations, for different L_y and fixed $L_x = 160\,\mu\text{m}$. $\rho = 10$, $\dot{\gamma} = 10$, and $\beta = 0.7$. Wall-aligning boundary condition were applied.

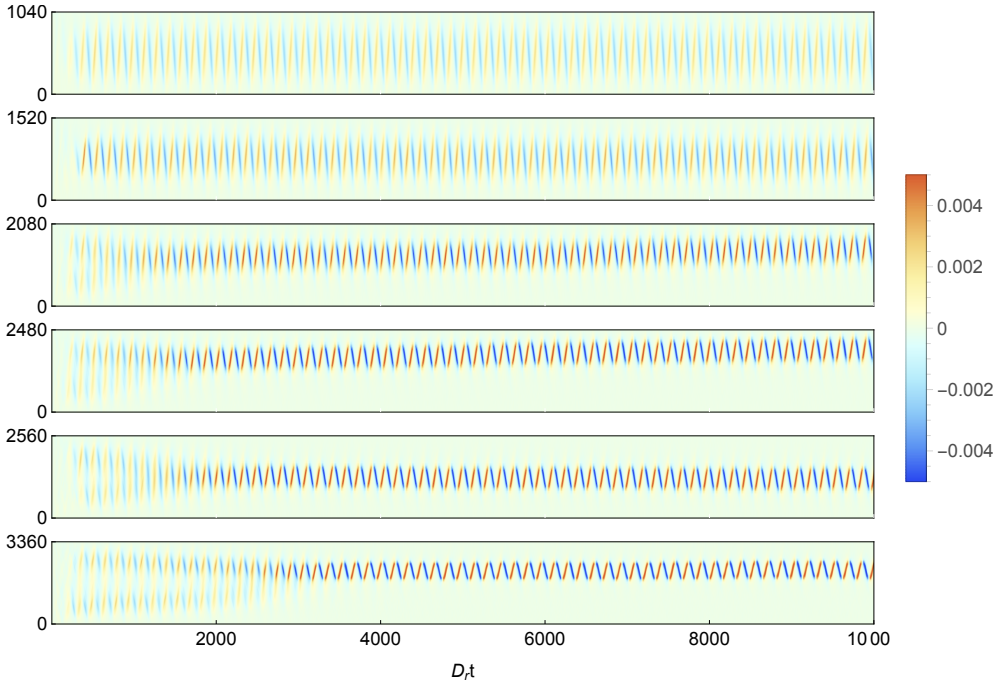

Figure 5.9: $\langle p_y \rangle_x \rho_x(y)$ (color bar) in time (horizontal axis) space (vertical axis, in µm)) representation obtained from DSMC simulations, for different L_y and fixed $L_x = 160\,\mu\text{m}$. $\rho = 10$, $\dot{\gamma} = 10$, and $\beta = 0.7$. Wall-aligning boundary condition were applied.

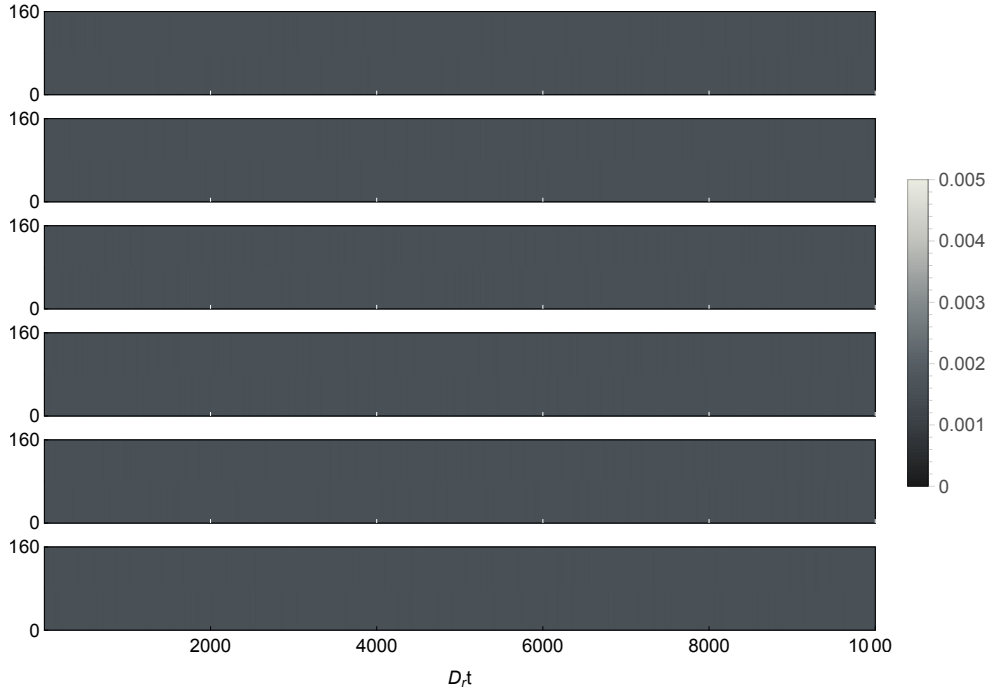

Figure 5.10: $\rho_y(x)$ (gray scale) in time (horizontal axis) space (vertical axis, in µm) representation obtained from DSMC simulations, for different L_y and fixed $L_x = 160\,\mu\text{m}$. $\rho = 10$, $\dot{\gamma} = 10$, and $\beta = 0.7$. Wall-aligning boundary condition were applied.

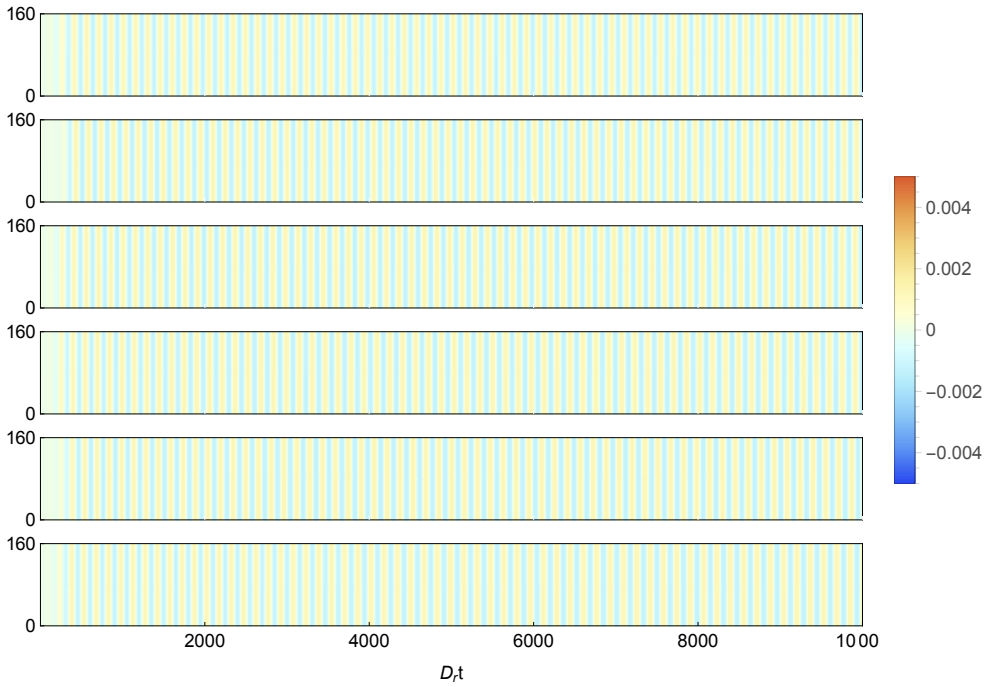

Figure 5.11: $\langle p_x \rangle_y \, \rho_y(x)$ (color bar) in time (horizontal axis) space (vertical axis, in µm) representation obtained from DSMC simulations, for different L_y and fixed $L_x = 160\,\mu\text{m}$. $\rho = 10$, $\dot{\gamma} = 10$, and $\beta = 0.7$. Wall-aligning boundary condition were applied.

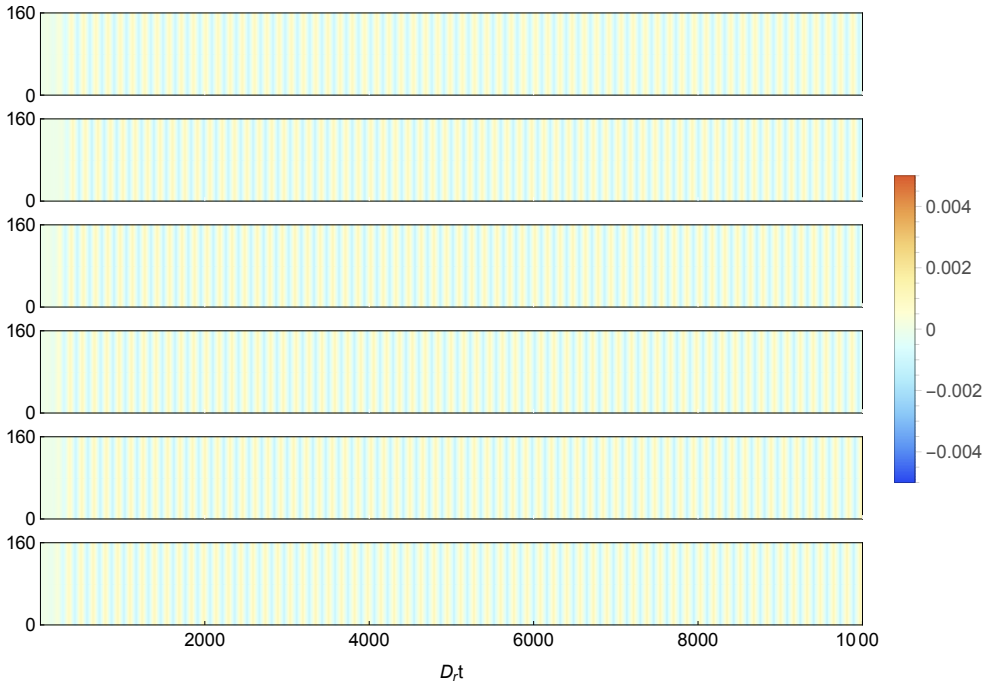

Figure 5.12: $\langle p_y \rangle_y \, \rho_y(x)$ (color bar) in time (horizontal axis) space (vertical axis, in µm) representation obtained from DSMC simulations, for different L_y and fixed $L_x = 160\,\mu\text{m}$. $\rho = 10$, $\dot{\gamma} = 10$, and $\beta = 0.7$. Wall-aligning boundary condition were applied.

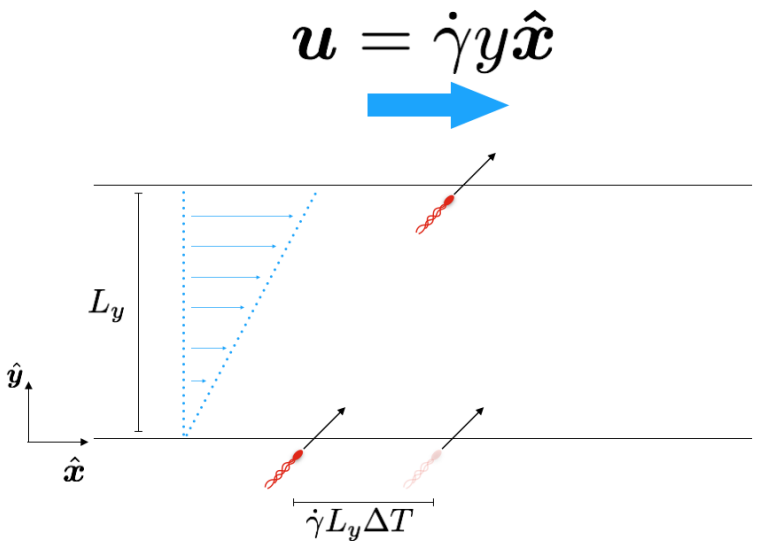

Figure 5.13: Lees-Edwards boundary condition scheme. If the swimmer traverses the wall, then it appears in the opposite wall with its x position shifted by $\dot{\gamma} L_y \Delta T$, where $\dot{\gamma}$ is the shear rate of the uniform flow, L_y the distance between the walls, and ΔT the time elapsed from the beginning of the simulation.

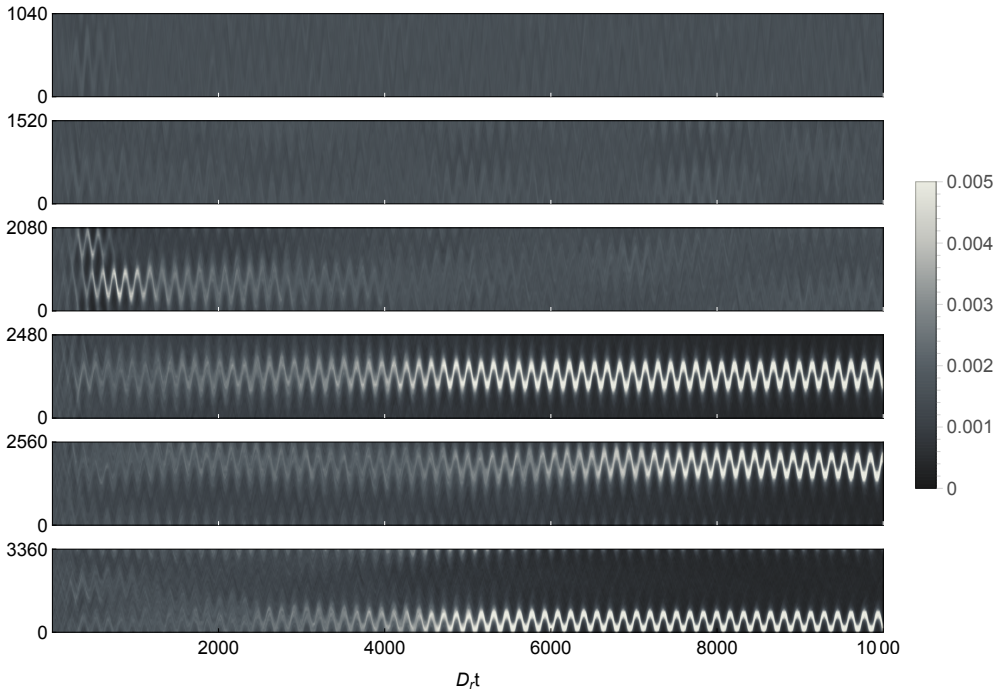

Figure 5.14: $\rho_x(y)$ (gray scale) in time (horizontal axis) space (vertical axis, in µm) representation obtained from DSMC simulations, for different L_y and fixed $L_x = 160\,\mu\text{m}$. $\rho = 10$, $\dot{\gamma} = 10$, and $\beta = 0.7$. Lees-Edward boundary condition were applied.

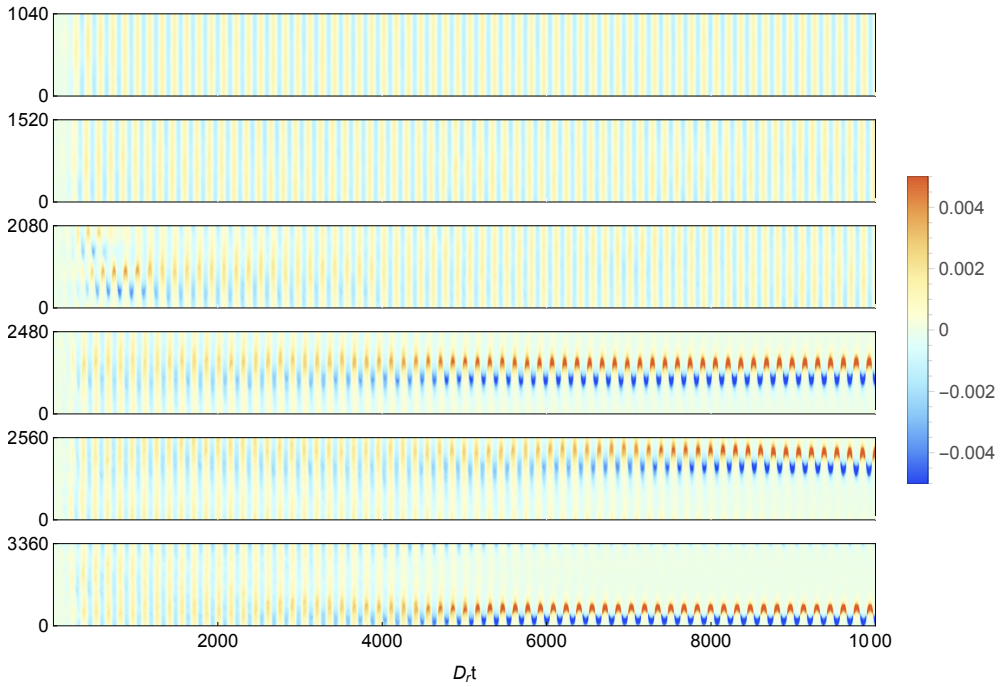

Figure 5.15: $\langle p_x \rangle_x \rho_x(y)$ (color bar) in time (horizontal axis) space (vertical axis, in µm) representation obtained from DSMC simulations, for different L_y and fixed $L_x = 160\,\mu\text{m}$. $\rho = 10$, $\dot{\gamma} = 10$, and $\beta = 0.7$. Lees-Edward boundary condition were applied.

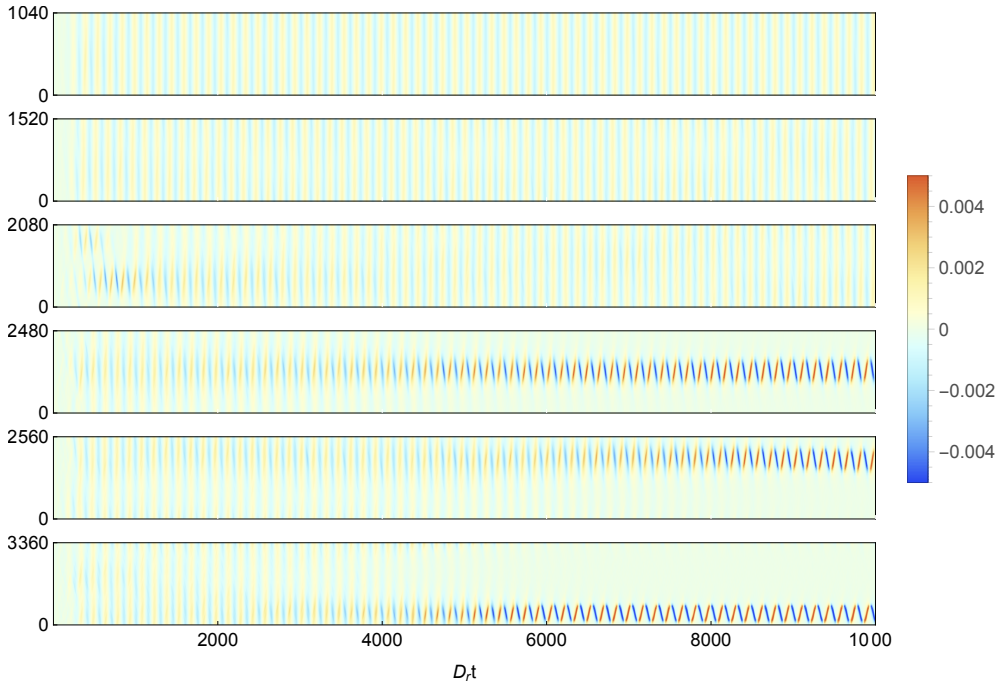

Figure 5.16: $\langle p_y \rangle_x \rho_x(y)$ (color bar) in time (horizontal axis) space (vertical axis, in µm) representation obtained from DSMC simulations, for different L_y and fixed $L_x = 160\,\mu\text{m}$. $\rho = 10$, $\dot{\gamma} = 10$, and $\beta = 0.7$. Lees-Edward boundary condition were applied.

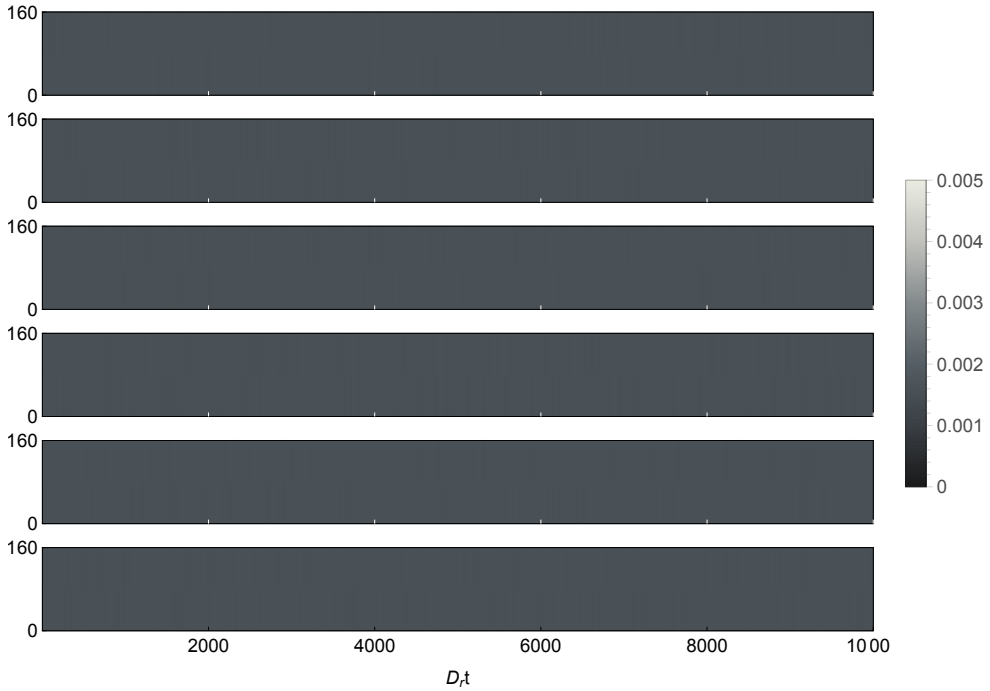

Figure 5.17: $\rho_y(x)$ (gray scale) in time (horizontal axis) space (vertical axis, in µm) representation obtained from DSMC simulations, for different L_y and fixed $L_x = 160\,\mu\text{m}$. $\rho = 10$, $\dot{\gamma} = 10$, and $\beta = 0.7$. Lees-Edward boundary condition were applied.

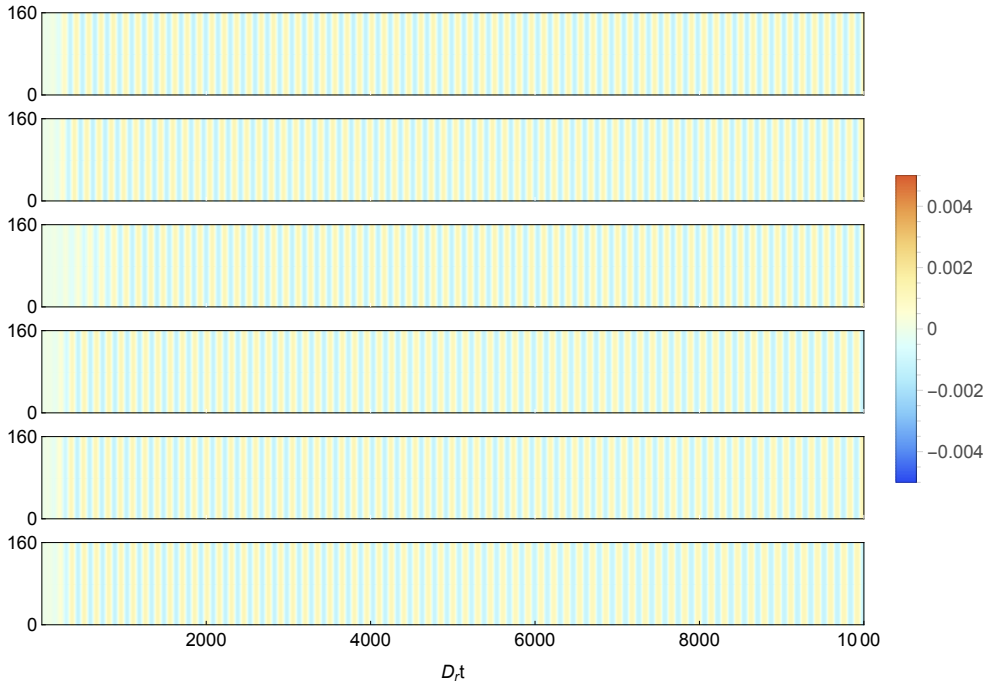

Figure 5.18: $\langle p_x \rangle_y \rho_y(x)$ (color bar) in time (horizontal axis) space (vertical axis, in µm) representation obtained from DSMC simulations, for different L_y and fixed $L_x = 160\,\mu\text{m}$. $\rho = 10$, $\dot{\gamma} = 10$, and $\beta = 0.7$. Lees-Edward boundary condition were applied.

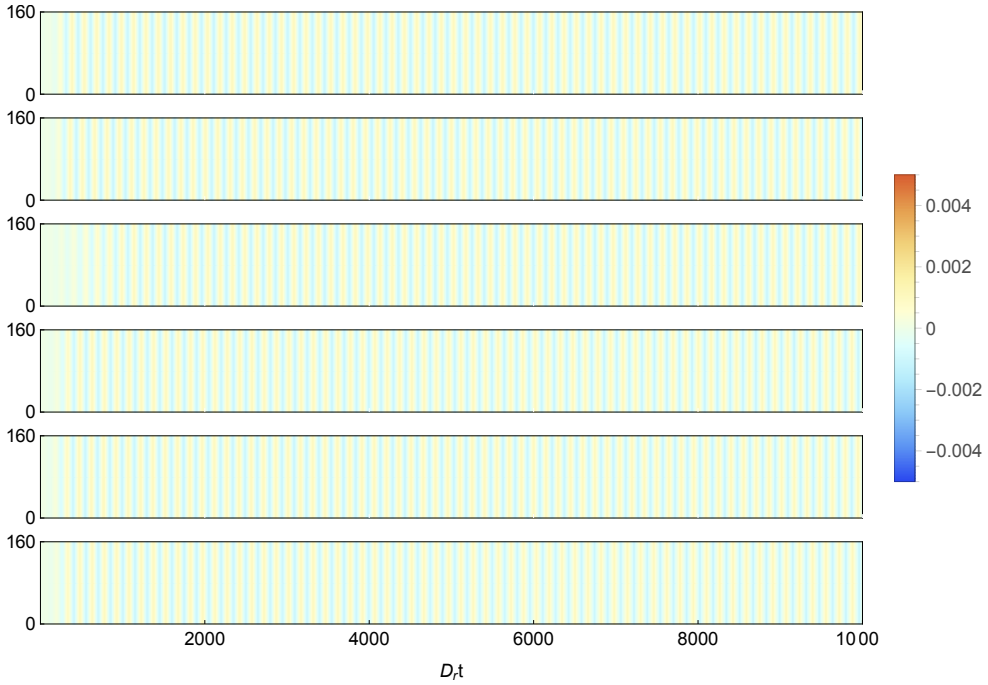

Figure 5.19: $\langle p_y \rangle_y \rho_y(x)$ (color bar) in time (horizontal axis) space (vertical axis, in µm) representation obtained from DSMC simulations, for different L_y and fixed $L_x = 160\,\mu\text{m}$. $\rho = 10$, $\dot{\gamma} = 10$, and $\beta = 0.7$. Lees-Edward boundary condition were applied.

It is worth pointing out that larger systems or, analogously, larger shear rates, allow the formation of several bands that show fusion processes in a slow time-scale, as shown in fig. 5.20.

Having the same phenomenon in the periodic system and the one including walls, we can turn our attention to the former case and perform a linear stability analysis of the homogeneous solution Ψ_0. Let $\Psi = \Psi_0 + \alpha\Psi_1$ with $\alpha \ll 1$. To first order in α, eq. (2.11) reads

$$\frac{\partial \Psi_1}{\partial t} = -(\boldsymbol{p} + \dot{\gamma} y \hat{x}) \cdot \nabla \Psi_1 - \frac{\partial(\dot{\theta}\Psi_1)}{\partial \theta} + \frac{\partial^2 \Psi_1}{\partial \theta^2} + I\left[\Psi_0, \Psi_1\right], \tag{5.15}$$

where $I[\Psi_0, \Psi_1]$ is the linearized Boltzmann operator, given by

$$\begin{aligned} I[\Psi_0, \Psi_1] = \int_{-\pi}^{\pi} \mathrm{d}w [&\Psi_0(\theta + w/2)\Psi_1(\theta - w/2) + \Psi_1(\theta + w/2)\Psi_0(\theta - w/2) - \Psi_0(\theta)\Psi_1(\theta - w) \\ &- \Psi_1(\theta)\Psi_0(\theta - w)]. \end{aligned} \tag{5.16}$$

In order to analyze the stability of the homogeneous solution, we assume plane-wave perturbations. Considering the deformation and advection fo the waves due to the imposed flow, we write the perturbation as [27]

$$\Psi_1(\boldsymbol{r}, \theta, t) = \bar{\Psi}_1(\theta, t) \mathrm{e}^{\mathrm{i}\boldsymbol{k}\cdot(\boldsymbol{r} - \dot{\gamma} y \hat{x} t)}. \tag{5.17}$$

The advantage of this kind of perturbation is that it eliminates the explicit appearance y (see eq. 5.15), which if treated with Fourier, would be expressed as convolutions, rendering

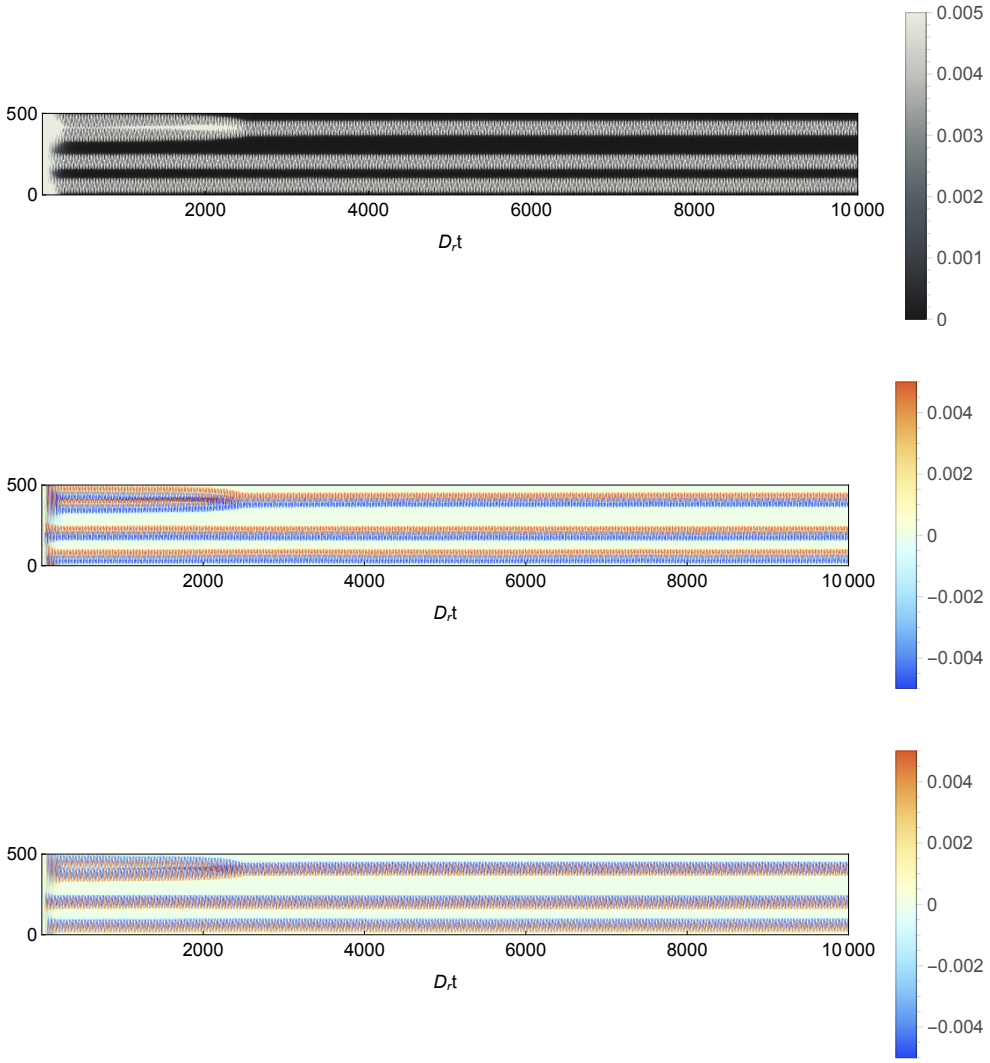

Figure 5.20: $\rho_x(y)$ (top, in gray scale), $\langle p_x \rangle_x \rho_x(y)$ (middle, in color bar), $\langle p_y \rangle_x \rho_x(y)$ (bottom, in color bar), in time (horizontal axis) space (vertical axis, in µm) representation obtained from DSMC simulations, for $L_y = L_x = 500\,\mu\text{m}$. $\rho = 50$, $\dot{\gamma} = 100$, and $\beta = 0.7$. Lees-Edward boundary condition were applied. At $D_r t \approx 2400$ there is a fusion event between two bands.

the problem more complicated. The price to pay is the explicit appearance of time in the perturbation equation.

Inserting (5.17) into (5.17) we are left with

$$\frac{\partial\bar{\Psi}_1}{\partial t} = -\mathrm{i}\boldsymbol{p}\cdot\boldsymbol{k}\bar{\Psi}_1 + \mathrm{i}\dot{\gamma}k_x t\sin\theta\bar{\Psi}_1 - \frac{\partial(\dot{\theta}\bar{\Psi}_1)}{\partial\theta} + \frac{\partial^2\bar{\Psi}_1}{\partial\theta^2} + I\left[\Psi_0, \bar{\Psi}_1\right]. \tag{5.18}$$

Notice that (5.18) is not an eigenvalue problem due to the explicit appearance of t in the RHS, in addition to the explicit time-dependence of the homogeneous solutions, which can be seen through the ansatz in eqs. (3.19) and (3.20). Expanding the perturbation in angular Fourier series, $\bar{\Psi}_1 = \sum b_n(t)\mathrm{e}^{\mathrm{i}n\theta}$, eq. (5.18) can be written as

$$\frac{\mathrm{d}\boldsymbol{b}}{\mathrm{d}t} = \mathbb{L}(\boldsymbol{k}, t)\boldsymbol{b}, \tag{5.19}$$

where

$$\boldsymbol{b} = \begin{pmatrix} \vdots \\ b_{-2} \\ b_{-1} \\ b_0 \\ b_1 \\ b_2 \\ \vdots \end{pmatrix} \tag{5.20}$$

and $\mathbb{L}$ is the linear operator which depends explicitly on the wave-vector k and t.

Based on the simulation results, we assume that the perturbation is only in the gradient direction, *i.e.* $k_x = 0$. Therefore, the linear dependence on time disappears (see eq. (5.18)) and $\mathbb{L}$ becomes periodic in time due to the oscillating nature of the homogeneous solution. Notice that in this case, the correction of the plane-wave perturbation becomes irrelevant, *i.e.* the result would have been the same having used $\Psi_1(\boldsymbol{r}, \theta, t) = \bar{\Psi}_1(\theta, t)\mathrm{e}^{\mathrm{i}k_y y}$. From a theoretical point of view, the periodic nature of linear operator allows us to use the Floquet's theorem, which is the analogue of Bloch's theorem in condensed matter. It states that the solution of eq. (5.19) has the form $\boldsymbol{b}(t) = \sum_{\mathrm{i}} c_{\mathrm{i}}\mathrm{e}^{\mu_{\mathrm{i}}t}\boldsymbol{x}_{\mathrm{i}}(t)$, where $\boldsymbol{x}_{\mathrm{i}}(t)$ is a T-periodic function and c_{i} are coefficients determined by the initial conditions. The μ_{i} coefficients are called Floquet exponents and have the same interpretation as the eigenvalues, since $\boldsymbol{x}_{\mathrm{i}}(t)$ are bounded functions.

Before attempting the Floquet method, we can solve eq. (5.19) numerically by truncating to order $a_{\pm 10}$ with a complex random initial condition of amplitude. In order to analyze if the solution is stable or not, we plot the maximum value of $|b_n|$ for all n from -10 to 10 and between $D_r t = 0$ and $D_r t = 1000$ in fig. 5.21. Furthermore, we also show the plots for the cases up to order $a_{\pm 3}$ and $a_{\pm 2}$ in order to see what is the minimum number of modes needed to see the instability. In this regard, we obtained that all this phenomenon can be explained by the first three Fourier modes. However, as discussed in chapter 3, we have an approximate numerical solution to order $a_{\pm 2}$, and the multiscale analysis fails for higher orders, therefore

nothing is gained by using the Floquet's method at this stage. Other approximations should be considered and it is left as future work.

The numerical results agree with the simulations, revealing a critical wave-length of $\lambda_c \approx 2200\,\mu\text{m}$ which is very close to the critical system size shown in figs. 5.14, 5.15, and 5.16, for the parameters $\rho = 10$, $\dot{\gamma} = 10$, and $\beta = 0.7$.

We can further study the stability of the homogeneous solution when considering long-range interactions. As before, we assume that the perturbation is only in the gradient interaction. To this end, we need the perturbed velocity field $\boldsymbol{u}_1$ produced by the perturbed active stress tensor $\Sigma_{ij} = \sigma_0 \int \Psi_1(p_i p_j - \delta_{ij}/2)\mathrm{d}^2 p$, which is given by (following the Green method)

$$\begin{aligned} u_{1,i} &= \int A_{ij}(y-y')\frac{\partial}{\partial y}\Sigma_{1,yj}(y')\mathrm{d}y' = i\sigma_0 k_y \int A_{ij}(y-y')e^{ik_y y'}\mathrm{d}y' \int \bar{\Psi}_1 \left(p_y p_j - \delta_{y,j}/2\right)\mathrm{d}^2 p \\ &= i\sigma_0 k_y \tilde{A}_{ij}(k_y) e^{ik_y y} \int \bar{\Psi}_1 \left(p_y p_j - \delta_{y,j}/2\right)\mathrm{d}^2 p, \end{aligned} \tag{5.21}$$

where $\tilde{A}_{ij} = \frac{1}{8\pi\eta}\left(\delta_{ij}/k^2 - k_i k_j/k^4\right)$ is the Oseen tensor in Fourier space. As a result, the perturbed velocity field is

$$\boldsymbol{u}_1 = \frac{-\sigma_0}{8\pi\eta} \int \bar{\Psi}_1 p_x p_y \mathrm{d}^2 p \hat{\boldsymbol{x}}, \tag{5.22}$$

which enters into the Jeffery equation

$$\dot{\theta}_1 = \frac{\partial u_{1,x}}{\partial y}\frac{1}{2}(\beta\cos(2\theta) - 1). \tag{5.23}$$

Considering the angular Fourier decomposition of the perturbation, $\bar{\Psi}_1 = \sum b_n(t)e^{in\theta}$, and the rescaled variables given by (3.3), (3.4), and (3.5) plus $y \to yD_r/V_0$, the evolution of the orientation due to the perturbation is

$$\dot{\theta}_1 = -i\frac{\sigma_0}{32\eta g}(b_2 - b_{-2})e^{ik_y y}. \tag{5.24}$$

Using the parameters for *E. Coli*, $\sigma_0 \approx 2.3\,\text{pN m}$, $g \approx 80\,\mu\text{m}^3/\text{s}$, and the viscosity of water at room temperature $\eta \approx 10 \times 10^{-3}\,\text{Ns/m}^2$, we have $\sigma_0/(\eta g) \sim 10$. The perturbed equation becomes

$$\frac{\partial \bar{\Psi}_1}{\partial t} = -i\boldsymbol{p}\cdot\boldsymbol{k}\bar{\Psi}_1 + i\dot{\gamma}k_x t\sin\theta\bar{\Psi}_1 - \frac{\partial(\dot{\theta}\bar{\Psi}_1)}{\partial\theta} + i\frac{\sigma_0}{32\eta g}(b_2 - b_{-2})\frac{\partial\Psi_0}{\partial\theta} + \frac{\partial^2\bar{\Psi}_1}{\partial\theta^2} + I\left[\Psi_0, \bar{\Psi}_1\right]. \tag{5.25}$$

The effect of the long-range interaction is to add constants into the matrix operator $\mathbb{L}(\boldsymbol{k}, t)$. By numerically solving the linear problem truncated up to order $a_{\pm 10}$ and $b_{\pm 10}$, with a complex random initial condition of amplitude, we obtain that the instability prevails, but the long-range interactions shift the critical wave-length to a smaller but similar value, as seen in figs 5.22, 5.23, 5.24.

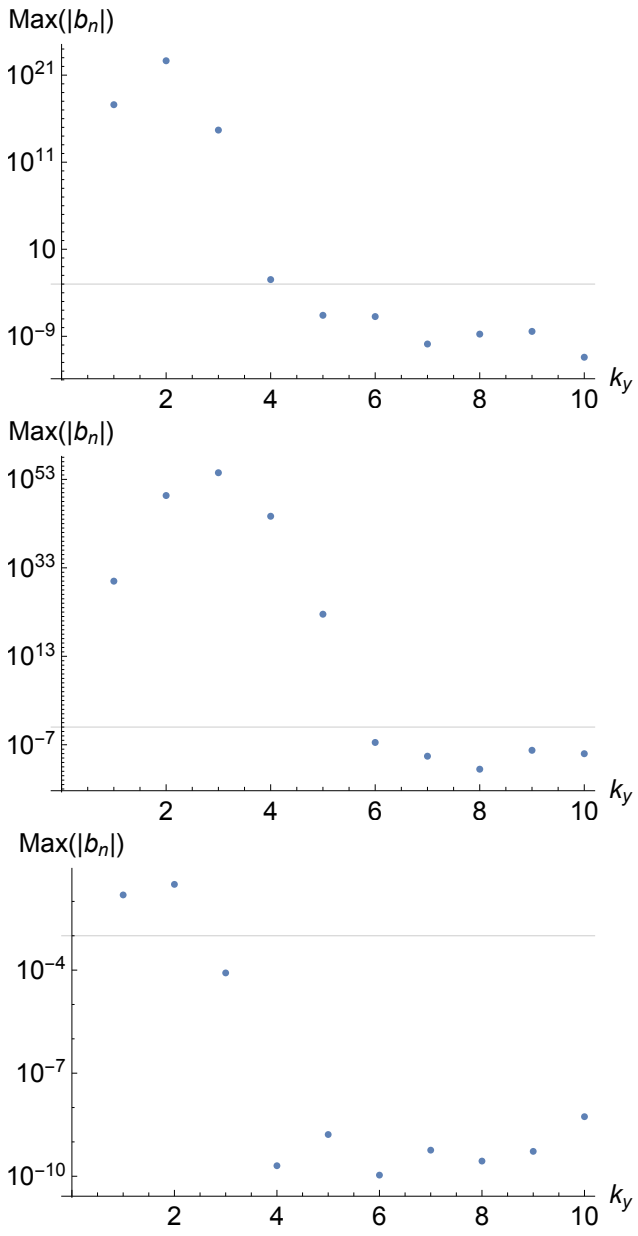

Figure 5.21: Linear-Log plot of the maximum value of $|b_n|$ at $D_r t = 1000$, as a function of the wave-vector k_y. We assume $k_x = 0$. The vertical line corresponds to 0.001. The solutions were obtained by truncating the system at $n = 10$ (top), $n = 3$ (middle), and $n = 2$ (bottom), for both the homogeneous solution and the perturbation. The parameters used were $\rho = 10$ and $\dot{\gamma} = 10$. The figure in the top reveals a critical wave-length of $\lambda_c \approx 2200\,\mu\text{m}$.

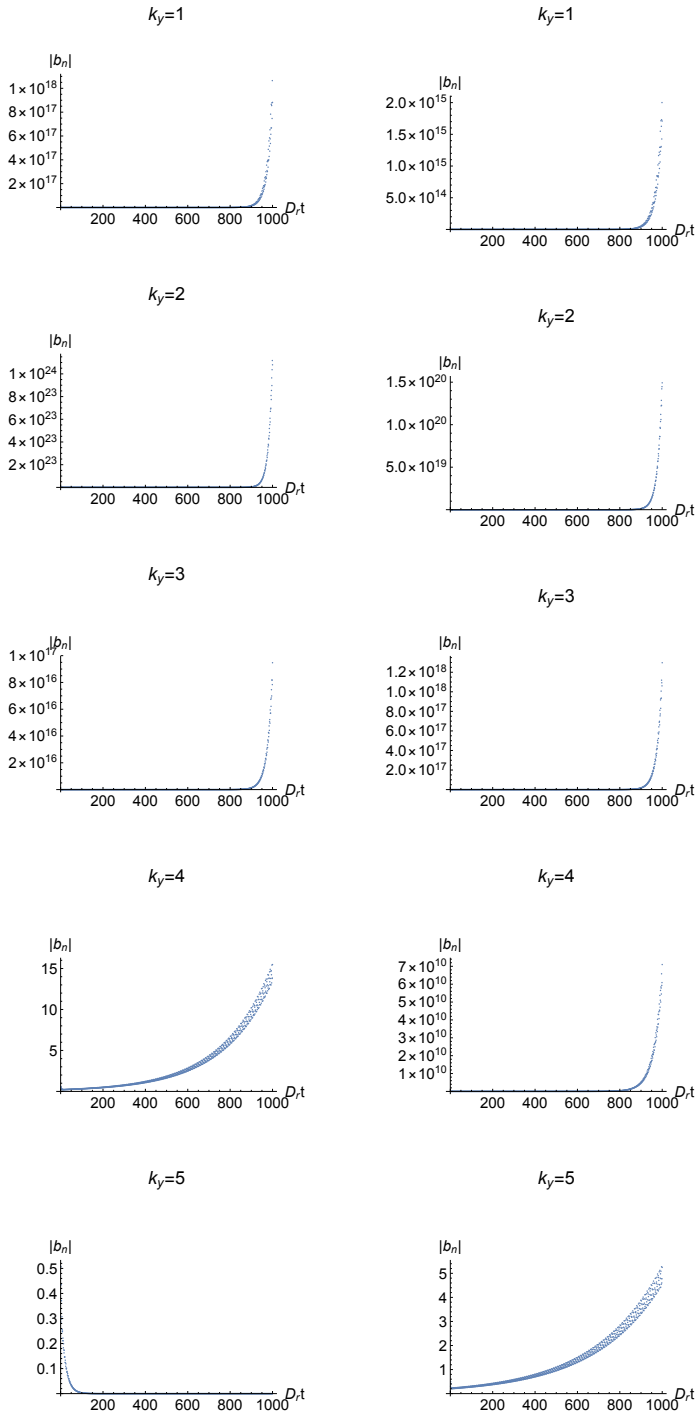

Figure 5.22: Evolution of the modules of all the Fourier modes $|b_n|$ for different wave-vectors k_y with (right) and without (left) long-range hydrodynamic interactions. We assume $k_x = 0$. The solutions were obtained by truncating the system at $n = 10$ for both the homogeneous solution and the perturbation. The parameters used were $\rho = 10$, $\beta = 0.7$ and $\dot{\gamma} = 10$.

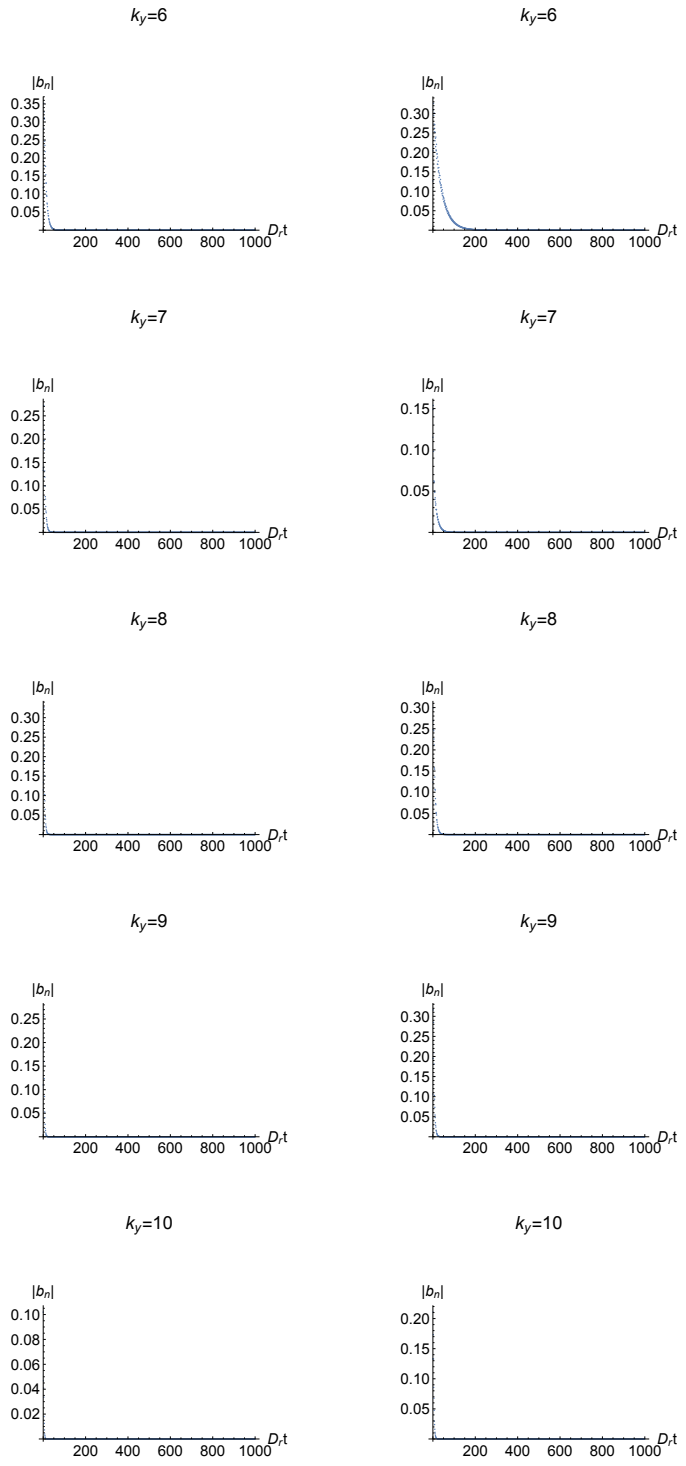

Figure 5.23: Continuation of figure 5.22

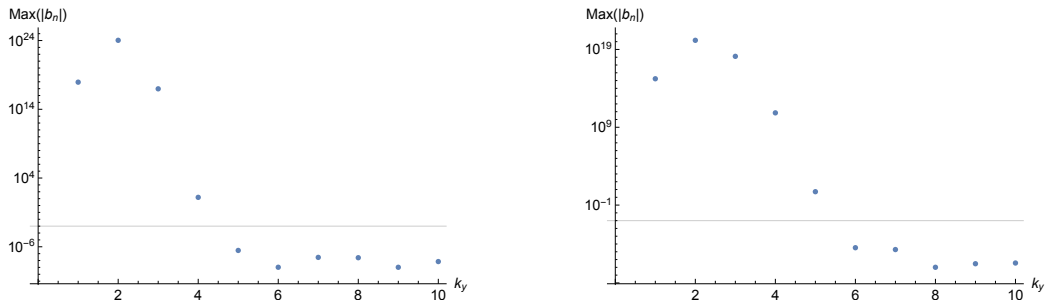

Figure 5.24: Evolution of the modules of all the Fourier modes $|b_n|$ for different wave-vectors k_y with (right) and without (left) long-range hydrodynamic interactions. We assume $k_x = 0$. The solutions were obtained by truncating the system at $n = 10$ for both the homogeneous solution and the perturbation. The parameters used were $\rho = 10$, $\beta = 0.7$ and $\dot{\gamma} = 10$.

5.4.1 Three-Dimensional Simulations

By performing various simulations varying the density and the size of the system, we find a similar kind of spatial structures. We imposed a uniform shear flow $\boldsymbol{u} = \dot{\gamma} z \hat{\boldsymbol{x}}$. The simulations were done considering wall aligning BC (see figs. 5.25, 5.26, 5.27, 5.28, 5.29, 5.30, 5.31, and 5.32) and Lees-Edward BC (see figs. 5.33, 5.34, 5.35, and 5.36). Since we are working in three dimensions, we take averages in two orthogonal directions and plot them as a function of third coordinate. For example, in fig. 5.25 we show the number density integrated in the $\hat{\boldsymbol{x}}$ and $\hat{\boldsymbol{y}}$ direction, $\rho_{xy}(z)$ and in fig. 5.26 we show the average orientation weighted by the density, $\langle p_x \rangle_{xy} \rho_{xy}(z)$. Unlike the two-dimensional case, the origin of the spatial structures depends on the system size in a non-trivial way, but they share some similarities with the two-dimensional case. For example, the instability only appears in the gradient direction (z-axis) whereas in the rest remains homogenous (see figs. 5.29 5.30 5.31 5.32). We note as well that the evolution of p_y is not oscillatory, but has a persistence to a given direction, as shown in fig. 5.27. In figs. 5.375.385.395.40 we show as well the formation of several bands when the shear rate is large in a periodic-like system.

More simulations should be considered in order to understand the origin of the instability, by varying the system size, the concentration and the shear rates. This is left as future work.

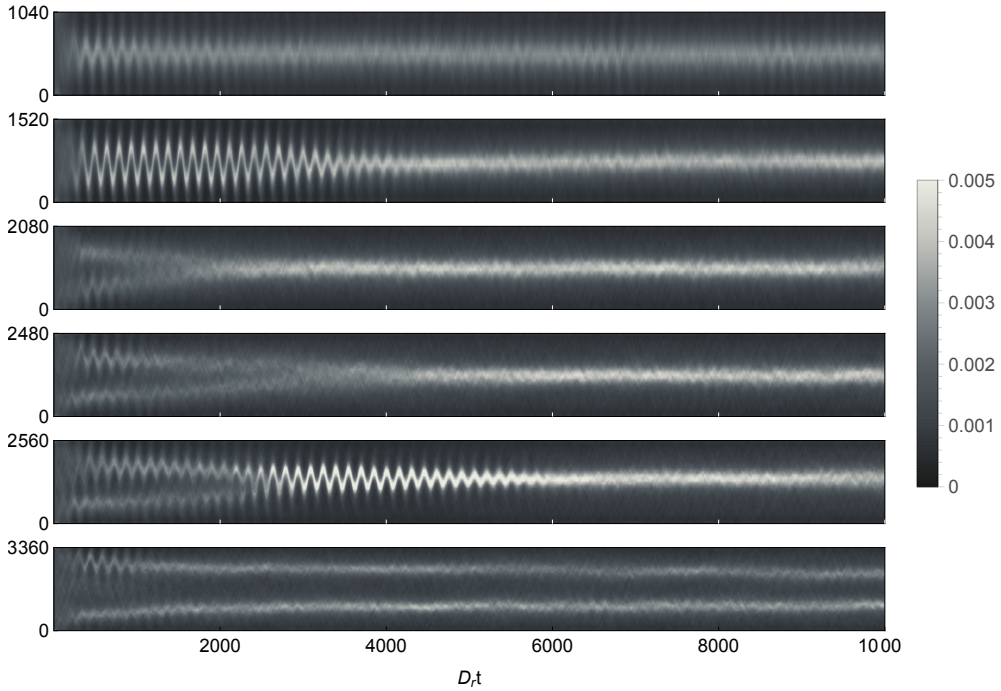

Figure 5.25: $\rho_{xy}(z)$ in time (horizontal axis) space (vertical axis, in µm) representation obtained from DSMC simulations, for different L_z and fixed $L_x = Ly = 160\,\mu\text{m}$. $\rho = 10$, $\dot{\gamma} = 10$, and $\beta = 0.7$. Wall-aligning boundary condition were applied.

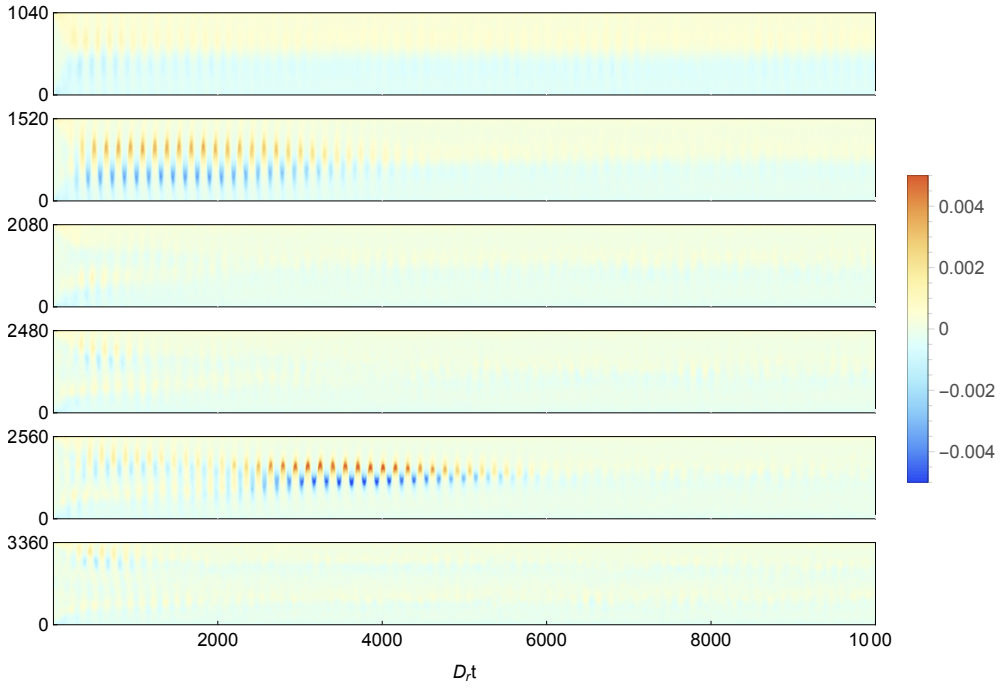

Figure 5.26: $\langle p_x \rangle_{xy} \rho_{xy}(z)$ in time (horizontal axis) space (vertical axis, in µm) representation obtained from DSMC simulations, for different L_z and fixed $L_x = Ly = 160\,\mu\text{m}$. $\rho = 10$, $\dot{\gamma} = 10$, and $\beta = 0.7$. Wall-aligning boundary condition were applied.

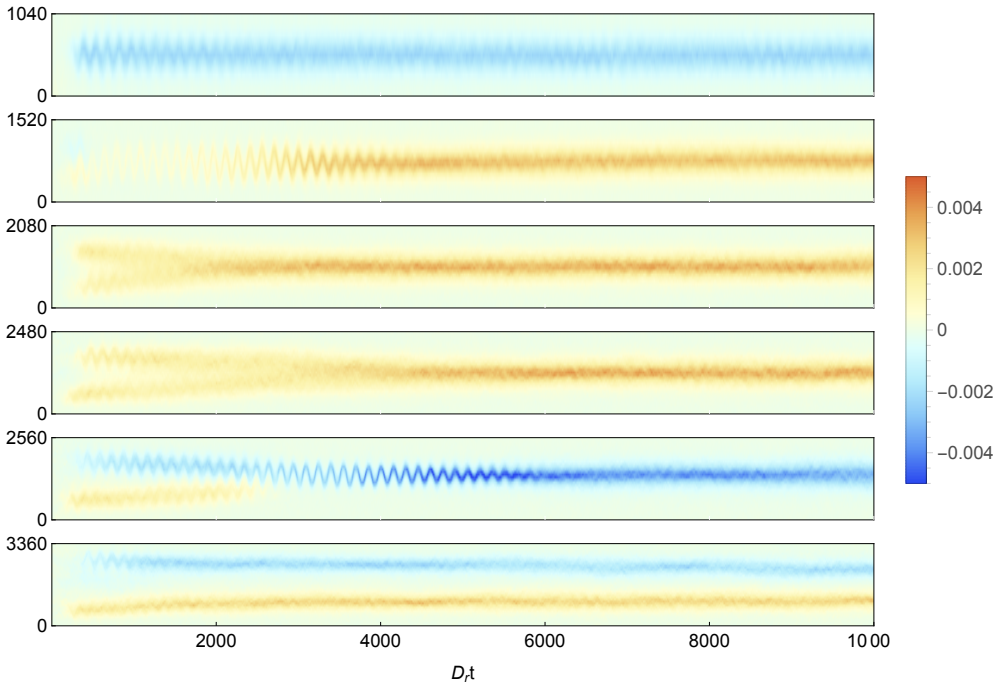

Figure 5.27: $\langle p_y \rangle_{xy} \rho_{xy}(z)$ in time (horizontal axis) space (vertical axis, in µm) representation obtained from DSMC simulations, for different L_z and fixed $L_x = Ly = 160\,\mu\text{m}$. $\rho = 10$, $\dot{\gamma} = 10$, and $\beta = 0.7$. Wall-aligning boundary condition were applied.

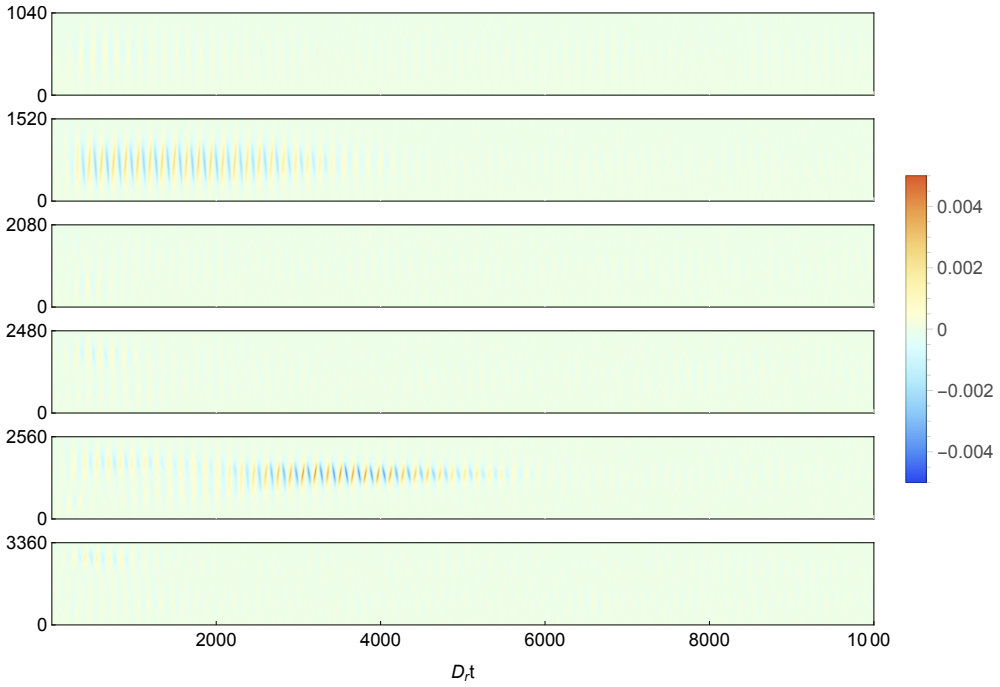

Figure 5.28: $\langle p_z \rangle_{xy} \rho_{xy}(z)$ in time (horizontal axis) space (vertical axis, in µm) representation obtained from DSMC simulations, for different L_z and fixed $L_x = Ly = 160\,\mu\text{m}$. $\rho = 10$, $\dot{\gamma} = 10$, and $\beta = 0.7$. Wall-aligning boundary condition were applied.

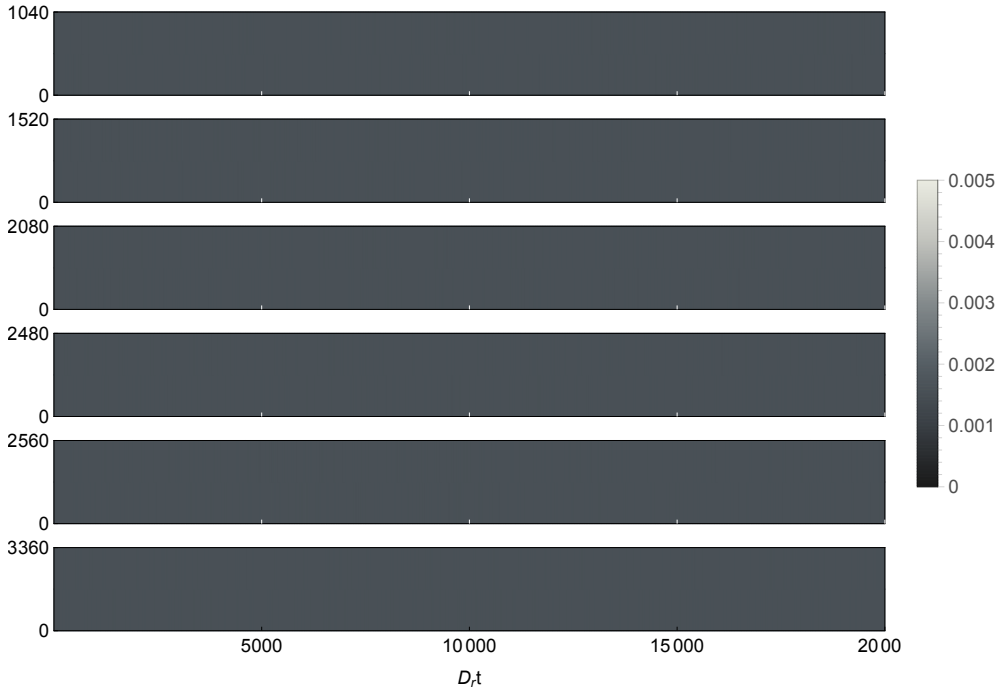

Figure 5.29: $\rho_{yz}(x)$ in time (horizontal axis) space (vertical axis, in µm) representation obtained from DSMC simulations, for different L_z and fixed $L_x = Ly = 160\,\mu\text{m}$. $\rho = 10$, $\dot{\gamma} = 10$, and $\beta = 0.7$. Wall-aligning boundary condition were applied.

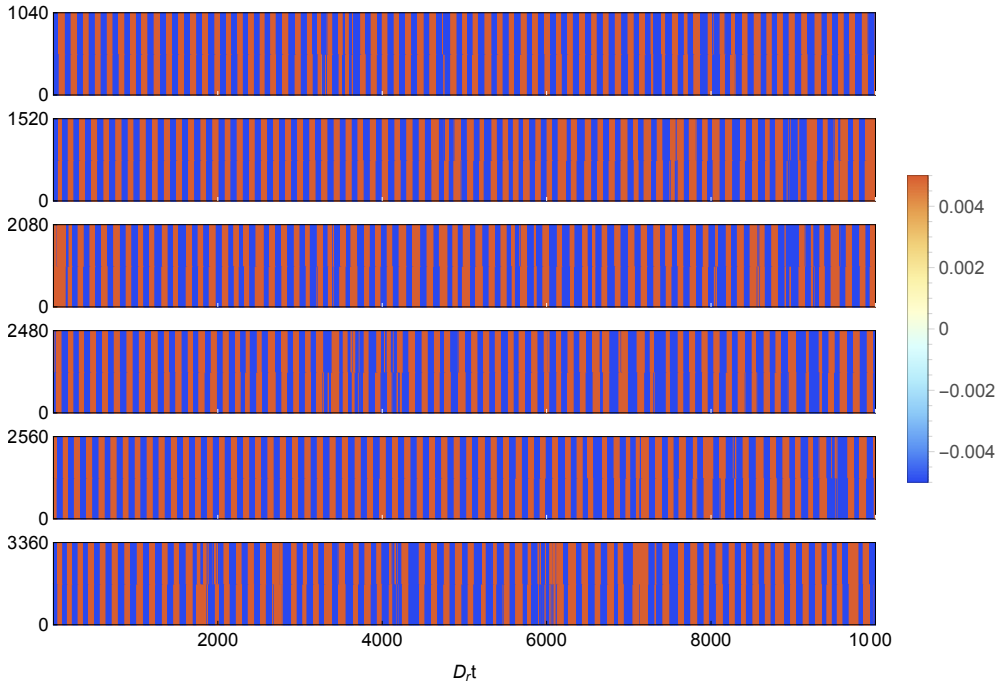

Figure 5.30: $\langle p_x \rangle_{yz} \rho_{yz}(x)$ in time (horizontal axis) space (vertical axis, in µm) representation obtained from DSMC simulations, for different L_z and fixed $L_x = Ly = 160\,\mu\text{m}$. $\rho = 10$, $\dot{\gamma} = 10$, and $\beta = 0.7$. Wall-aligning boundary condition were applied.

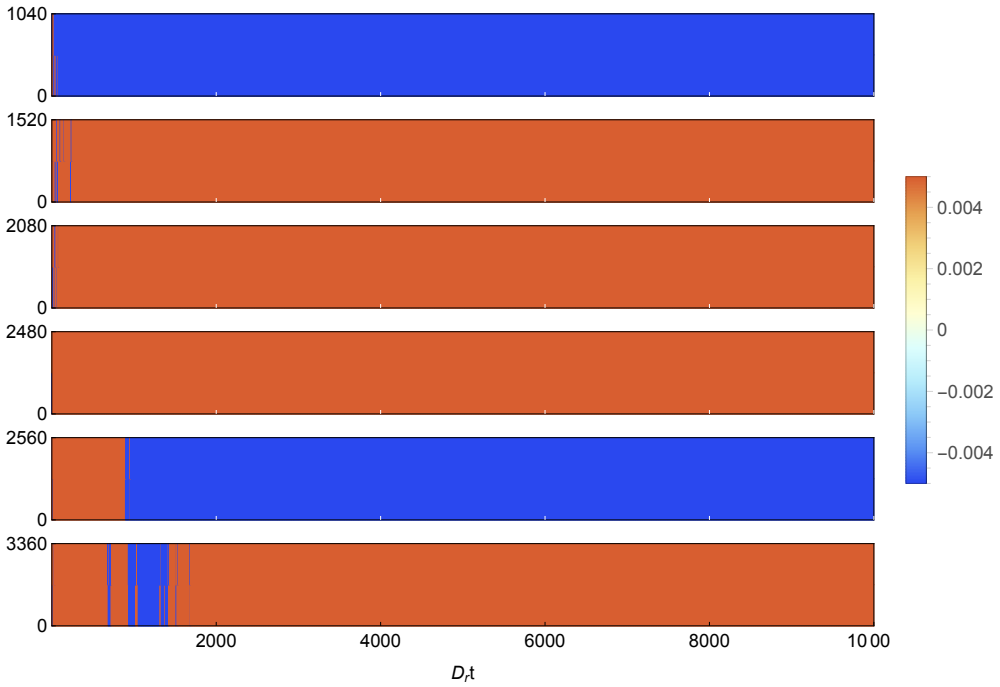

Figure 5.31: $\langle p_y \rangle_{yz} \rho_{yz}(x)$ in time (horizontal axis) space (vertical axis, in µm) representation obtained from DSMC simulations, for different L_z and fixed $L_x = Ly = 160\,\mu\text{m}$. $\rho = 10$, $\dot{\gamma} = 10$, and $\beta = 0.7$. Wall-aligning boundary condition were applied.

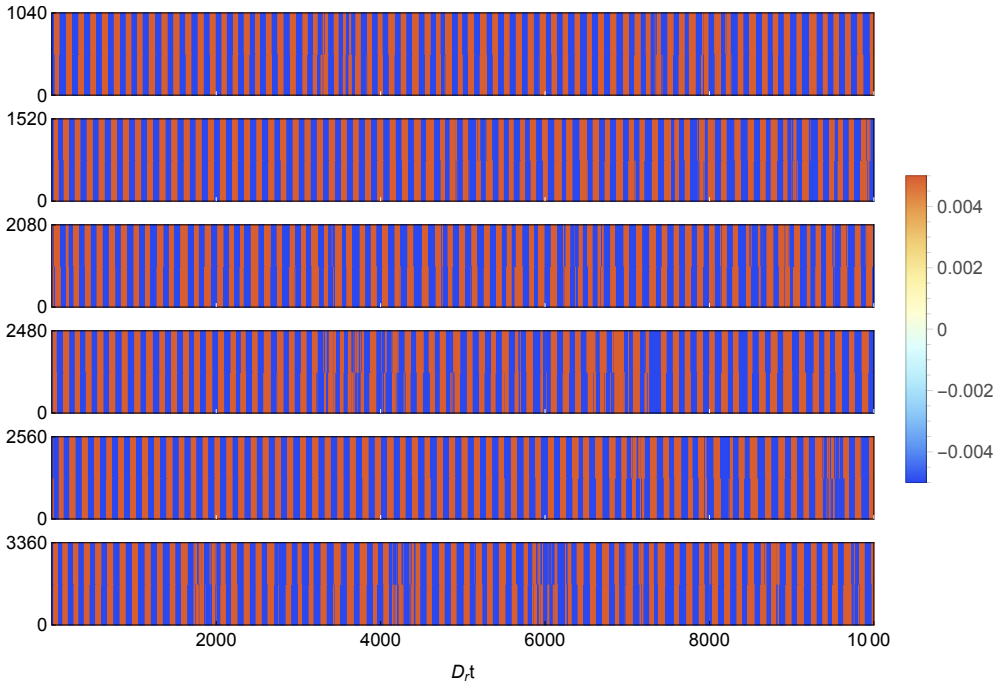

Figure 5.32: $\langle p_z \rangle_{yz} \rho_{yz}(x)$ in time (horizontal axis) space (vertical axis, in µm) representation obtained from DSMC simulations, for different L_z and fixed $L_x = Ly = 160\,\mu\text{m}$. $\rho = 10$, $\dot{\gamma} = 10$, and $\beta = 0.7$. Wall-aligning boundary condition were applied.

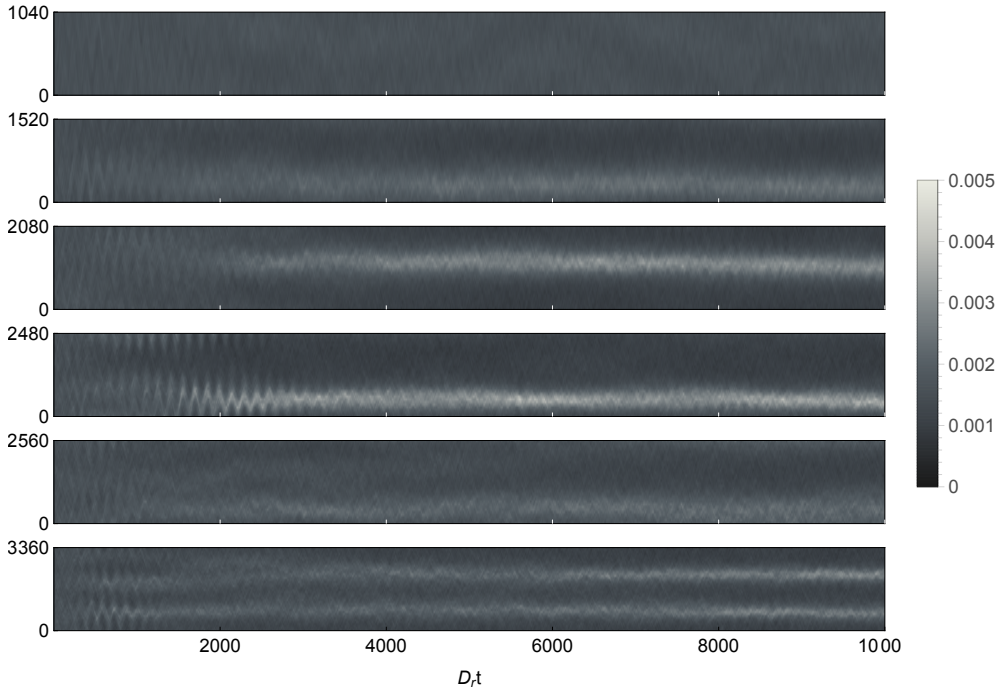

Figure 5.33: $\rho_{xy}(z)$ in time (horizontal axis) space (vertical axis, in µm) representation obtained from DSMC simulations, for different L_z and fixed $L_x = Ly = 160\,\mu\text{m}$. $\rho = 10$, $\dot{\gamma} = 10$, and $\beta = 0.7$. Lees-Edward boundary condition were applied.

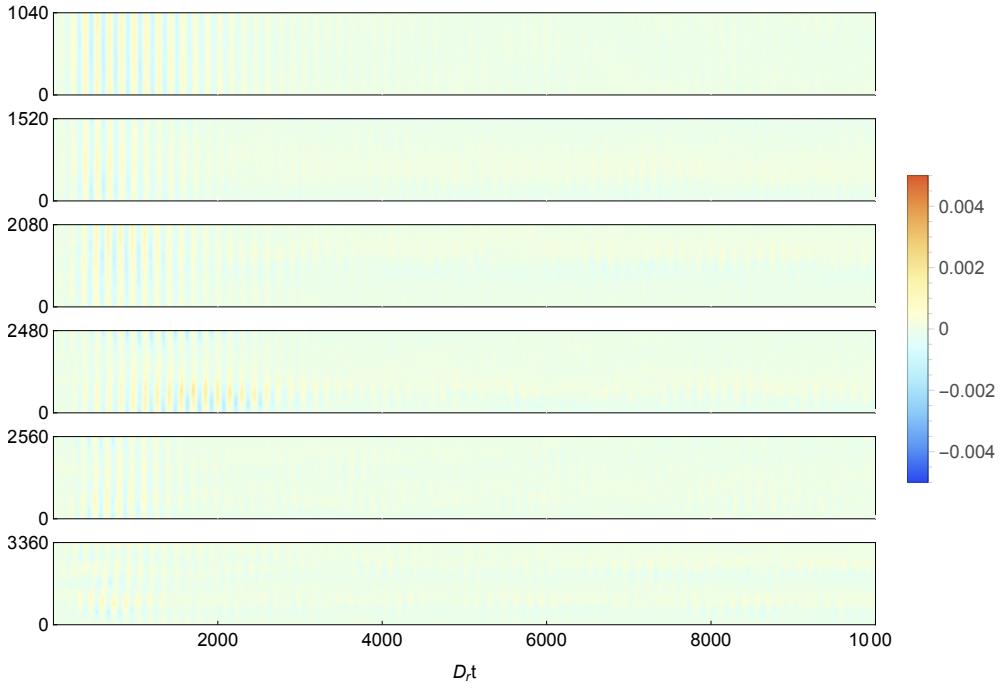

Figure 5.34: $\langle p_x \rangle_{xy} \rho_{xy}(z)$ in time (horizontal axis) space (vertical axis, in µm) representation obtained from DSMC simulations, for different L_z and fixed $L_x = Ly = 160\,\mu\text{m}$. $\rho = 10$, $\dot{\gamma} = 10$, and $\beta = 0.7$. Lees-Edward boundary condition were applied.

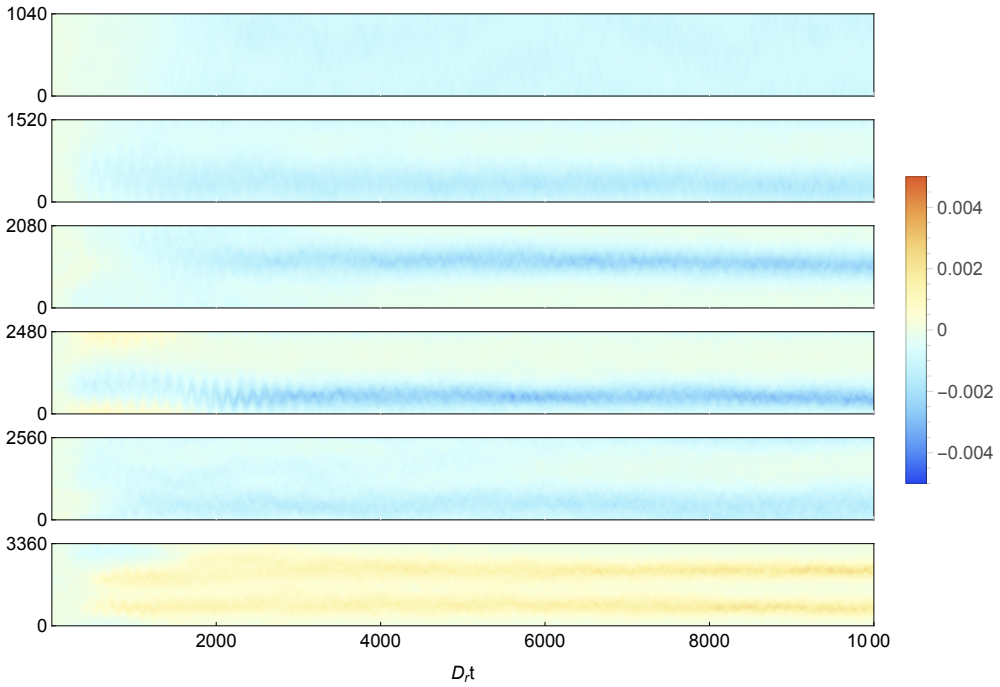

Figure 5.35: $\langle p_y \rangle_{xy} \rho_{xy}(z)$ in time (horizontal axis) space (vertical axis, in µm) representation obtained from DSMC simulations, for different L_z and fixed $L_x = Ly = 160\,\mu\text{m}$. $\rho = 10$, $\dot{\gamma} = 10$, and $\beta = 0.7$. Lees-Edward boundary condition were applied.

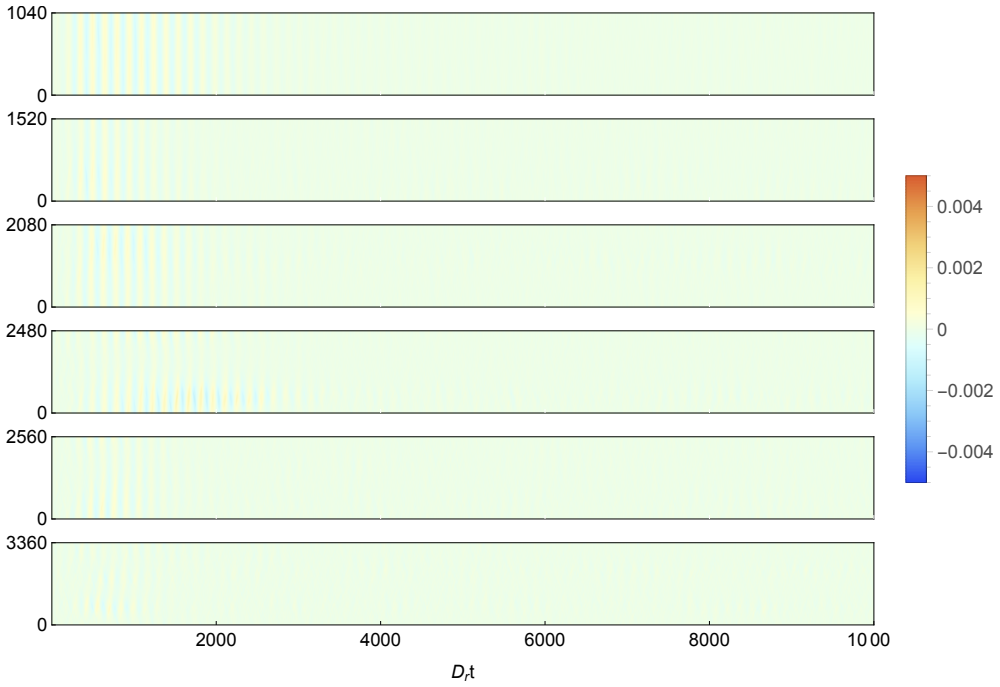

Figure 5.36: $\langle p_z \rangle_{xy} \rho_{xy}(z)$ in time (horizontal axis) space (vertical axis, in µm) representation obtained from DSMC simulations, for different L_z and fixed $L_x = Ly = 160\,\mu\text{m}$. $\rho = 10$, $\dot{\gamma} = 10$, and $\beta = 0.7$. Lees-Edward boundary condition were applied.

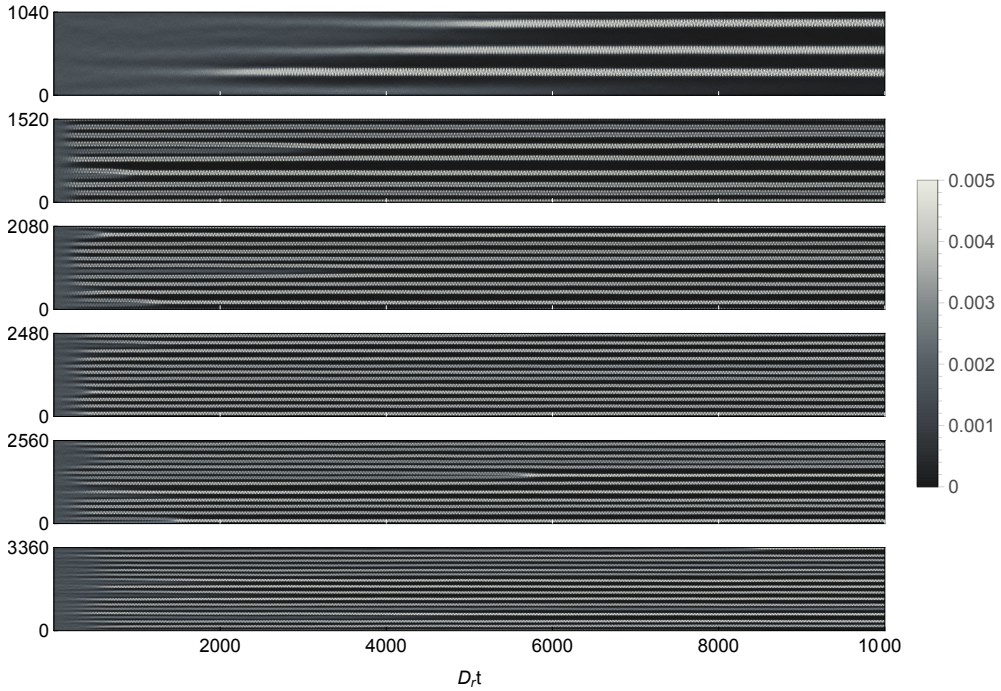

Figure 5.37: $\rho_{xy}(z)$ in time (horizontal axis) space (vertical axis, in µm) representation obtained from DSMC simulations, for different L_z and fixed $L_x = Ly = 160\,\mu\text{m}$. $\rho = 10$, $\dot{\gamma} = 100$, and $\beta = 0.7$. Lees-Edward boundary condition were applied.

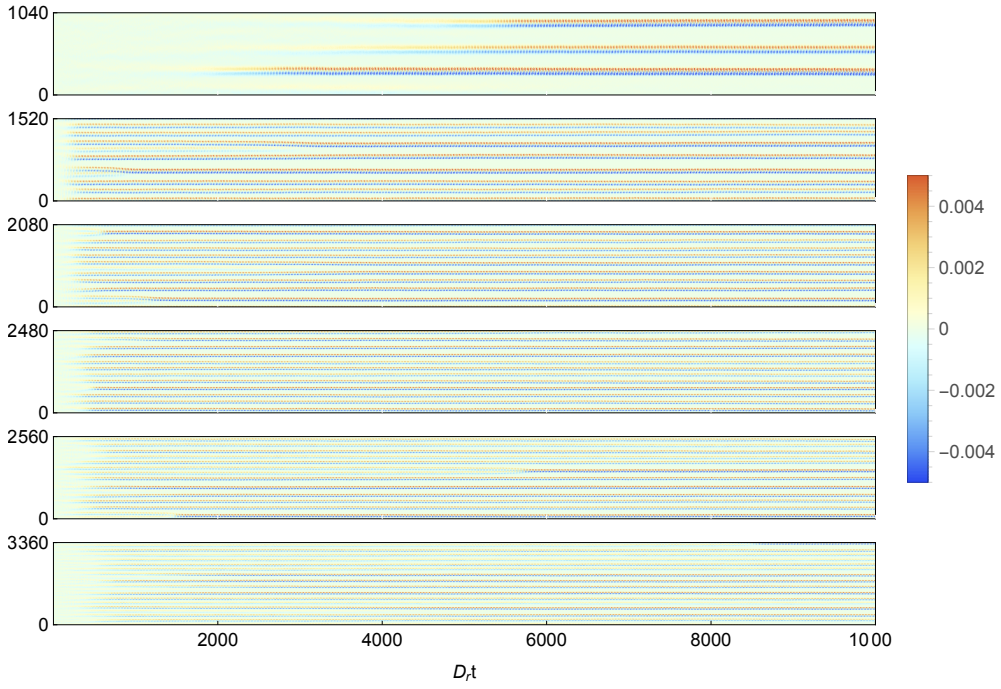

Figure 5.38: $\langle p_x \rangle_{xy} \rho_{xy}(z)$ in time (horizontal axis) space (vertical axis, in µm) representation obtained from DSMC simulations, for different L_z and fixed $L_x = Ly = 160\,\mu\text{m}$. $\rho = 10$, $\dot{\gamma} = 100$, and $\beta = 0.7$. Lees-Edward boundary condition were applied.

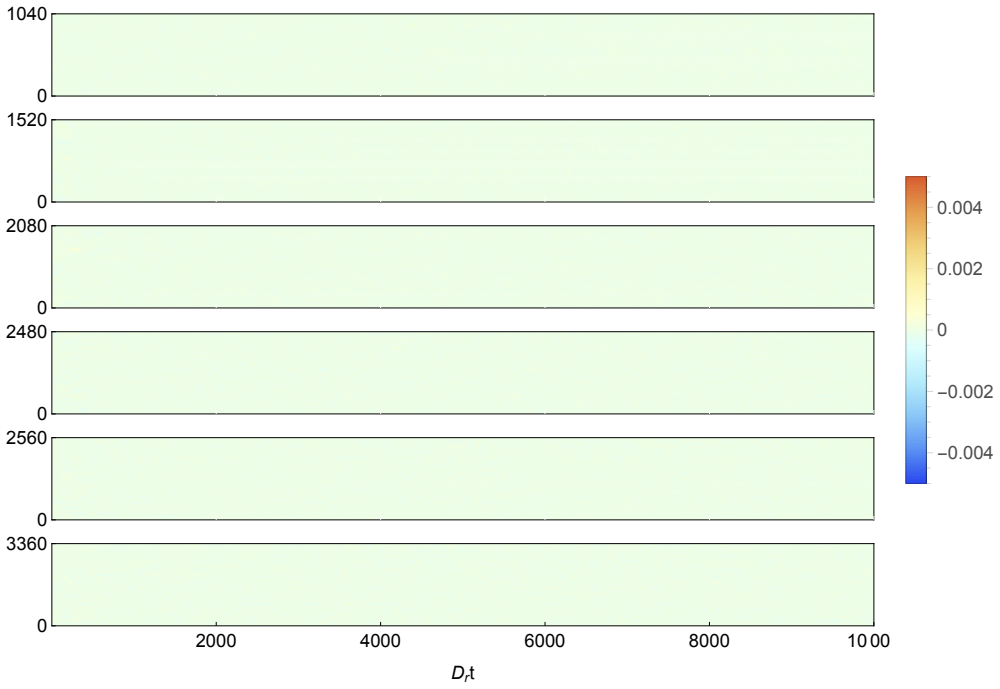

Figure 5.39: $\langle p_y \rangle_{xy} \rho_{xy}(z)$ in time (horizontal axis) space (vertical axis, in µm) representation obtained from DSMC simulations, for different L_z and fixed $L_x = Ly = 160\,\mu\text{m}$. $\rho = 10$, $\dot{\gamma} = 100$, and $\beta = 0.7$. Lees-Edward boundary condition were applied.

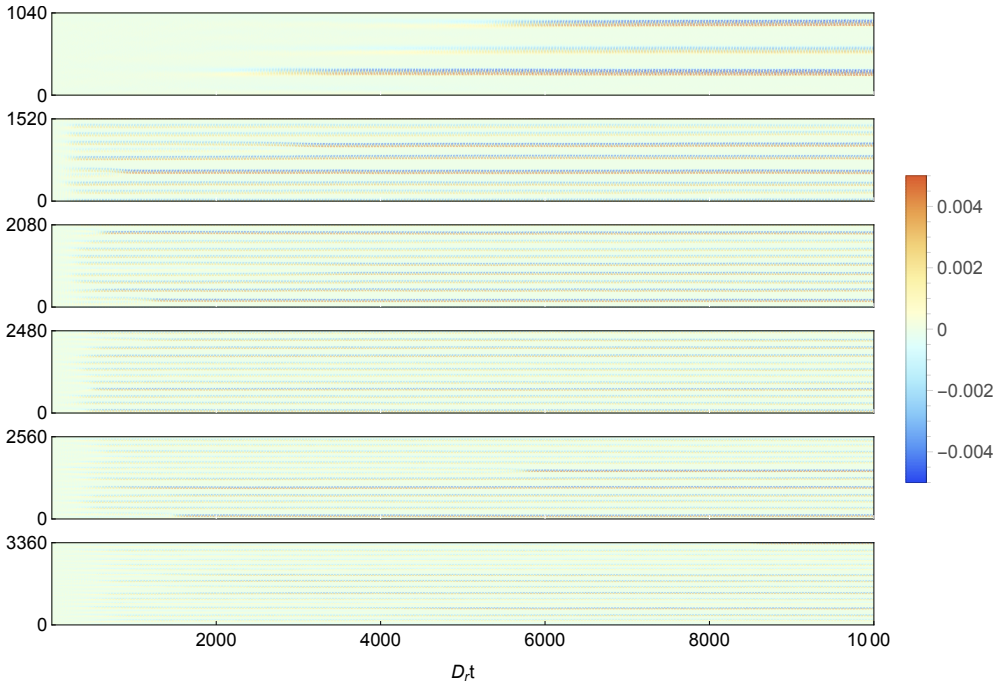

Figure 5.40: $\langle p_z \rangle_{xy} \rho_{xy}(z)$ in time (horizontal axis) space (vertical axis, in µm) representation obtained from DSMC simulations, for different L_z and fixed $L_x = Ly = 160\,\mu\text{m}$. $\rho = 10$, $\dot{\gamma} = 100$, and $\beta = 0.7$. Lees-Edward boundary condition were applied.

Chapter 6

Conclusions and Perspectives

In this thesis we extended the kinetic theory of dilute bacterial suspensions to the semidilute case by including short-range aligning collisions through a Boltzmann collision integral. This model was studied theoretically and numerically in detail for a homogeneous suspension of swimmers with nematic and polar interactions, and for non-homogeneous bacterial suspensions of polar interacting swimmers.

In chapter 2 we derived the kinetic equation for the distribution function of positions and orientations, considering short-range interactions through a Boltzmann collision integral. The interactions considered were completely inelastic polar and nematic aligning collisions, which were expressed in detail in two dimensions. Finally, we expanded the distribution function in angular Fourier modes for the case of a simple shear flow, obtaining the evolution of each mode for both kinds of interactions.

In chapter 3 we studied in detail the kinetic equation in two dimensions for a homogeneous suspension under a uniform shear flow. First, we analyzed the polar interacting case. Although analytic solutions were not possible to find even when truncating the equations to the first two modes, we employed an ansatz in a multi-scale scheme in which we identified different time-scales for the polar interacting case near the critical density. As a result, we obtained simplified expressions for the nematic and polar modes in the Fourier expansion, as well as for the active stress tensor. This last quantity revealed an oscillatory behavior with a frequency of the order of the shear rate of the imposed uniform shear flow, due to the interplay between the Jeffery's orbit and the short-range aligning collisions, with an average that remained close to the one obtained in the dilute regime. Furthermore, we obtained the scaling laws of the root mean square and the standard deviation of the the active shear stress. Then, we tried to perform the same analysis truncating to the first three modes, but we faced different inconsistencies due to the ansatz used. Finally, we solved numerically the equations for the modes up to order 10, for which we obtained a new transition for high shear rates, in which we lose the polar phase. For the nematic interacting case, we found that a similar transition takes place, this time related to the fourth mode enslaved to the second mode. In fact, all the odd modes go to zero, including the average orientation even in the oscillatory phase, unlike the polar interacting case. Finally, numerical solutions, considering up to the tenth mode, reveal a subcritical transition in which the nematic phase is lost.

In chapter 4 we studied numerically the effect of polar interactions in magnetotactic bacteria under a simple shear flow and a constant magnetic field. The effect of the magnetic interaction is to shift the average polarization close to the direction of the magnetic field and to increase or decrease the critical density with respect to the non interacting case if the magnetic field is aligned with the flow or opposed to it, respectively.

In chapter 5 we studied inhomogeneous suspensions in two and three dimensions. First, we tested different boundary conditions, concluding that the only boundary condition able to reproduce the homogeneous solution is the anti-specular collision with the wall. Then we solved the kinetic equation by employing DSMC simulations and adhoc boundary conditions that reproduce two phenomena observed experimentally: upstream swimming and high concentrations near the wall. Considering this boundary condition in two and three dimensions, we observe that the homogeneous solution becomes unstable and spatial localizations appear. Furthermore, this instability depends on the size of the system, appearing for systems larger than a threshold set by the shear rate. Then we ran simulations with periodic-like boundary conditions, obtaining the same results, concluding that the instability is not generated by the interaction with the walls. Having the same phenomenon in the periodic-like system, we performed a linear stability analysis of the homogenous solution by using plane-wave perturbations in the gradient direction. We found that this instability appears even when considering long-range hydrodynamic interactions. The same results were obtained in three dimensions.

6.1 Future work

There are several small contributions that could be done and were mentioned throughout this thesis: to find an ansatz up to the third mode for the homogenous solution in chapter 3 which could explain the loss of the transition for large shear rates, and could be of great help to the Floquet problem proposed in chapter 5, to consider perturbations in the flow direction in chapter 5, and to explore different parameters for the three dimensional simulations in chapter 5 in order to understand the origin of the instability.

In addition, we have already started to work in different paths that are highly connected to this thesis: the response of the fluid under a change of viscosity and the phenomenology of dense magnetotactic bacterial suspensions in three dimensional droplets.

6.1.1 Fluid Response

Until now we have not studied how the fluid is going to respond to a change in the viscosity. The most simple case corresponds to a 2D simple shear flow for an ideal bacterial suspension (i.e without interactions. In the stationary and homogeneous state, the Fokker-Planck equation for the distribution function reads

$$\frac{\partial(\dot{\theta}\Psi)}{\partial\theta} = D_{\mathrm{r}}\frac{\partial^2\Psi}{\partial\theta^2}, \tag{6.1}$$

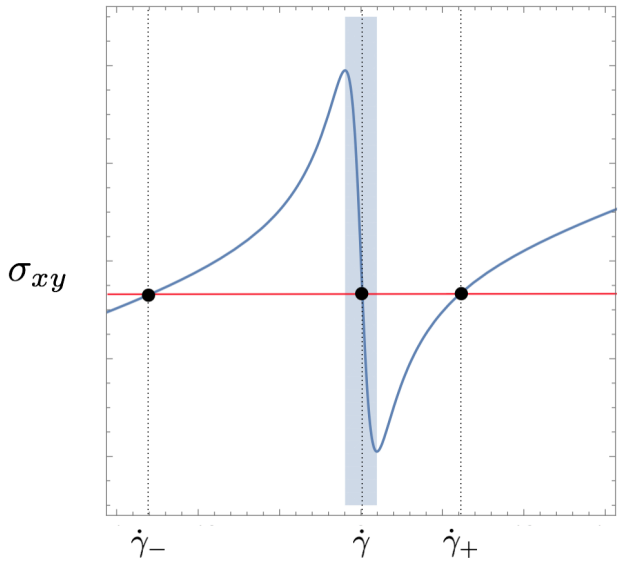

Figure 6.1: Shear stress as a function of the shear rate. The shaded region indicates the unstable values of $\dot{\gamma}$. The dots indicate the three possible solutions for a given value of σ_{xy}.

where $\dot{\theta}$ is given by (2.12). Equation (6.1) can be solved via angular Fourier series: $\Psi = \sum a_n e^{in\theta}$. Truncating to order $a_{\pm 2}$ we obtain the following expression for the shear stress tensor:

$$\Sigma_{xy} = \Sigma_{xy}^{\text{viscous}} + \Sigma_{xy}^{\text{active}} = \eta \left(1 - \frac{b}{1 + (\tau_c \dot{\gamma}^2)}\right) \dot{\gamma}, \tag{6.2}$$

where $b = \frac{|\sigma_0|\beta\rho}{16\eta}$ and $\tau_c = 1/(4D_{\text{r}})$. Figure 6.1 shows the behavior of the shear stress as a function of the shear rate $\dot{\gamma}$.

The evolution of the fluid is governed by the incompressible Navier-Stokes (NS) equation

$$\rho \frac{\partial u}{\partial t} = \frac{\partial \sigma_{xy}}{\partial y}, \tag{6.3}$$

where we have assumed that the spatial dependence is perpendicular to the flow direction, and we have used the notation $\boldsymbol{u} = u\hat{\boldsymbol{x}}$.

Given the non-newtonian shear stress of (6.2), we do not expect to have a Couette profile as a stable solution for all the shear rates. Indeed, let $u = u_0 + \delta u$, where $u_0 = \dot{\gamma} y$ is the Couette solution. To first order in δu, from the NS equation we have

$$\rho \frac{\partial \delta u}{\partial t} = \sigma'_{xy}(\dot{\gamma}_0) \frac{\partial^2 \delta v}{\partial y^2}. \tag{6.4}$$

Therefore, if $\sigma'_{xy}(\dot{\gamma}_0) < 0$ the Couette solution is unstable. So, how is the system going to evolve if it is tuned to an unstable Couette profile? We note from figure 6.1 that for a given shear stress there are three shear rates associated, one in the unstable region, and the two others in the stable region. Due to the boundary conditions, it is impossible to have just one value (whether $\dot{\gamma}_-$ or $\dot{\gamma}_+$). Nevertheless local linear profiles, as the ones shown in fig. 6.2,

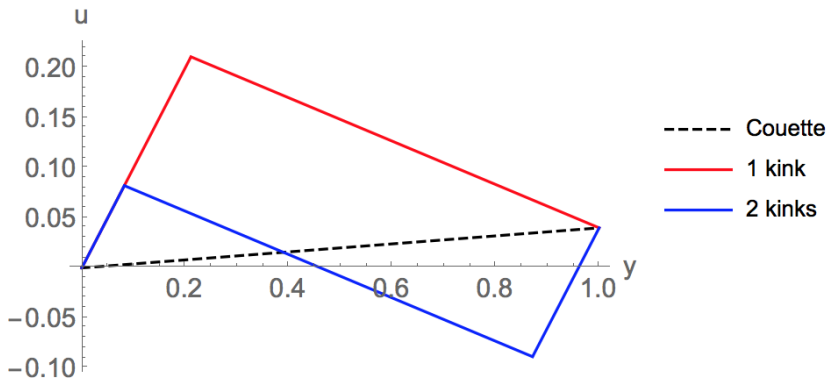

Figure 6.2: Velocity profiles for three different cases: Couette (dashed), 1-kink (red), and 2-kinks (blue). All of them satisfying the same boundary conditions. Dimensionless units.

are possible in principle, where the two shear rates of the linear profiles are located in the stable region. The condition to obtain the two stable shear rates for a given value of σ_{xy} is the continuity of the shear stress at each kink, *i.e.* $\sigma_{xy}(\dot{\gamma}_1) = \sigma_{xy}(\dot{\gamma}_2)$ (where $\dot{\gamma}_1$ and $\dot{\gamma}_2$ are the stable shear rates), leading to:

$$\dot{\gamma}_2 = \frac{-b\dot{\gamma}_1 \pm \sqrt{4(b-1)\tau_c^{-2} + (b(4+b)-8)\dot{\gamma}_1^2 - 4\tau_c^2\dot{\gamma}_1^2}}{2(1+\tau_c^2\dot{\gamma}_1^2)}. \tag{6.5}$$

If there are 2 kinks or more, these shear rates alternate. Finally, figs. 6.1 and 6.2 imply an infinite amount of solutions, by varying the number of kinks and their positions.

As preliminary results, we solved the dimensionless incompressible NS equation

$$\frac{\partial u}{\partial t} = \frac{\partial}{\partial y}\left[\left(1 - \frac{b}{1+\left(\frac{\partial u}{\partial y}\right)^2}\right)\frac{\partial u}{\partial y}\right], \tag{6.6}$$

where we have used $t \to \tau_c t$ and $y \to \sqrt{\eta\tau_c/\rho}y$. We solved the equations with explicit methods. As boundary conditions we used $u = 0$ at $y = 0$, and $u = \dot{\gamma}$ at $y = 1$. In fig. 6.3 we show the velocity profiles for two initial conditions. Corroborating our previous analytical results, there are plenty of stable solutions, where the evolution towards one of the solutions depends solely on the initial condition.

On more physical grounds we know that the number of kinks is in fact limited by the minimum size of each region with constant shear rate, and ultimately it cannot be shorter than one mean free path. Furthermore, we expect that the system would try to minimize the number of kinks. Inspired by this idea we add an artificial viscosity that smooths out the kinks. Its deduction is based on microscopic theories (kinetic theory for example). The new equation reads:

$$\frac{\partial u}{\partial t} = \frac{\partial \sigma_{xy}}{\partial y} + c\frac{\partial^4 u}{\partial y^4}, \tag{6.7}$$

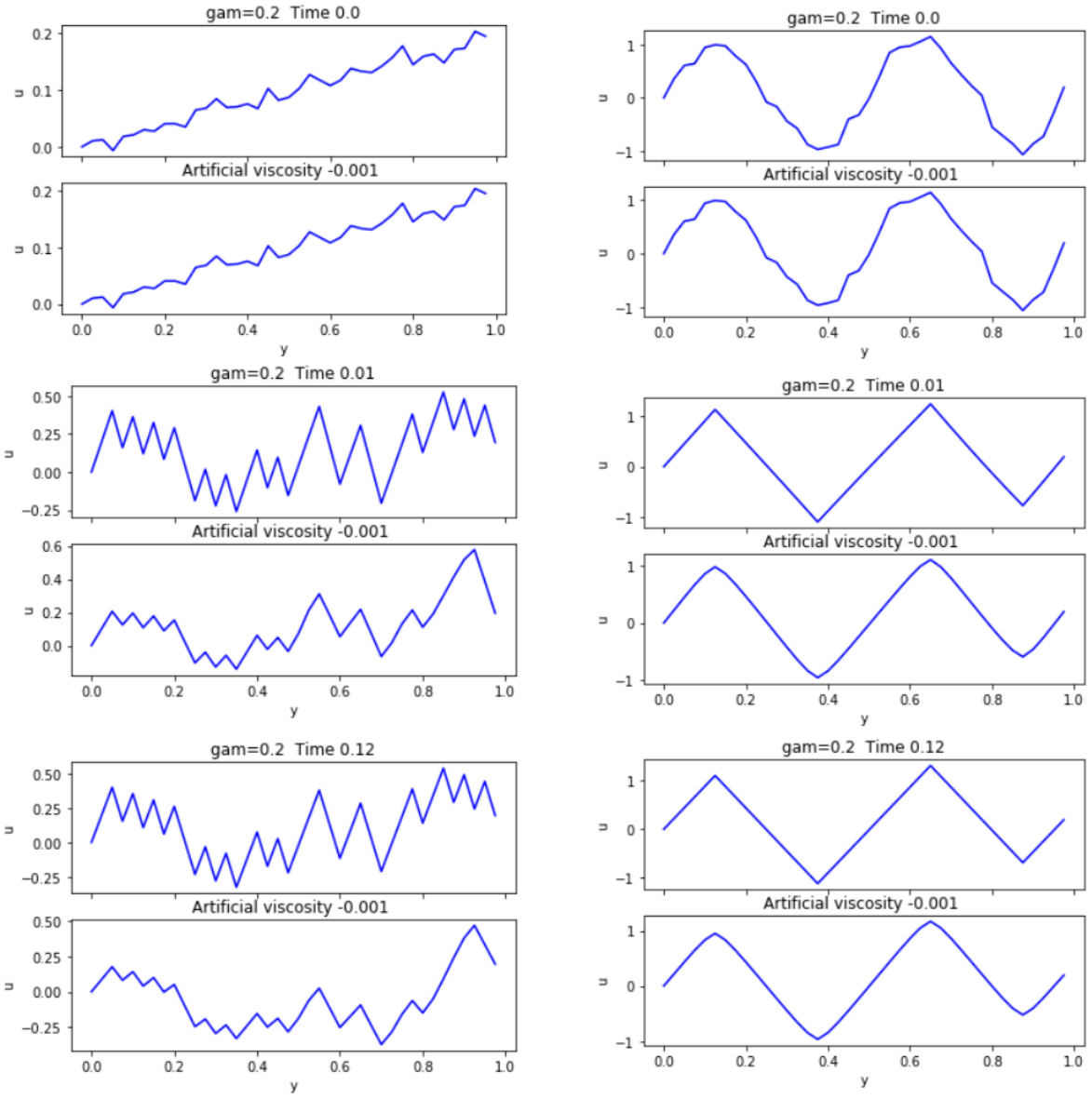

Figure 6.3: Velocity profiles at different times, for two initial conditions: Couette with noise (left) and sinusoidal with noise(right). At each time we have the solution of NS equation and the solution NS with artificial viscosity $c = -0.001$. Here gam= $\dot{\gamma}$. Dimensionless values.

where c is the artificial viscosity. Figure 6.3 shows the velocity profile at different times with $c = -0.001$. Increasing the artificial viscosity leads to even smoother curves as shown in fig. 6.4. It is worth pointing out the fast evolution towards the equilibrium solution in both cases, with and without artificial viscosity.

One of the possible path to follow is to find an underlying variational principle that fix the number of kinks present in the system. By solving this problem we can potentially explain the negative viscosity measurements as a local phenomenon near the walls where the local velocity profile induce the right alignment of the bacteria in order to do work to the rheometer.

6.1.2 Dense Magnetotactic Bacterial Suspensions in Confined Environments

When dense magnetotactic bacterial suspensions are enclosed in confined environments such as droplets, and exposed to external magnetic fields, they reveal macroscopic patterns such as vortices of the size of the droplet. It has been proposed that in very dense suspensions, the long-range hydrodynamic interactions are highly screened leading to very weak perturbations, so the system is governed by short-range interactions [48]. In this regard, we study through DSMC simulations the effect of the short-range interactions for a dense magnetotactic bacterial suspension with nematic and polar interactions confined in a spherical droplet, ignoring both magnetic and hydrodynamic long-range interactions. We employed wall-aligning BC and a repulsive potential among the bacteria in order to avoid unrealistic overlaps. The repulsion is considered via a Yukawa potential $U(\boldsymbol{r}_a) = \sum_b U(\boldsymbol{r}_{a,b})$, with

$$U(r_{a,b}) = U_0 \frac{\mathrm{e}^{-r_{a,b}/\lambda}}{r_{a,b}}, \tag{6.8}$$

where $\boldsymbol{r}_{a,b} = \boldsymbol{r}_a - \boldsymbol{r}_b$ is the distance vector between the swimmers a and b, U_0 is the strength of the repulsion, and λ is the screening-length which is typically the cell-size of the bacterium.

Simulations reveal that for very high concentrations, the short-range aligning interactions lead to the formation of vortices as shown in figs. 6.5 and 6.6 for polar and nematic interactions, respectively.

The next steps would be to compare measurable quantities with the experimental results, such as the vorticity or radial shear rates, in order to determine whether long-range hydrodynamic and magnetic interactions can be neglected or not.

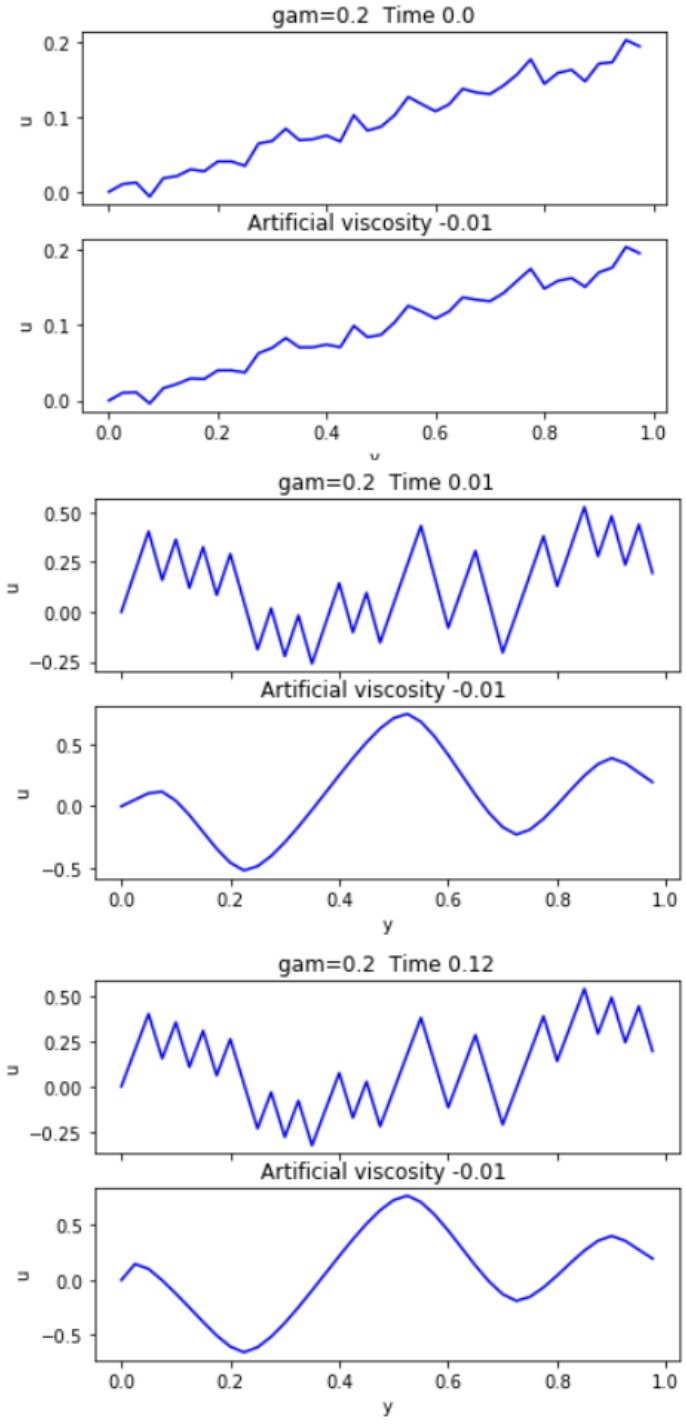

Figure 6.4: Velocity profiles at different times. Initial condition: Couette with noise. Dimensionless values.

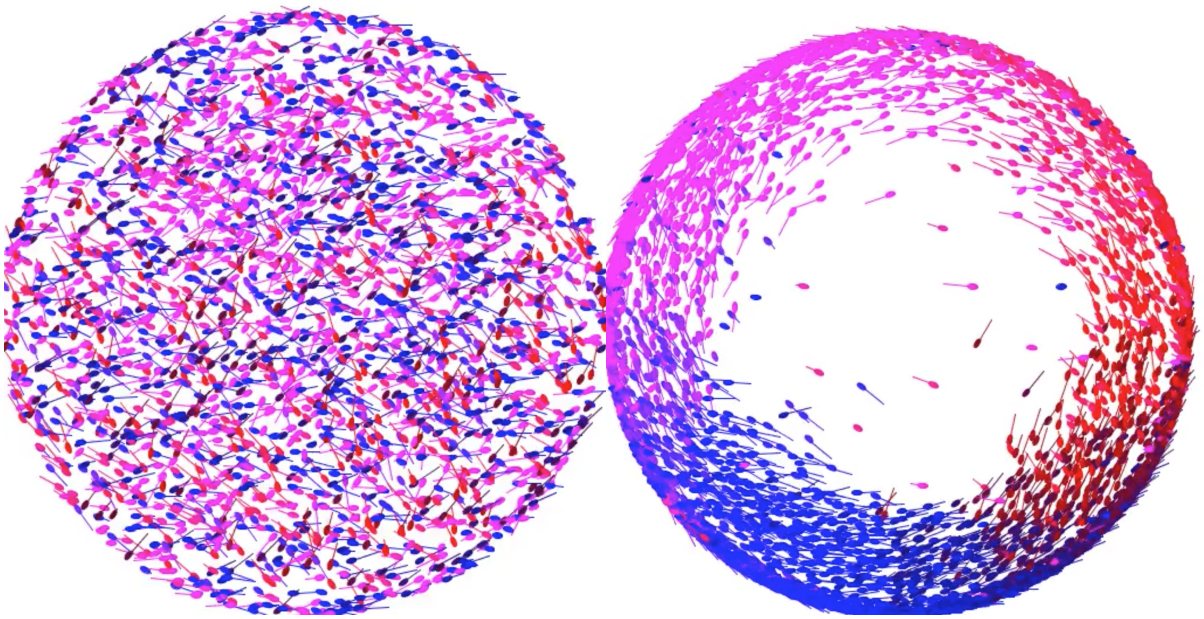

Figure 6.5: Snapshots of the simulations at $tD_\mathrm{r} = 0$ (left) and $tD_\mathrm{r} = 2$, showing a slice of the droplet (that is why the number of bacteria is not the same in both pictures). The magnetic field points in the upward direction. The droplet has a radius of 30 µm. The parameters used where $\lambda = 3\,\mu\mathrm{m}$, $\rho = 100$, $\beta = 0.7$, $\omega_\mathrm{m} = 1$, and polar interactions. The colors indicate the orientation of the swimmers.

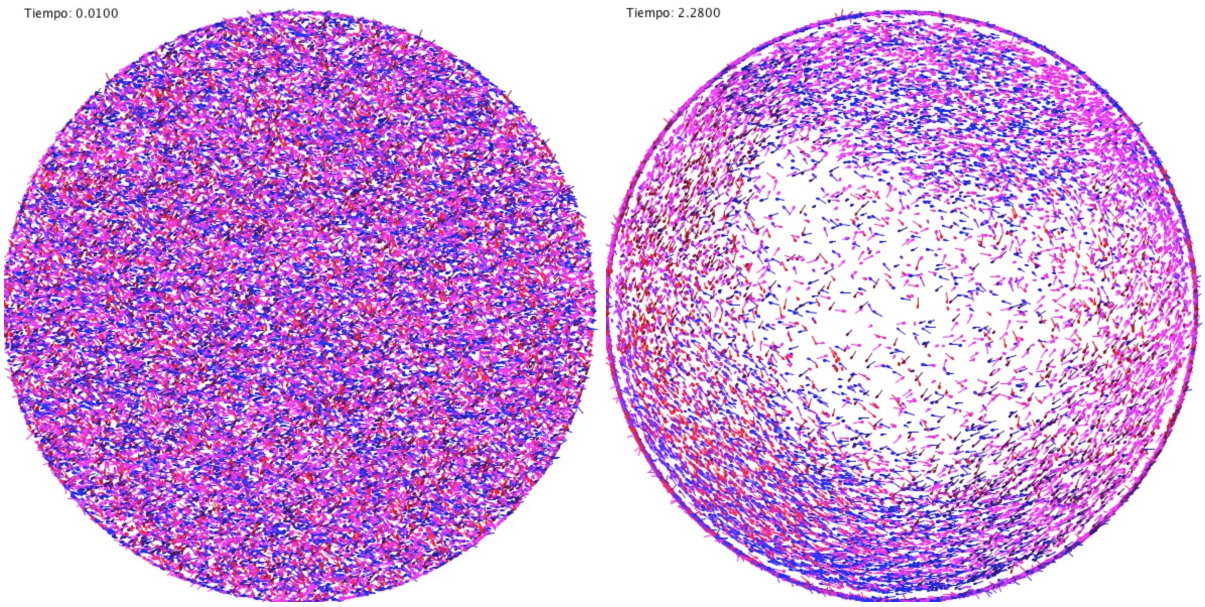

Figure 6.6: Snapshots of the simulations at $tD_\mathrm{r} = 0.01$ (left) and $tD_\mathrm{r} = 2.28$, showing a slice of the droplet. The magnetic field points in the upward direction. The magnetic field points in the upward direction. The droplet has a radius of 100 µm. The parameters used where $\lambda = 3\,\mu\mathrm{m}$, $\rho = 100$, $\beta = 0.7$, $\omega_\mathrm{m} = 1$, and nematic interactions. The colors indicate the orientation of the swimmers.

Chapter 7

Bibliography

[1] Igor S Aranson, Andrey Sokolov, John O Kessler, and Raymond E Goldstein. Model for dynamical coherence in thin films of self-propelled microorganisms. *Physical Review E*, 75(4):040901, 2007.

[2] Igor S Aranson and Lev S Tsimring. Pattern formation of microtubules and motors: Inelastic interaction of polar rods. *Physical Review E*, 71(5):050901, 2005.

[3] Igor S Aranson and Lev S Tsimring. Theory of self-assembly of microtubules and motors. *Physical Review E*, 74(3):031915, 2006.

[4] M Argentina, MG Clerc, and R Soto. Van der waals–like transition in fluidized granular matter. *Physical review letters*, 89(4):044301, 2002.

[5] Howard C Berg. *E. coli in Motion*. Springer Science & Business Media, 2008.

[6] Allison P Berke, Linda Turner, Howard C Berg, and Eric Lauga. Hydrodynamic attraction of swimming microorganisms by surfaces. *Physical Review Letters*, 101(3):038102, 2008.

[7] Richard Blakemore. Magnetotactic bacteria. *Science*, 190(4212):377–379, 1975.

[8] Francis P Bretherton. The motion of rigid particles in a shear flow at low reynolds number. *Journal of Fluid Mechanics*, 14(2):284–304, 1962.

[9] Navneet Dogra, Hadi Izadi, and T Kyle Vanderlick. Micro-motors: A motile bacteria based system for liposome cargo transport. *Scientific reports*, 6:29369, 2016.

[10] Christopher Dombrowski, Luis Cisneros, Sunita Chatkaew, Raymond E Goldstein, and John O Kessler. Self-concentration and large-scale coherence in bacterial dynamics. *Physical review letters*, 93(9):098103, 2004.

[11] Amin Doostmohammadi, Sumesh P Thampi, and Julia M Yeomans. Defect-mediated morphologies in growing cell colonies. *Physical review letters*, 117(4):048102, 2016.

[12] Knut Drescher, Jörn Dunkel, Luis H Cisneros, Sujoy Ganguly, and Raymond E Goldstein. Fluid dynamics and noise in bacterial cell–cell and cell–surface scattering. *Proceedings of the National Academy of Sciences*, 108(27):10940–10945, 2011.

[13] Jocelyn Dunstan, Gastón Mino, Eric Clement, and Rodrigo Soto. A two-sphere model for bacteria swimming near solid surfaces. *Physics of Fluids*, 24(1):011901, 2012.

[14] Jérémie Gachelin, Gastón Mino, Hélene Berthet, Anke Lindner, Annie Rousselet, and Éric Clément. Non-newtonian viscosity of escherichia coli suspensions. *Physical review letters*, 110(26):268103, 2013.

[15] George B Jeffery. The motion of ellipsoidal particles immersed in a viscous fluid. In *Proc. R. Soc. Lond. A*, volume 102, pages 161–179. The Royal Society, 1922.

[16] Tolga Kaya and Hur Koser. Characterization of hydrodynamic surface interactions of escherichia coli cell bodies in shear flow. *Physical review letters*, 103(13):138103, 2009.

[17] Tolga Kaya and Hur Koser. Direct upstream motility in escherichia coli. *Biophysical journal*, 102(7):1514–1523, 2012.

[18] R Kemkemer, D Kling, D Kaufmann, and H Gruler. Elastic properties of nematoid arrangements formed by amoeboid cells. *The European Physical Journal E*, 1(2-3):215–225, 2000.

[19] S Kim and S KARILLA. Microhydrodynamics [m], 1991.

[20] Arshad Kudrolli, Geoffroy Lumay, Dmitri Volfson, and Lev S Tsimring. Swarming and swirling in self-propelled polar granular rods. *Physical review letters*, 100(5):058001, 2008.

[21] Eric Lauga. Bacterial hydrodynamics. *Annual Review of Fluid Mechanics*, 48:105–130, 2016.

[22] AW Lees and SF Edwards. The computer study of transport processes under extreme conditions. *Journal of Physics C: Solid State Physics*, 5(15):1921, 1972.

[23] I Llopis and I Pagonabarraga. Hydrodynamic interactions in squirmer motion: Swimming with a neighbour and close to a wall. *Journal of Non-Newtonian Fluid Mechanics*, 165(17-18):946–952, 2010.

[24] Héctor Matías López, Jérémie Gachelin, Carine Douarche, Harold Auradou, and Eric Clément. Turning bacteria suspensions into superfluids. *Physical review letters*, 115(2):028301, 2015.

[25] M Cristina Marchetti, Jean-François Joanny, Sriram Ramaswamy, Tanniemola B Liverpool, Jacques Prost, Madan Rao, and R Aditi Simha. Hydrodynamics of soft active matter. *Reviews of Modern Physics*, 85(3):1143, 2013.

[26] Rohan Nadkarni, Solomon Barkley, and Cécile Fradin. A comparison of methods to

measure the magnetic moment of magnetotactic bacteria through analysis of their trajectories in external magnetic fields. *PloS one*, 8(12):e82064, 2013.

[27] Amir Alizadeh Pahlavan and David Saintillan. Instability regimes in flowing suspensions of swimming micro-organisms. *Physics of Fluids*, 23(1):011901, 2011.

[28] Julia K Parrish and William M Hamner. *Animal groups in three dimensions: how species aggregate*. Cambridge University Press, 1997.

[29] Walter F Paxton, Kevin C Kistler, Christine C Olmeda, Ayusman Sen, Sarah K St. Angelo, Yanyan Cao, Thomas E Mallouk, Paul E Lammert, and Vincent H Crespi. Catalytic nanomotors: autonomous movement of striped nanorods. *Journal of the American Chemical Society*, 126(41):13424–13431, 2004.

[30] Salima Rafaï, Levan Jibuti, and Philippe Peyla. Effective viscosity of microswimmer suspensions. *Physical Review Letters*, 104(9):098102, 2010.

[31] Mathias Reufer, Rut Besseling, Jana Schwarz-Linek, Vincent A Martinez, Alexander N Morozov, Jochen Arlt, Denis Trubitsyn, FB Ward, and Wilson CK Poon. Switching of swimming modes in magnetospirillium gryphiswaldense. *Biophysical journal*, 106(1):37–46, 2014.

[32] Michael Rubenstein, Alejandro Cornejo, and Radhika Nagpal. Programmable self-assembly in a thousand-robot swarm. *Science*, 345(6198):795–799, 2014.

[33] David Saintillan. The dilute rheology of swimming suspensions: A simple kinetic model. *Experimental Mechanics*, 50(9):1275–1281, 2010.

[34] David Saintillan. Extensional rheology of active suspensions. *Physical Review E*, 81(5):056307, 2010.

[35] David Saintillan and Michael J Shelley. Instabilities and pattern formation in active particle suspensions: kinetic theory and continuum simulations. *Physical Review Letters*, 100(17):178103, 2008.

[36] Andrey Sokolov, Mario M Apodaca, Bartosz A Grzybowski, and Igor S Aranson. Swimming bacteria power microscopic gears. *Proceedings of the National Academy of Sciences*, 107(3):969–974, 2010.

[37] Andrey Sokolov and Igor S Aranson. Reduction of viscosity in suspension of swimming bacteria. *Physical Review Letters*, 103(14):148101, 2009.

[38] Andrey Sokolov, Igor S Aranson, John O Kessler, and Raymond E Goldstein. Concentration dependence of the collective dynamics of swimming bacteria. *Physical review letters*, 98(15):158102, 2007.

[39] Rodrigo Soto. *Kinetic theory and transport phenomena*, volume 25. Oxford University Press, 2016.

[40] Thomas Surrey, François Nédélec, Stanislas Leibler, and Eric Karsenti. Physical properties determining self-organization of motors and microtubules. *Science*, 292(5519):1167–1171, 2001.

[41] John Toner and Yuhai Tu. Flocks, herds, and schools: A quantitative theory of flocking. *Physical review E*, 58(4):4828, 1998.

[42] Chih-kuan Tung, Florencia Ardon, Anubhab Roy, Donald L Koch, Susan S Suarez, and Mingming Wu. Emergence of upstream swimming via a hydrodynamic transition. *Physical review letters*, 114(10):108102, 2015.

[43] René Uebe and Dirk Schüler. Magnetosome biogenesis in magnetotactic bacteria. *Nature Reviews Microbiology*, 14(10):621, 2016.

[44] Tamás Vicsek, András Czirók, Eshel Ben-Jacob, Inon Cohen, and Ofer Shochet. Novel type of phase transition in a system of self-driven particles. *Physical review letters*, 75(6):1226, 1995.

[45] Benoit Vincenti, Carine Douarche, and Eric Clément. Actuated rheology of active magnetic suspensions: emergence of motor and brake states. *arXiv preprint arXiv:1710.01954*, 2017.

[46] Gaszton Vizsnyiczai, Giacomo Frangipane, Claudio Maggi, Filippo Saglimbeni, Silvio Bianchi, and Roberto Di Leonardo. Light controlled 3d micromotors powered by bacteria. *Nature communications*, 8:15974, 2017.

[47] Nicolas Waisbord, Christopher T Lefèvre, Lydéric Bocquet, Christophe Ybert, and Cécile Cottin-Bizonne. Destabilization of a flow focused suspension of magnetotactic bacteria. *Physical Review Fluids*, 1(5):053203, 2016.

[48] Henricus H Wensink, Jörn Dunkel, Sebastian Heidenreich, Knut Drescher, Raymond E Goldstein, Hartmut Löwen, and Julia M Yeomans. Meso-scale turbulence in living fluids. *Proceedings of the National Academy of Sciences*, 109(36):14308–14313, 2012.